



**Model studies on photocatalysis: Laser induced CO  
desorption from platinum nanoparticles at an alumina  
support**

in Partial Fulfillment of the Requirements for the Degree  
Doctor

in Natural Science

Presented to the Faculty of Mathematics and Science  
of Oldenburg University (Germany) by

**Alaa Al-Shemmary**

in September 2010

**The first Referee: Prof. Dr. Katharina Al-Shamery**

**The second Referee: Prof. Dr. Thorsten Klüner**

**Disputation day: 26.11.2010**

## Abstract

CO molecules adsorption has been studied at 90 K on different nanoparticles of platinum deposited via physical vapor deposition at 300 K on an epitaxial alumina support grown on NiAl(110). Fourier transform infrared reflection absorption spectra have been recorded as a function of CO coverage and the amount of platinum deposited. The CO adsorption is clearly assigned to on-top bonding when comparing the vibrational frequency to on-top CO on platinum single crystals. The CO vibrational frequency at saturation coverage increases linearly with the amount of the deposited platinum.

TPD experiments show two species, the high temperature species are assigned adsorption at step-edge sites and the low temperature species to adsorption at the perimeter interface between the platinum particles and the alumina.

Nanosecond laser excitation at  $\lambda = 355$  nm have been used to produce Laser induced desorption of CO adsorbed on platinum nanoparticles deposited on an epitaxial alumina support grown on NiAl(110). Laser desorption is observed, in contrast to the case for experiments on CO adsorbed on Pt(111) for the same laser wavelength. The influence of the laser fluence was studied systematically for a Pt deposition of 1Å. Fluences varied between 6.4 and 25.5 mJ cm<sup>-2</sup> per pulse. Fourier transform infrared reflection absorption spectra have been recorded as a function of CO coverage, the laser fluence and the number of photons impinging on the surface. For laser fluences below 12.7 mJ cm<sup>-2</sup> per pulse, a cross section of  $(1.1 \pm 0.2) \times 10^{-19}$  cm<sup>2</sup> can be estimated from the measurements. At elevated fluences a second desorption channel occurs with a cross section more than an order of magnitude larger, scaling linearly with the laser fluence. Laser induced particle morphology changes for CO covered surfaces are observed for higher laser fluences which are not apparent for bare particles. A model implying energy pooling within adsorbates at hot spots and even spillover between the metal nanoparticles and the oxidic support is discussed.

In a second set of experiments laser induced CO desorption was studied as a function of the amount of the deposited platinum on an epitaxial alumina support grown on NiAl(110). The amount deposited was varied between 0.5 to 3Å according to the quartz microbalance reading. The laser fluence was fixed to 6.4 mJ cm<sup>-2</sup> per pulse. Fourier transform infrared reflection absorption spectra were recorded as a function of CO coverage, the amount of the deposited platinum and the number

of photons impinging on the surface. For large amount of platinum thicknesses, a cross section of  $(1 \pm 5) \times 10^{-20} \text{ cm}^2$  can be estimated for the measurements increases as the amount of the deposited platinum decreases. At 0.5 Å amount of the deposited platinum, a second desorption channel occurs with a cross section larger by three orders of magnitude than for the largest amount of platinum deposited. In all cases desorption ends at a critical coverage beyond which no desorption occurs and which depends on the laser fluence. These results show that the smaller the particles are the more efficient the CO desorption is at certain laser fluences to occur. This is due to a shorter mean free path of electron path of the generated electrons in the particles.



## Kurzzusammenfassung

Es wurde die Adsorption von CO Molekülen bei 90 K auf verschiedenen Platinnanopartikeln untersucht, welche durch „physical vapor deposition“ (PVD) bei 300 K auf eptiaktischen Aluminiumoxidfilmen abgeschieden wurden. Die Filme wurden durch oberflächliche Oxidierung eines NiAl(110) Kristalls präpariert. Fouriertransformation-Infrarot-Absorptionsspektren in Reflexion wurden in Abhängigkeit der aufgetragenen Platinmenge aufgenommen. Die CO Adsorption kann durch Vergleich mit entsprechenden Messungen an Platineinkristallen, eindeutig einer „on-top“ Bindung zugeordnet werden. Die CO Schwingungsfrequenz einer Sättigungsbelegung nimmt linear mit der abgeschiedenen Platinmenge zu.

TDS Experimente zeigen zwei Spezies, die Hochtemperaturspezies kann der Adsorption an Stufenkantenplätzen und die Tieftemperaturspezies der Adsorption an der Kontaktzone zwischen Platinpartikel und umgebenen Aluminiumoxid zugeordnet werden.

Durch Anregung mittels eines Nanosekundenlasers bei einer Wellenlänge  $\lambda = 355$  nm wurde versucht eine laserinduzierte Desorption des auf den Platinpartikeln adsorbierten CO hervorzurufen. Im Gegensatz zu Experimenten mit der gleichen Wellenlänge an Platin (111) Einkristallen konnte eine CO Desorption beobachtet werden. Der Einfluss der Laserfluenz wurde für eine 1 Å Bedeckung an Pt systematisch untersucht. Die Fluenz wurde hierbei zwischen 6,4 und 25,5  $\text{mJ cm}^{-2}$  pro Puls variiert. Es wurden Fouriertransformation-Infrarot-Absorptionsspektren in Reflexion in Abhängigkeit von der CO Bedeckung, der Laserfluenz und der Zahl der auf die Oberfläche auftreffenden Photonen aufgenommen. Für Fluenzen niedriger als 12,7  $\text{mJ cm}^{-2}$  pro Puls kann der Wechselwirkungsquerschnitt mit  $(1,1 \pm 0,2) \times 10^{-19} \text{ cm}^2$  abgeschätzt werden. Bei erhöhten Fluenzen tritt ein zweiter Desorptionskanal mit einem um eine Größenordnung größerem Wechselwirkungsquerschnitt auf, welcher linear mit der Laserfluenz skaliert. Bei höheren Laserfluenzen wurde ebenfalls eine laserinduzierte Morphologieveränderung der CO bedeckten Partikel beobachtet, die bei unbedeckten Partikeln nicht auftritt. Ein Modell welches „energy pooling“ innerhalb der Adsorbate an „hot spots“ und „spillover“ zwischen den Metallnanopartikeln und der oxidischen Unterlage betrachtet wird diskutiert.

In einer zweiten Reihe von Experimenten wurde die laserinduzierte CO Desorption als Funktion des abgeschiedenen Platins betrachtet, wobei die Menge nach Messung mit einer Quarzmikrowaage

zwischen 0,3 und 5 Å variiert wurde. Die Fluenz wurde konstant auf  $6,4 \text{ mJ cm}^{-2}$  pro Puls gehalten und es wurden Fouriertransformation-Infrarot-Absorptionsspektren in Reflexion in Abhängigkeit von der CO Bedeckung, der Pt Bedeckung und der Zahl der auf die Oberfläche auftreffenden Photonen aufgenommen. Für große Platinschichtdicken kann der Wechselwirkungsquerschnitt mit  $(1 \pm 5) \times 10^{-20} \text{ cm}^2$  abgeschätzt werden. Dieser nimmt mit sinkender Platinbedeckung zu. Bei einer abgeschiedenen Menge von 0,5 Å tritt ein zweiter Desorptionskanal auf, welcher um 3 Größenordnungen größer ist als der bei der größten Bedeckung gemessene. In allen Fällen endet die Desorption bei einer Laserfluenz abhängigen kritischen Bedeckung über die Hinaus keine Desorption statt findet. Die Ergebnisse zeigen dass für bestimmte Fluenzen die Effizienz der CO Desorption mit sinkender Partikelgröße zunimmt. Dies beruht auf der kleineren freien Weglänge der innerhalb des Partikels angeregten Elektronen.

*To my parents*

## Acknowledgments

I would like to express the deepest appreciation to my supervisor Prof. Dr. Katharina Al-Shamery for the continuous support of my Ph.D study and research, for her patience, motivation, enthusiasm, and immense knowledge. Her guidance helped me in all the time of research and writing of this thesis. I gratefully acknowledge Prof. Dr. Klüner for the support, recommendation and scientific evaluation. My acknowledge to Prof. Wittstock's work group regards help with the Atomic force microscope.

I am very grateful to my friends Robert Buchwald and Dirk Hoogestraat. Thanks for your scientific discussion and your valuable support in this work. Thanks for your sense of humor and your close friendships. My acknowledgment to all the group members for the nice time we have spent together.

Special thanks to Mr. Al-Shamery for his great effort starting from the first day that I have been in Germany until the last letter of this thesis. Mr. Al-Shamery, I am very grateful to you.

My thanks go to Mrs. Szefczyk and Mrs. Schroeter-Schuller for their support to get the publications.

I would like to thank my friends Frank, Anja, Tobias and Ralf for your patient and the delicious food. I have spent a good time with you.

There is no word to express my thanks to my parents for their love, support and your emotions. My brothers Dhiaa and Bahaa thanks for your encouragement and your love. Thanks for my family, my uncles and cousins for your support.

## List of abbreviations

<b>UV</b>	Ultra Violet
<b>REMPI</b>	Resonance Enhanced Multi-Photon Ionization
<b>MGR</b>	Menzel-Gomer-Redhead
<b>DIET</b>	Desorption Induced by Electronic Transitions
<b>PES</b>	Potential Energy Surface
<b>TDS</b>	Thermal Desorption Spectroscopy
<b>TPD</b>	Temperature Programmed Desorption
<b>UHV</b>	Ultra High Vacuum
<b>LEED</b>	Low Energy Electron Diffraction
<b>IR</b>	Infrared
<b>FT-IR</b>	Fourier Transform Infrared
<b>ZPD</b>	Zero Path Difference
<b>STM</b>	Scanning Tunneling Microscopy
<b>FTIRAS</b>	Fourier Transform Infrared Absorption Spectroscopy
<b>MCT</b>	Micro Channel Tube
<b>PID</b>	Proportional Integral Derivative
<b>Nd:YAG</b>	Neodymium-doped Yttrium Aluminium Garnet; Nd:Y <sub>3</sub> Al <sub>5</sub> O <sub>12</sub>
<b>ISS</b>	Ion Scattering Spectroscopy
<b>EELS</b>	Electron Energy Loss Spectroscopy
<b>TEM</b>	Transmission Electron Microscopy
<b>AES</b>	Auger Electron Spectroscopy
<b>AFM</b>	Atomic Force Microscopy

# Table of Contents

<b>1 Introduction</b> .....	1
<b>2 Theory</b> .....	4
2.1 Laser induced processes at surfaces.....	4
2.2 The Menzel-Gomer-Redhead model (MGR).....	4
2.3 Thermal Desorption Spectroscopy.....	7
2.4 LEED.....	11
2.5 Infrared spectroscopy.....	14
2.5.1 Normal modes of vibration.....	15
2.5.2 FTIR spectrometer.....	16
<b>3 Experimental setup</b> .....	20
3.1 Introduction.....	20
3.2 The UHV chamber and the spectroscopic methods.....	20
3.2.1 Sample holder.....	23
3.3 IR experiment.....	24
3.4 TDS.....	26
3.5 Scanning methods.....	26
3.6 Nanosecond Laser.....	27
3.7 Sample preparation.....	27
3.7.1 Pt/Al <sub>2</sub> O <sub>3</sub> /NiAl(110).....	27
3.7.2 Pt(111).....	28
<b>4 Structure and properties of the model catalyst Pt/Al<sub>2</sub>O<sub>3</sub>/NiAl (110)</b> .....	30
4.1 Introduction .....	30
4.2 Electronic and geometric structure.....	31

4.3 Nucleation and growth at different temperatures.....	33
4.4 Growth and Morphology.....	37
4.5 Structural characterization of Pt/Al <sub>2</sub> O <sub>3</sub> /NiAl(110).....	42
4.5.1 AFM scans of Platinum deposited over Al <sub>2</sub> O <sub>3</sub> at 300K.....	42
4.5.2 Scans of Platinum deposited on Al <sub>2</sub> O <sub>3</sub> /NiAl(110) at 100K.....	45
4.6 STM scan for 1Å Pt deposited at 300K/Al <sub>2</sub> O <sub>3</sub> .....	48
4.7 Discussion.....	49
<b>5 Adsorption and desorption of CO from Platinum surfaces.....</b>	<b>51</b>
5.1 Adsorption and desorption of CO from Platinum single crystals.....	51
5.1.1 Pt(111).....	52
5.1.2 Pt(533).....	56
5.1.3 Pt(321).....	60
5.2 Pt(335) & Pt(112).....	64
5.2.1 TPD measurements.....	64
5.2.2 FTIR measurement.....	67
5.3 Adsorption of CO on Pt Nanoparticles.....	70
5.4 CO desorption from Platinum nanoparticles.....	80
5.5 Discussion.....	87
<b>6 Laser induced processes of CO at Pt surfaces using nanosecond laser.....</b>	<b>88</b>
6.1 Laser induced CO desorption from Pt(111) single crystal.....	89
6.2 The effect of Laser induced CO desorption from Pt deposited at 300K.....	93
6.3 Adsorbate-induced roughening of Platinum nanoparticles after laser irradiation.....	101
6.4 Laser induced CO desorption from different Pt thickness deposited at 300K.....	103
6.5 Calculation of the error propagation in the desorption cross section.....	109
6.6 Discussion.....	111
<b>References.....</b>	<b>112</b>
<b>List of figures.....</b>	<b>124</b>

## 1 Introduction

The demand for energy is increasing permanently due to the fast expansion in the emerging economies and growing of the population while the cheap natural resources are limited. This fact will lead to a major problem in the next century but there are several solutions for this problem. One of the solutions is to develop renewable energies. The sun is the largest source of energy at hand. To produce solar fuels, photochemical reactions at solid surfaces are used. The ability to photochemically split water into hydrogen and oxygen for fuel cells by semiconductor and oxide surfaces are used in photocatalysts. The semiconductor surfaces have been investigated for several decades (Kamat 2007). The molecule surface interaction is often accompanied by charge transfer that changes the electronic properties of the molecule in the ground and the excited state. New reaction paths with regards to the free molecule may become available and would be useful for a lot of technological applications. The main problem to use the photochemical reactions to produce solar fuels is their efficiency. It has been discussed that photochemical cross sections could be enhanced by using nanoparticles to modify the surface (Pan *et al.*, 2007).

Focus most recently started to be on gaining insight into elementary processes at samples like a catalyst system consisting of nanoparticle/support systems. A lot of factors have been studied like particle structure, the influence of edges and kinks, the metal particle size, the particle perimeter as well as the particle/support interaction and spill over processes. Also the microkinetics might be influenced by distances between particles. Depending on the temperature and pressure, all these properties might change even in a dynamical way under reactive conditions.

In photochemical reactions several processes might happen. Direct electronic excitation of the adsorbate itself can occur, followed by its decomposition. Such a process is dominant in large aromatic molecules, carbonyls and other metal organic molecules. This process is taken advantage of in some applications like photolithography (Okoroanyanwu 2002). The indirect excitation is dominant in smaller molecules including substrate excitation that lead to hot electron transfer to the adsorbate. This excitation is related to the fact that first optically allowed transitions of these molecules could normally be found in the UV or VUV regimes for gas phase molecules.



In nanocomposite systems the population of different possible photochemical reaction channels depends on the metal nanoparticle size as has been shown in an early work by Watanabe *et al.* (1999). They have reported that the branching ratio between UV laser induced photodissociation and photodesorption changes dramatically with the metal particle size for nanoparticles in the lower nanometer regime when looking at the photodissociation of methane adsorbed at nanoparticulate palladium on an epitaxial alumina support. While methane tends to dissociate after laser excitation when adsorbed at larger particles, photo desorption is most efficient for smaller nano particles at particle diameters below 4.5 nm. When the particle sizes are in the size regime of the mean free path of the excited electron or below photodesorption becomes particularly efficient.

Kamplung *et al.* (2002) used quantum state resolved spectroscopy to map the energy partitioning of NO desorbing from palladium nanoparticles on an epitaxial alumina support. They found that though the photo desorption cross sections easily changes by at least one order of magnitude the final energy distribution was little sensitive to the particle size. From these findings they concluded that apparently defect sites may play a major role to pin the initial excitation energy for inducing the photochemical desorption.

Wille *et al.* (2003) investigated local site changes of CO adsorbed at palladium nanoparticles on an epitaxial alumina support. When using ultra short pulses of laser light they found metal nano particle deterioration for CO coverages of fluctuating adsorbate densities (Wille *et al.* 2004). From extensive experiments with various isotopic C<sup>12</sup>O/C<sup>13</sup>O mixtures they concluded that at particle edges energy pooling arises along rows of densely packed adsorbates which may be followed by energy pinning at kinks and concomitant formation of local hot spots responsible for the metal nano particle destruction. The adsorbate coverage was crucial for particle decomposition to occur. For the system investigated desorption was only a minor reaction channel for extremely small particles consisting of only a few atoms.

In view of these results investigations in this thesis will be reported on a closely related adsorbate system: CO adsorbed at nanoparticulate platinum on an epitaxial alumina support. In contrast to palladium CO adsorbs on Pt(111) preferentially at on top sites while at Pd(111) it initially adsorbs at threefold coordinated sites at low coverages (Hayden & Bradshaw 1983).

Laser induced desorption of CO from Pt(001) and Pt(111) has been investigated by Peremans *et al.* (1993a,b) and Fukutani *et al.* (1995) involving a state resolved mapping of the desorbing molecules using (2+1) REMPI (Resonance Enhanced Multi-Photon Ionization). The fluence dependence of the desorption with a laser wavelength of 193 nm indicated that CO desorption occurs as a three photon process from Pt(001). This may be connected to a direct excitation of CO itself. On the other hand a single photon process is relevant for CO desorption from Pt(111) indicating an initial surface excitation step. Electron stimulated desorption experiments from Pt(111) by Burns *et al.* (1987) resulted in neutral, electronically excited CO. No laser experiments have been reported for nano particulate platinum under well defined conditions to my knowledge.

## 2 Theory

### 2.1 Laser induced processes at surfaces

A chemical bonding which is the molecule-surface bond is created when the molecules adsorb on a surface. Due to the molecule surface interaction the electronic and the vibrational states will be changed in the adsorbed molecules. The surface chemistry of low photons and electron reaction is related to changes in the electronic states of the adsorbed molecules. A path for surface reactions has been created through the molecule surface binding which may be activated by thermal, electronic or photo excitation. Catalyst systems consisting of small particles on an inert oxide are considered efficient catalysts. Therefore investigation of the influence of the particle size and morphology with regard to the catalytic activity is very important.

In the beginning of surface photochemistry research, work has been focused on single crystals in conjunction with ultra high vacuum and corresponding laser systems for a defined excitation and analysis (Chuang 1986, Ho 1988, Dai *et al.* 1995, Cavannagh *et al.* 1993, Ho 1990, Hasselbrink 1991). Useful applications such as catalysis material processing, photolithography and gain of solar fuels have increased the interest to investigate this branch of science.

The absorption of photons by the adsorbates or the substrate determines the photochemical surface reaction. Various energy transfer processes including deexcitation mechanisms lead to reaction or desorption/diffusion. This may be known as a composite process involving photon absorption connected with a transition to an excited electrical state, followed by a nuclear motion on a repulsive potential curve.

### 2.2 The Menzel-Gomer-Redhead model (MGR)

The Menzel-Gomer-Redhead (MGR) model has explained photodesorption (Menzel & Gomer 1964, Redhead 1964). Figure 2.1 shows a schematic diagram of the MGR model for desorption induced by electronic transitions (DIET).

The elements of the MGR model are a ground state, a Frank-Condon type electronic transition and an excited state Potential Energy Surface (PES). An adsorption state on the surface is influenced by several conditions like adsorption sites, adsorption structures, coverage, etc. This adsorption state determines the ground state PES. The adsorbate will be transferred via a Frank-Condon type electronic transition from the ground state to the excited state which is repulsive in the MGR model by the absorbed photon. The motion of the molecule on the excited PES depends on the excitation processes because the excited state PES depends on the nature of the excited state, e.g., the excitation level of intermolecule or adsorbate-substrate, electron or hole attachment. The adsorbate is accelerated and gains kinetic energy  $E_k$  during its residence time on the excited state PES. The adsorbate will gain potential energy after the quenching of the excited state to the ground state because the position of the adsorbate with respect to the surface is different from the situation before excitation due to the motion of nuclei on the excited state PES ( Zimmermann & Ho 1995).

The adsorbate will be desorbed with a kinetic energy  $E_k$ , if the summation of the gained potential and kinetic energies in the reaction coordinate is sufficient to overcome the desorption barrier  $E_b$ . So different translational temperatures ( $Tt = \langle Ek \rangle / 2kB$ ) and photodesorption cross sections reflect different adsorption states and excitation processes. The MGR can be used for photoinduced dynamics by choosing the appropriate reaction coordinate although it was initially developed to describe desorption of adsorbates.

The Antoniewicz model has contributed an ionic excited state of the adsorbate as a similar way of photodesorption (Antoniewicz 1980). Figure 2.2 describes the Antoniewicz model and shows the transient negative (positive) ion state on the excited PES by electron (hole) transfer from the metal substrate to the adsorbate. The adsorbate is accelerated to the surface and gains kinetic energy  $E_k$  in the transient negative (positive) ion state of adsorbate. The electron (hole) attached to the adsorbate jumps back into the metal substrate after a residence time on the excited state PES. Due to a different adsorbate-surface distance, the adsorbate experiences a repulsive force. Like for the MGR model, desorption occurs with kinetic energy  $E_k$ , if the sum of the gained potential and kinetic energies in the reaction coordinate are sufficient to overcome the desorption barrier  $E_b$ .

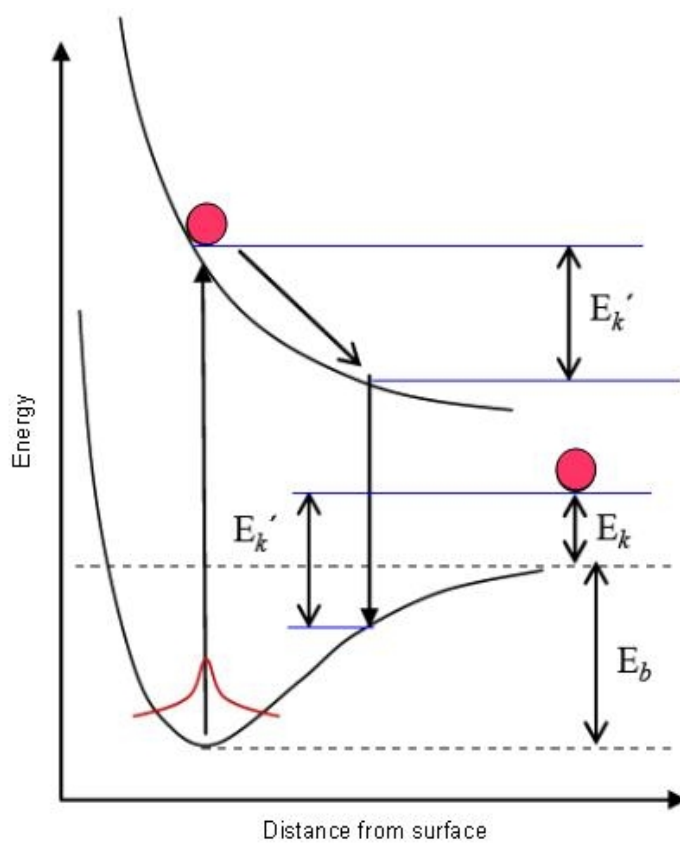


Figure 2.1: Schematic drawing of the MGR model. The excited state PES is repulsive (Rubahn 1999).

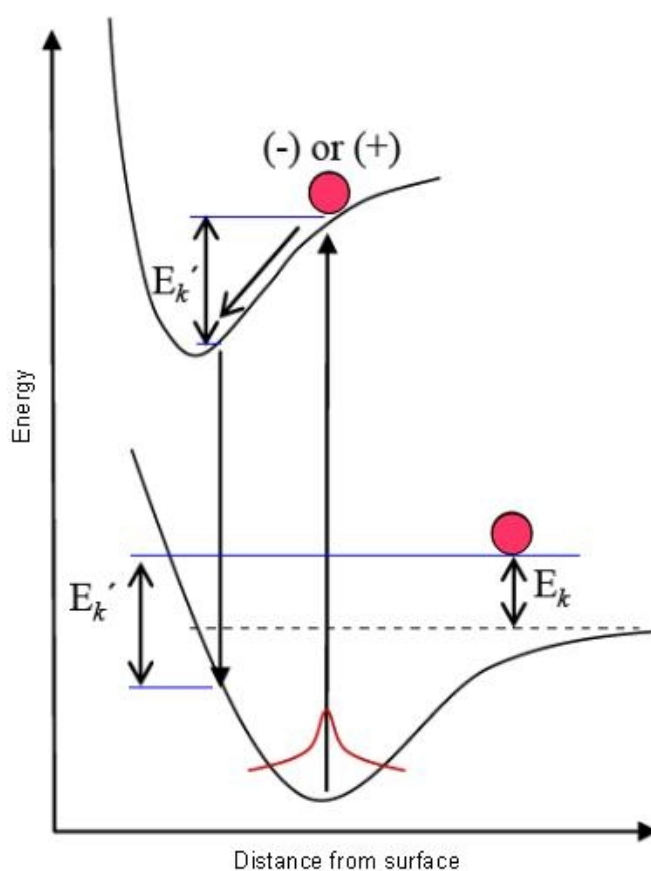


Figure 2.2: Schematic drawing of the Antoniewicz model. The excited state PES is attractive due to an image charge on the metal substrate (Rubahn 1999).

### 2.3 Thermal Desorption Spectroscopy

Thermal desorption spectroscopy (TDS) is a useful method in surface science because it offers good possibilities to interpret desorption in terms of reaction kinetic theories like the transition state formalism. It is also called temperature programmed desorption (TPD) and it is particularly used to study the desorption of gases from single crystals and polycrystalline samples into vacuum. (Falconer & Schwarz 1983).

A schematic set up for thermal desorption is shown in Figure 2.3. The crystal is mounted in the crystal holder described in chapter 3. This crystal holder is attached to a cooling reservoir in the UHV chamber. The crystal is heated by a tungsten filament. By using a thermocouple spot welded at the side of the crystal the temperature is monitored. The interesting part from monitoring the temperature is the heating rate which is typically between 0.1 and 25 K per second.

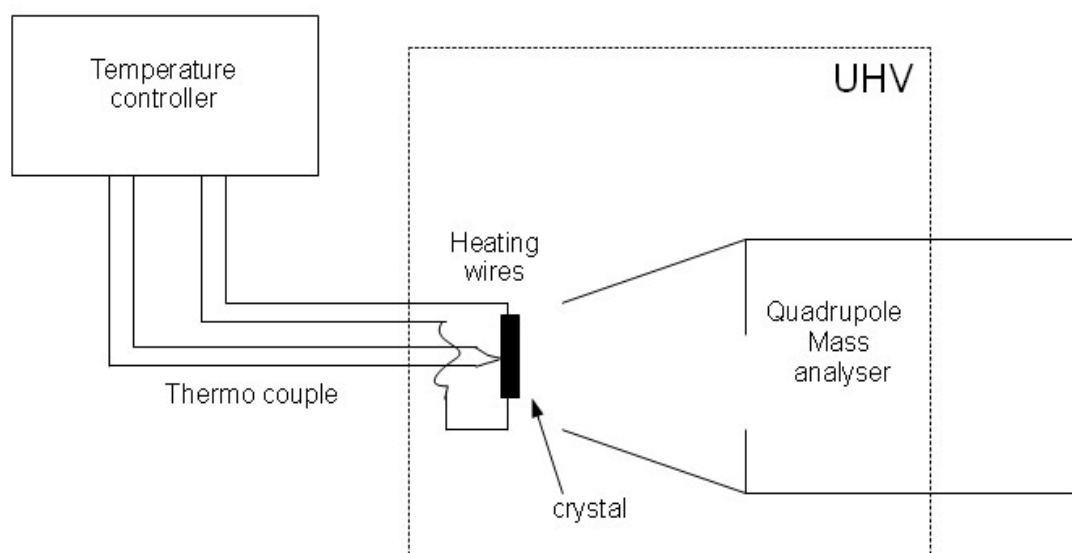


Figure 2.3: Schematic drawing for TPD experimental setup (Niemantsverdriet 1993)

The quadrupole mass spectrometer is used for measuring the intensities of the desorbed species. It could also be measured by another method like monitoring the work function of the sample or determined with an ionization manometer. Feulner and Menzel have described optimized geometries for TDS measurements (Feulner *et al.* 1980).

An important consideration in the thermal desorption is the pumping capacity or pumping speed because the spectra could suffer broadening at higher desorption temperatures. The pumping speed

should be high enough to prevent the desorbed species to readsorb back onto the surface. Desorption experiments in UHV systems pumped by turbo pumps with an insufficient pump speed for light gases such as H<sub>2</sub> will suffer from readsorption features. The situation becomes less critical for heavier gases.

The readsorption could be neglected, if the pumping speed is high enough. The relative rate of desorption, defined as the change in adsorbate coverage per unit of time is given by (King 1975) :

$$r = -\left(\frac{d\theta}{dt}\right) = k_{des} \theta^n = \nu(\theta) \theta^n \exp\left(-E_{des} \frac{(\theta)}{RT}\right) \quad (2.1)$$

$$T = T_o + \beta t \quad (2.2)$$

in which

- $r$  is the rate of the desorption
- $\theta$  is the coverage in monolayers
- $t$  is the time
- $k_{des}$  is the reaction rate constant for desorption
- $n$  is the order of desorption
- $\nu$  is the preexponential factor of desorption
- $E_{des}$  is the activation energy of desorption
- $R$  is the gas constant
- $T$  is the temperature
- $T_o$  is the temperature at which the experiment starts
- $\beta$  is the heating rate, equal to  $dT/dt$ .

The desorption parameters  $E_{des}$  and  $\nu$  dependent on the coverage because of attractive or repulsive interaction between the adsorbate molecules (Cassuto & King 1981).

The Redhead method is the most known among surface scientists in which the activation energy of the desorption is given by:



$$E_{des} = RT_{max} \left[ \ln \left( \nu \frac{T_{max}}{\beta} \right) - 3.46 \right] \quad (2.3)$$

where

$E_{des}$  is the activation energy of desorption

$R$  is the gas constant

$T_{max}$  is the peak maximum temperature

$\nu$  is the preexponential factor

$\beta$  is the heating rate  $dT/dt$ .

For  $\nu/\beta$  values between  $10^8$  and  $10^{13} \text{ K}^{-1}$  the expression (2.3) is approximately correct for first order desorption. From a single TDS spectrum one may determine  $E_{des}$  but in case of a normal desorption kinetics one may choose a value of  $\nu = 10^{13} \text{ s}^{-1}$ , independent of the coverage. This choice is only valid for a so called tight transition state. The Redhead formula should only be used if a reliable value for the prefactor is available.

Another popular method to extract  $E_{des}$  and  $\nu$  uses the peak maximum temperature  $T_{max}$  and the peak width, either at half or at three quarters of the maximum intensity. Their expressions for first order desorption is then:

$$E_{des} = RT_{max} \left[ -1 + \sqrt{1 + 5.832 \left( \frac{T_{max}}{W} \right)^2} \right] \quad \text{for } n=1 \quad (2.4)$$

$$\nu = E_{des} \frac{\beta}{RT_{max}^2} e^{\frac{E_{des}}{RT_{max}}} \quad [T] = \text{K} \quad (2.5)$$

in which  $W$  is the peak width at half of maximum intensity; the other parameters are defined in eq. (2.3). Similar expressions exist for the peak width at three quarters of the maximum intensity and for second order desorption. Essential is that  $E_{\text{des}}(\theta)$  and  $v(\theta)$  values obtained this way are extrapolated to zero coverage, to obtain the desorption parameters of a single molecule adsorbed on an otherwise empty surface (Chan *et al.* 1978).

## 2.4 LEED

The low energy electron diffraction (LEED) is one of the most common surface analysis methods (Davisson & Germer 1927). It has to be noted that the structural information contains no information about the chemical composition .

From the de Broglie relationship, the wavelength of electrons is related to their kinetic energy  $\lambda = (150 \text{ eV} \text{ \AA}^2 / E)^{1/2}$ . Electrons below 500 eV have the correct wavelength to interfere with atomic structure that are  $\text{\AA}$  in size shown by the above relationship. The LEED only provides structural information about the atoms in the surface region because the low energy electrons ( $< 500 \text{ eV}$ ) penetration depth is only a few  $\text{\AA}$

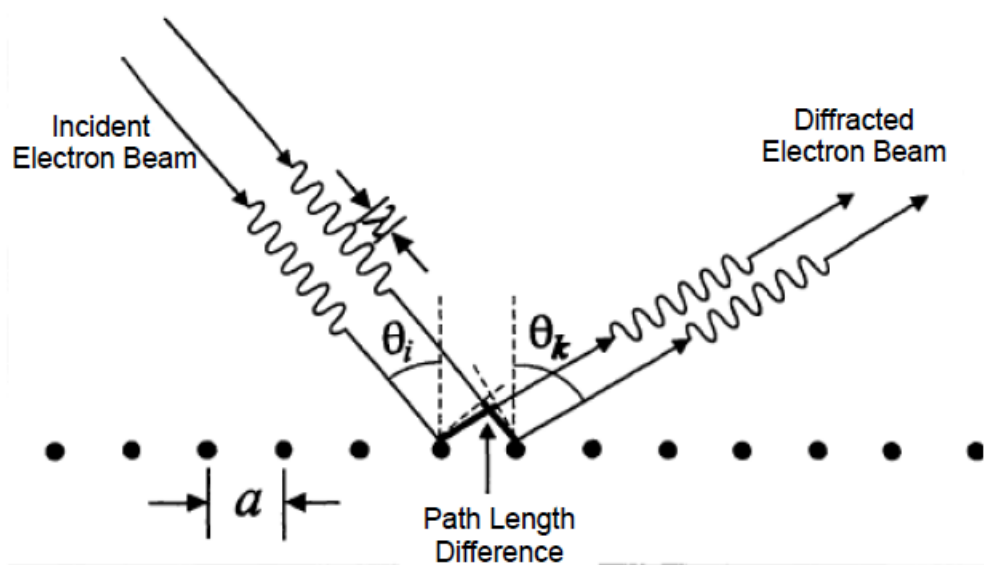


Figure 2.4: Diffraction from a one-dimensional lattice (Smith 1995)

We consider a one dimensional array of atoms to explain the diffraction of electrons as shown in Figure 2.4. The wavelength ( $\lambda$ ) of the incident electrons is comparable to the inter atomic spacing ( $a$ ). The only electrons that are detected in the LEED experiment are elastically scattered and have the same kinetic energy as the incident electrons. These electrons scatter in all directions but when the difference in the path length of the scattered electrons is an integer multiple of the incident wavelength, constructive interference can occur. This formula gives the angles at which these diffraction patterns will occur:

$$k \lambda = a (\sin \theta_k - \sin \theta_i) \quad (2.6)$$

$k$ : 0, +-1, +-2, +-3,...

$\theta_i$ : incident angle

$\theta_k$ : scattering angle

$a$ : interatomic spacing

$\lambda$ : wavelength of the incident electrons

A two dimensional lattice can be treated alike to produce diffraction patterns. The angle of incidence ( $\theta$ ) on the screen is normally zero so the diffraction equation will be  $k \lambda = a \sin \theta_k$ ,  $d$  is the distance from the sample to the hemispherical phosphorescent screen. Visible spots will appear on the screen when the diffracted electrons incident on the screen and the distance between the spots is  $d \sin \theta$  and it is equivalent to  $d \lambda / a$ . Because of the proportionality between the diffraction spots to  $1/a$  with units of  $\text{\AA}^{-1}$  it is convenient to introduce the concept of reciprocal space. Every real space lattice has a corresponding reciprocal lattice, if the unit cell vector  $a$  and  $b$  of the real space, the reciprocal lattice, will be defined as  $a^*$  and  $b^*$  such that:

$$a \cdot a^* = b \cdot b^* = 1 \quad (2.7)$$

$$a \cdot b^* = b \cdot a^* = 0 \quad (2.8)$$

A convenient way of calculating the real space unit cell vectors  $a$  and  $b$  is done by measuring the reciprocal space unit cell vectors  $a^*$  and  $b^*$  with knowing the distance between the sample and the screen  $d$ .

The LEED gives an indication for the long order of the surface structure and also determines the size and the symmetry of the real space unit cell. If the surface structure over a distance is regular, it should be larger than the coherence width of the incident electron beam. A diffuse spot will appear instead of sharp diffraction spots, if this condition is not applied. Therefore analyzing the sharpness of the diffraction spots gives information about the surface regularity. An indication of a lower degree of regularity on the surface is apparent, if the pattern on the screen has a diffuse background between the diffracted beams because of a significant amount of non coherency.

The LEED pattern is used as a fingerprint for identification once the diffraction pattern of a particular surface is known. Also it could be used to estimate the cleanliness of the surface and for following the phase transformations between structures that have different diffraction patterns.

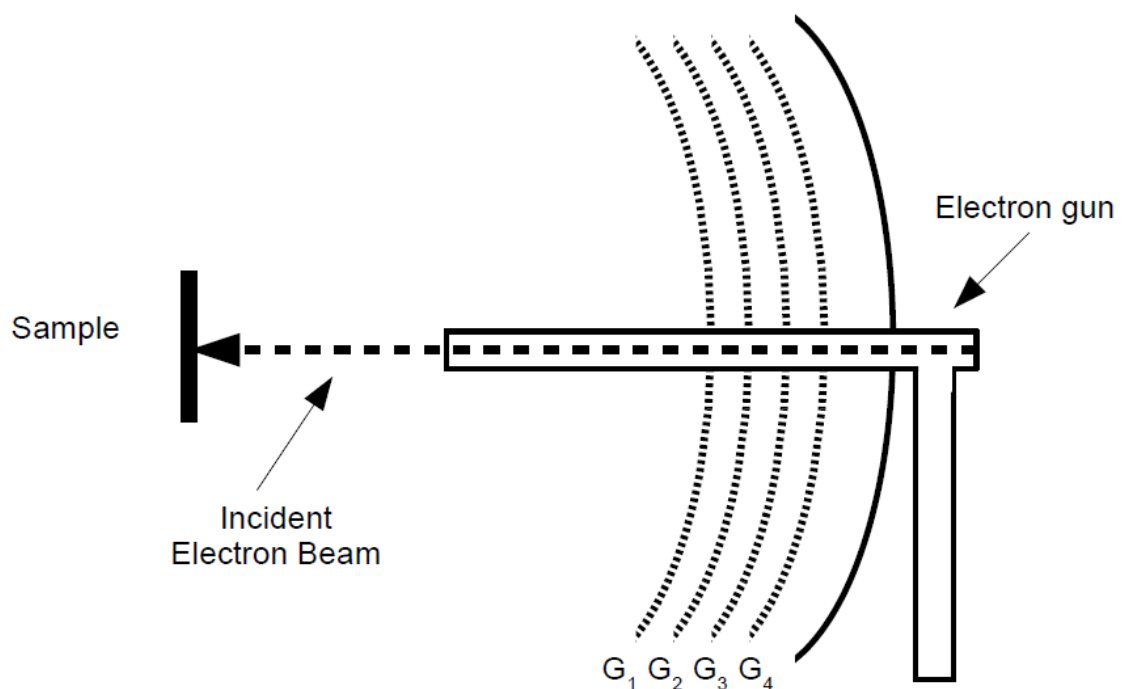


Figure 2.5: Schematic drawing of the LEED (Niemantsverdriet 1993)

Figure 2.5 shows a schematic drawing of LEED electron optics. It consists of 4 grids, an electron gun and a fluorescence screen. The electrons are delivered to the sample using the lens system to collimate the accelerated electrons from iridium filament with the electron beam incident perpendicular to the surface. The first grid is connected to the ground potential as the sample. The second and third grid allow only the scattered electrons to pass to the screen so they work as a high pass filter. Again the fourth grid is connected to the ground potential which protects the separated electrons from the influence of electric field. A two dimensional lattice pattern of elastically scattered electrons is generated by the scattered electrons at the surface of individual atoms.

## **2.5 Infrared spectroscopy**

One of the powerful methods in surface science is IR spectroscopy to study the adsorption of the molecules on well defined metal surfaces. A sensitivity of up to 1/1000 of a CO monolayer has been achieved at high resolution ( $1\text{-}5\text{ cm}^{-1}$ ).

It is well known that the electromagnetic radiation can interact with electrons being a moving charge and that energy can be released to it based on Bohr's atomic model. The same idea is applied to the vibrating or rotating atomic group which could be associated with the motion of an electric charge, especially when the distribution becomes asymmetric by the vibration of the atoms or when the charges of the atoms in a molecule are asymmetrically distributed.

Then, when an electromagnetic excitation results in a change in the dipole moment of a molecule, the electromagnetic radiation of the corresponding frequency can be absorbed and is associated with vibrational excitation of the atomic group. In principle, the diatomic molecules with the same atoms can not be excited to vibrate because they do not have any transition dipole moment. Vibrations are then characterized as infrared inactive when the change of the dipole moment is not present. However, the infrared radiation can always interact with molecules consisting of various types of atoms and with those having a transition dipole moment because of an antisymmetric displacement of the center of charge.

## 2.5.1 Normal modes of vibration

A single vibrational motion can be performed in a diatomic molecule by nature. In a simple way the number of possible vibrational modes of multi atomic molecules can be calculated. Each single atom can move in three spatial directions corresponding to  $3N$  spatial coordinates for  $N$ , the number of atoms. Therefore,  $3N$  degrees of freedom are available for a system of  $N$  points of mass.

A simultaneous change in the position of the center of mass of all atoms results in the translational motions of the molecule in three possible dimensions. They are subject to the laws of kinetic gas theory and do not belong to the field of molecular spectroscopy since an interaction with electromagnetic radiation does not happen. Very intensive absorption bands are produced by so called lattice vibrations which are excitable in the far IR spectral region associated only to the periodically repeating molecular translations in the crystalline structure of a solid. In the gas phase a rotation around the center of the mass is caused by further three movement combinations, so that the number of actual vibrational degrees of freedom is in this case in contrast to the  $3N$  vibrational modes of a solid:

$$Z=3N-6$$

Since the rotation around the molecular axis is not connected with any displacement of the atoms or of the center of the mass, the linear molecules have only two rotational degrees of freedom. Therefore, this molecule type has one more vibrational degree of freedom.

$$Z=3N-5$$

The molecule's normal modes of vibration are the calculated number of molecule vibrations which could be excited independently from one another. The atoms oscillate with the same frequency and the same phase when they are involved in the normal modes of vibration. A particular vibrational frequency is assigned to each normal vibration, whereby the frequencies of different vibrations can nevertheless adopt the same value under certain prerequisite conditions.

Blyholder has attempted to explain the origin of the CO stretching mode vibrational shift in terms of the mechanism of CO bonding to metal surfaces. The bonding happens when the charge transfer from the  $5\sigma$  orbital of CO to the unoccupied metal orbitals occurs followed by a charge transfer, or back donation, from the  $d_{\pi}$  metal orbitals to the  $2\pi^*$  unoccupied level of CO. Because of a large transition dipole moment in the adsorbed CO molecule, a dipole-dipole interaction occurs when CO molecules adsorb on a surface specially when distances are very small. The static repulsion that is produced from the dipole- dipole coupling will produce a frequency shift. This phenomena is very clear at high adsorption coverages.

### 2.5.2 FTIR spectrometer

Spectrometers are generally classified into two types. The dispersive spectrometers are the first type which consists of a radiation source, a dispersive element such as a grating and a detector. The spectrum is recorded by measuring the IR signal directly via the detector as a function of wavelength. The dispersive spectrometers have disadvantages like long scanning time and low IR intensity because of the dispersive elements which contribute to the signal to noise ratio. The Fourier-transform infrared (FTIR) spectrometer is the second type of spectrometers. This type of spectrometers consists generally of a radiation source, a Michelson interferometer and a detector. The spectrum is not recorded directly from the detector like for the first type spectrometer, but the interference intensity of two beams is recorded as a function of optical path difference with a following FT of the data. The heart of the FTIR spectrometer is the classical Michelson interferometer which is shown in Figure 2.6 as schematic diagram.

The beam of radiation from the source is split by a semi-permeable beam splitter into two partial beams that are reflected on a fixed and on a movable mirror back to the beam splitter where they recombine and are brought to interfere. The fraction directed back to the source is not used and gets lost. A shifting of the movable mirror changes the optical path length in this interferometer arm, whereby a phase difference between both partial beams results in a change in the interference amplitude. The interferogram is the intensity signal  $I(x)$  at the detector recorded as a function of the change in the optical path difference.

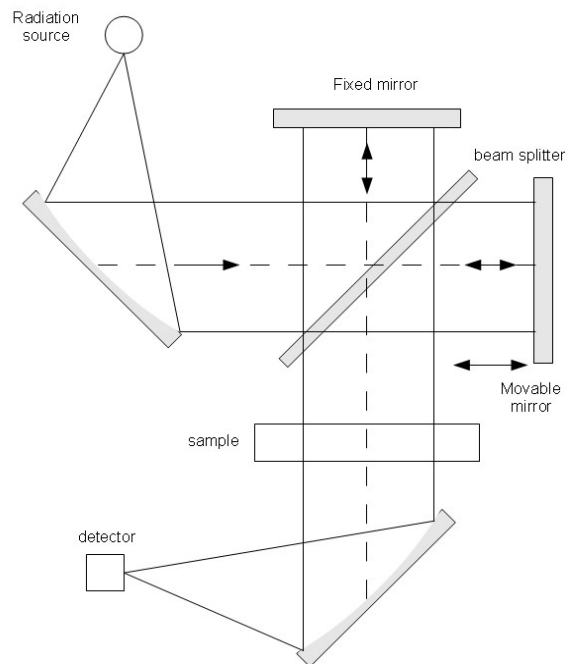


*Figure 2.6: Schematic diagram of Fourier transform spectrometer with a classical Michelson interferometer (Günzler 2002)*

For a monochromatic radiation source the interferogram recorded is of cosine form:

$$I(x) = I_0 \{ 1 + \cos(2\pi \tilde{\nu} x) \} \quad (2.9)$$

Constructive interference occurs when the arms of the interferometer have the same optical path, i.e. no phase difference, and the electric waves add up. The constructive interference is repeated when the optical difference is an integer number of the wavelength. While the destructive interference occurs when the movable mirror is moved by  $\lambda/4$  which makes the retardation between the beams a path difference of  $\lambda/2$  results in quenching interference at the detectors. The destructive interference is repeated whenever the optical path difference is  $\lambda/2$  multiplied by an integer number. For a polychromatic radiation the interference pattern corresponds to the sum of the cosine signals of all individual frequencies.



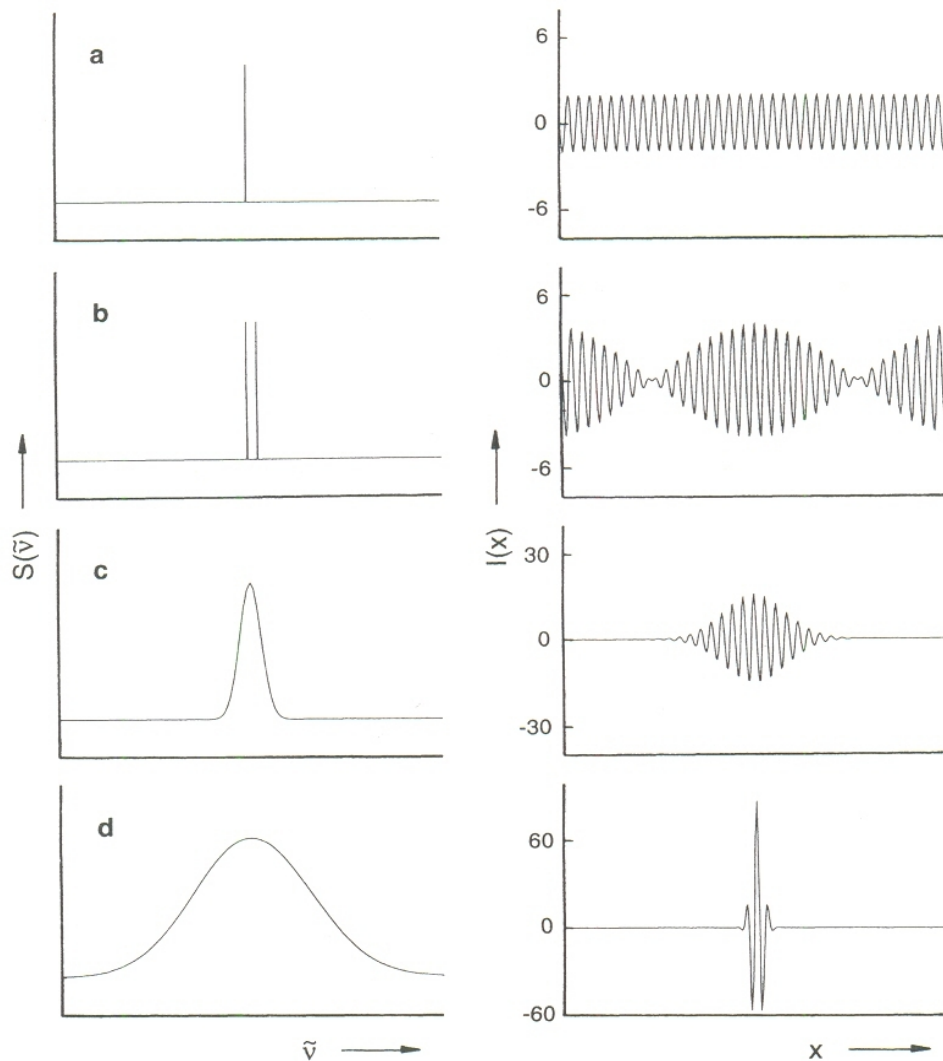


Figure 2.7: Spectra (on the left) with corresponding double-sided interferograms (on the right) a) monochromatic radiation b) two narrow-band emission lines c) band-pass filtered thermal radiation d) broadband thermal radiation (Günzler 2002).

Figure 2.7 shows the interferograms of various spectra. When the optical path length between the mirrors is zero, the position is known as zero path difference (ZPD) where all the wavelengths have constructive interference at the same point. Ideally the phase of all the wavelengths for broadband spectra, the maximum of the interferogram, drops rapidly. The obtained symmetrical interferograms is converted by Fourier transformation into a spectrum.

$$S(\tilde{\nu}) = \int_{-\infty}^{\infty} I(x) \cos(2\pi \tilde{\nu} x) dx \quad (2.10)$$

The interferogram is not recorded continuously but it is sampled and digitized at certain points to allow the computer process the data. The interference pattern of a He-Ne is simultaneously detected and the zero crossing of the He-Ne laser sine or a multiple of these intervals define the retardation points. Because of the He-Ne mode structure, the frequencies of it vary a little bit ( $<0.01 \text{ cm}^{-1}$ ). That means only for the high resolution IR spectroscopy stabilized single mode lasers are used.

## 3 Experimental setup

### 3.1 Introduction

An ideal surface system used in interface physics is different from a surface under atmospheric pressure. A clean surface exposed to the atmosphere is a very complex and not well defined system because it is very active to the atoms and molecules impinging on it. A lot of different adsorbed molecules may be found within the topmost adlayers on the topmost atomic layer of a surface. A monolayer of gases would be created in the atmospheric pressure on the surface within  $10^{-9}$  s. This adlayer has not a well defined chemical composition and geometrical structure, so it is considered as contamination layer. This contamination layer hinders the controlled adsorption of single and pure selected species. The preparation of a clean uncontaminated surface is the first step required before a well defined adsorbate of known consistency and quantity impinges on the surface. In the same way, a clean and crystallographically ordered substrate material is required to produce an epitaxy in a well controlled way. All the above points are good reasons to relocate the experiments in a UHV chamber. Another good reason to use the UHV is the use of low energy electron- and ion-based experimental techniques without having to deal with gas phase scattering.

### 3.2 The UHV chamber and the spectroscopic methods

The UHV system used in this work is shown in Figure 3.1 consists of four parts: The main chamber, the parking station, a load lock system and an STM chamber. The load lock was used to enter the crystals to the chamber without exposing the main chamber to the atmosphere. The sample is stored in the parking station. The main chamber is mounted on a wheeled frame and has a spherical shape. An Omniax VG manipulator is installed in the main chamber and used for moving the sample within the chamber in the x, y and z direction to ensure good alignment to different analysing devices. The cooling finger is mounted in a rotational feed through which gives freedom to rotate the sample  $360^\circ$  around the z axis. Several standard analysis techniques are included in the UHV chamber used in this work which are LEED, TPD, an electron beam evaporator and FTIRAS. These methods are necessary to prepare the sample Pt/Al<sub>2</sub>O<sub>3</sub>/NiAl(110).

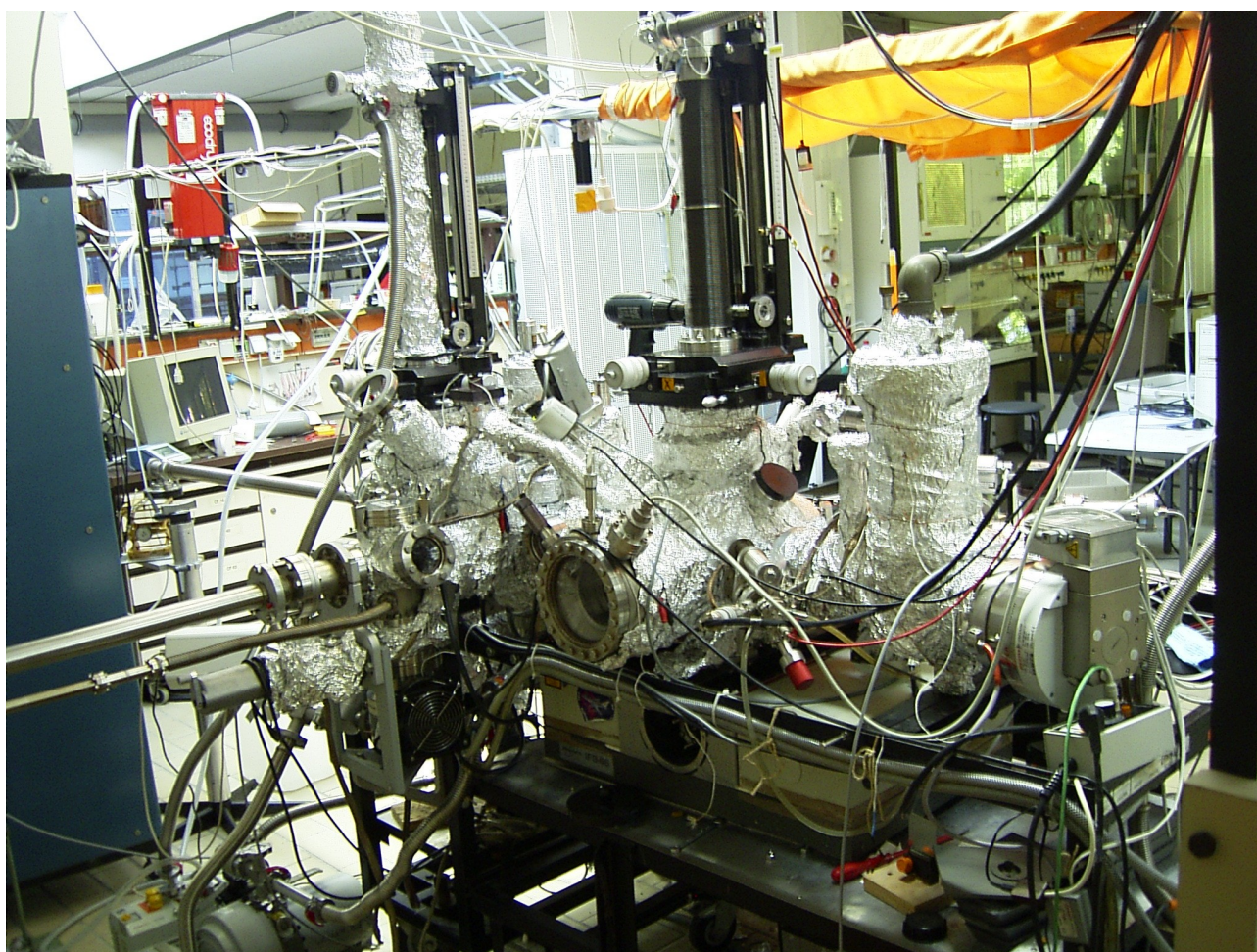


Figure 3.1: The UHV Chamber used in this work

A sputtergun has been installed and used as ion source to clean the crystal. It has a gas inlet which is fed with argon as an ion source controlled by a finepointed tip. After ionizing the argon gas, a high voltage is applied to the ion source with the sample lying on ground potential to accelerate the ions to achieve certain impetus to the ions and to remove the topmost bulk atoms from the sample. This is the cleaning mechanism. After the sputtering, the sample was annealed to 1300 K to smoothen the rough surface.

The sample surface needs to be characterized after the cleaning process. A four-grid LEED (ErLEED 1500) from Specs with associated power (ErLEED-A) was used. The LEED optics have been equipped with a z displacement to set the optical distance to the sample. The electron energy between 50 and 200 eV was used to obtain characteristic LEED images. The chamber is connected to a gas system which contains a gas line connected to the gas bottles like O<sub>2</sub> and Ar and CO by valves. The Ar was used to clean the sample and the O<sub>2</sub> to oxidize the sample. The gas line was

connected to a prevacuum pump and to a turbo pump to evacuate the line from the residual gases and to control the flow of the gases to the chamber. A water cooled electron beam evaporator (Tetra) equipped with a platinum rod was used to deposit platinum. A mechanical shutter in the electron beam evaporator was used to start and stop the deposition process. A constant evaporation flow was monitored by using a flow monitor (Tetra) to determine the proportion of the ionized particles in the evaporator.

The thickness of the deposited Platinum was calibrated using a quartz micro balance and quartz crystal monitor IL 150 (produced by Intellectrics Ltd.).

The CO adsorption on the sample surface was accomplished by using the gas system. The gas line used to dose the CO is connected to the chamber by a tube with an aperture of 10 microns. This gas system is filled with the adsorbate via a variable leak valve. A turbo pump (Pfeifer TMU 071P) was connected to the dosing line to evacuate the gases from the dosing line and also connected to another valve to evacuate the gas line. A prevacuum pump is connected by a valve to the gas line for preevacuation.

Underneath the main chamber a small chamber is located for use in FTIR experiments. It consists of a T-piece with four DN40CF view ports. The main chamber is equipped with three viewing ports which gives good view to relocate the sample to the IR chamber by means of the manipulator. An infrared spectrometer (BRUKER IFS66s) is installed on a separated mobile table with an adjustable height. This arrangement gives the possibility to remove the spectrometer to bake the chamber and flexibility to align the IR spectrometer to the IR chamber. Optimal reflection was achieved by adjusting the position of the sample using the manipulator. The IR chamber protrudes into the sample compartment of the IR spectrometer.

A turbo-molecular pump (Pfeiffer TMU 521) was used to achieve ultra high vacuum in the chamber with a dry scroll backing pump (Edwards XDS 10). The pumps were also used to differentially pump the rotational feed through of the manipulator. A Titanium sublimation pump from Varian was used to remove the hydrogen molecules which is very difficult to be removed by the turbo pump especially in the lower pressure range. A cold cathode pressure gauge (Pfeiffer range  $10^{-2}$  to  $5 \cdot 10^{-11}$  mbar) was installed in the main chamber. The pressure inside the chamber was  $1 \cdot 10^{-10}$  mbar after cooling the sample to 85 K by liquid nitrogen.

A damper was installed between the chamber and the scroll pumps to compensate the vibrations between them. Computer aids located in a rack near the chamber were used to control the various components.

### 3.2.1 Sample holder

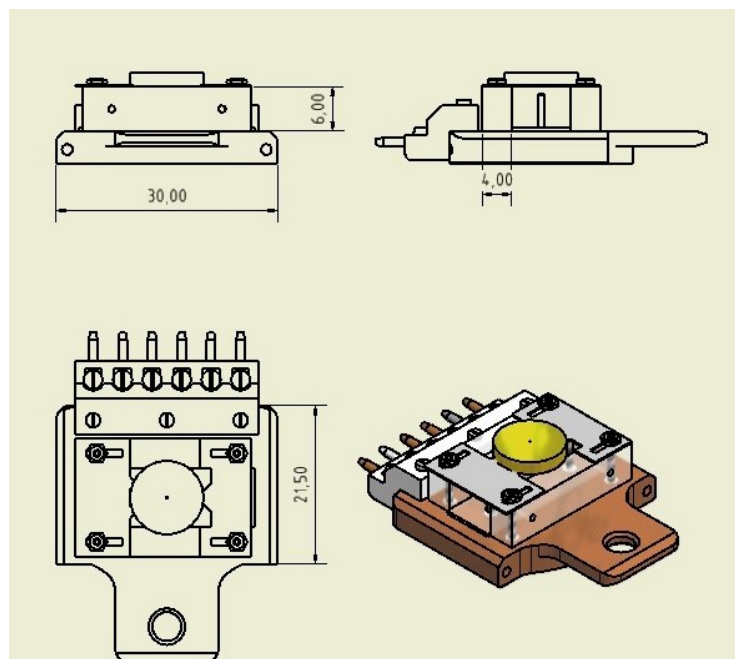


Figure 3.2: Schematic diagram of the sample holder

As shown in Figure 3.2 the sample holder consists of a copper semi rectangular piece which is a platform to install the other parts of the sample holder. Three pieces of sapphire were used in the sample holder. Two pieces have to carry the sample and the third piece is a thin sheet used to isolate the heat of the tungsten filament from the copper base. This heat is necessary to heat the sample installed on the copper platform to carry the sample. Tantalum sheets were used to clamp the sample on the sapphire. The reason of using Tantalum is its high melting point which is necessary because the temperature used to prepare the sample could reach 1300 K. The sapphire was used because it exhibits very good thermal conductivity specially at low temperatures which is necessary for cooling the sample. Two screws made from molybdenum were installed on the copper platform by using an isolating plug socket which lay directly under the sample. A tungsten filament



was fixed between the two molybdenum screws under the sample. It is used for heating the sample to high temperatures. To control the sample temperature a thermocouple was spot welded on the side of the sample. The sample was electrically isolated from the sample holder and the main chamber, in other words the ground of sample was isolated from the ground of the sample holder (which is, as the complete chamber, at ground potential). The electrical connections of the tungsten filament, the thermocouple and the sample ground were connected to pins attached on a socket. This pin socket is plugged to the cooling finger with the corresponding bushings of these pins. Then wires were used to connect these female connectors to the electrical feedthroughs out of the UHV. The sample holder was attached to a cooling reservoir filled with liquid nitrogen.

### 3.3 IR experiment

FTIR spectra were recorded using a BRUKER IFS66 spectrometer. It is purged with dry air using a Zander KM-25 air dryer. A narrow band MCT detector (D 316, BRUKER) is attached to the spectrometer. To obtain a high signal to noise ratio, the MCT detector was cooled by liquid nitrogen. The signal to noise ratio was 20 000 for a 4 mm aperture. A silicon carbide lamp is used as IR source. The Michelson interferometer in the IR spectrometer contained a  $\text{CaF}_2$  beam splitter and a mirror with 20 KHz speed. "OPUS" BRUKER software was used to control the spectrometer. The converted information from time domain to frequency domain was implemented with  $2 \text{ cm}^{-1}$  resolution.

Resolution:  $2 \text{ cm}^{-1}$

Mirror speed: 20 KHz

Measurement time: 5 minute

Aperture: 3.5/ 7 mm

Signal amplitude: 20 000

The acquisition spectral range extends from  $400 \text{ cm}^{-1}$  to  $4000 \text{ cm}^{-1}$  but the interesting region for the experiments in this work is between  $1800 \text{ cm}^{-1}$  to  $2250 \text{ cm}^{-1}$  which is the vibrational region of the adsorbed CO molecules. Because of the purged dry air is not 100% free from water vapor and the

water condensed on the  $\text{MgF}_2$  window of the MCT detector, the presented spectra were smoothed by 9 (number of the smoothing points) to reduce the noise present in the spectra.

Figure 3.1 shows how the spectrometer was aligned to the UHV chamber. Two KBr view ports have been installed in the T-piece of the IR chamber to allow the IR radiation to enter the IR chamber and to be reflected from the sample aligned to a grazing incident angle of  $84^\circ$ . The IR was incident to the detector windows. A  $\text{MgF}_2$  view port has been installed perpendicular to the sample surface which is transparent to the UV radiation. The laser beam will enter through this view port into the T-piece chamber and will hit the surface of the sample.

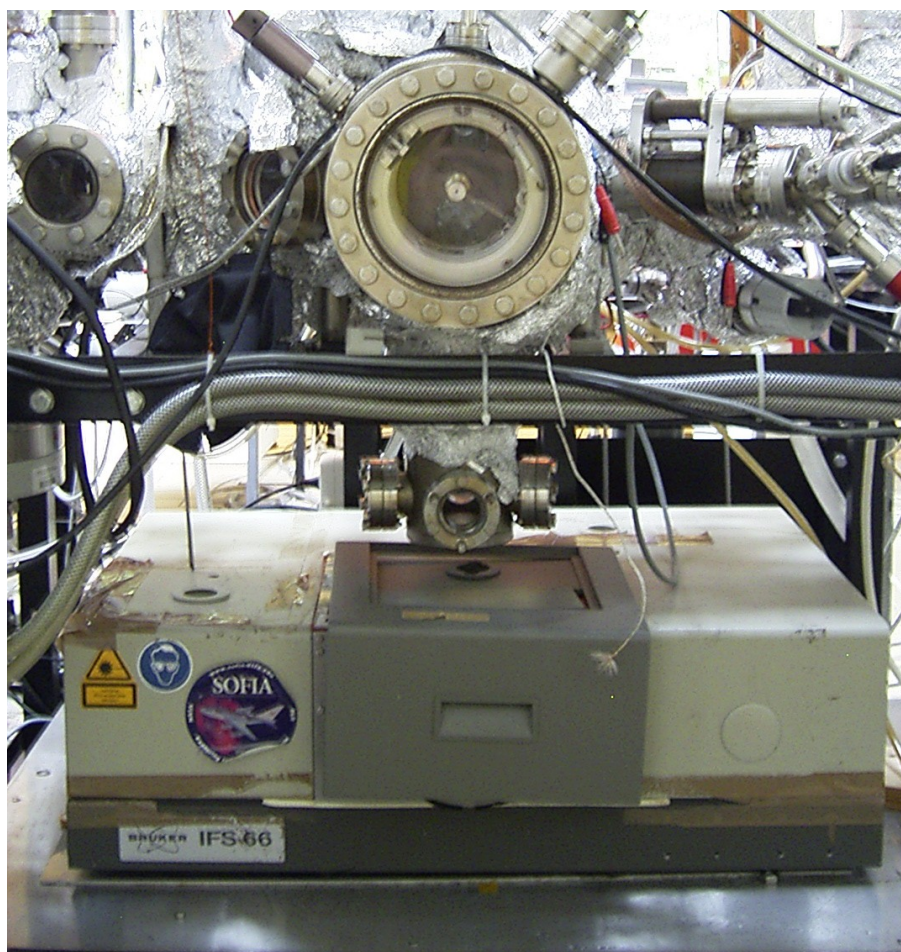


Figure 3.3: FTIR spectrometer under the chamber



### 3.4 TDS

The mass spectrometer used in the thermal desorption spectroscopy was a quadruple mass spectrometer (Pfeiffer QMS 200 Prisma). It was attached to a Feulner cup which can be driven using a z-shift towards the sample. The cup tapers have the dimensions of a 40 mm tube with a 12 mm wide tip welded to a 5 mm pinhole to ensure that only the molecules that desorb from the sample surface will be measured by the mass spectrometer.

The mass spectrometer head and the main chamber is connected by a differentially pumped bypass line to prevent the gas molecule to be accumulated in the mass spectrometer. An Ohm meter is used to detect how close the head of the mass spectrometer is to the sample surface. As soon as the Ohm meter indicates a closed loop which means that an electrical current flow has been accomplished between the sample surface and the head of the spectrometer, the head of the spectrometer is pushed 0.1 mm back from the sample.

The heating power and the temperature in the TPD experiments were controlled by a power supply (Bestec). A built in PID controller (Eurotherm 2408) controls the linear heating rate which is chosen to be 0.66 K/s. A thermocouple is used to read out the sample temperature. This reading will be integrated directly with the data of the desorbed molecules captured by the QMS. The  $m/e$  of 2 ( $H_2$ ), 18 ( $H_2O$ ), 28 (12  $CO$ ,  $N_2$ ), 44 ( $CO_2$ ) were detected. These masses were sequentially recorded with a time resolution of 0.5 second. The detected currents were within the range from  $10^{-12}$  Ampere to  $10^{-8}$  Ampere. Because of overshooting and oscillating in the power of the filament, a peak is found at the first 5-6 points in the TPD.

### 3.5 Scanning methods

An evacuated Atomic force microscopy from Veeco inc. was used in this work. The sample was extracted for the preparation chamber and scanned by the AFM in tapping mode. Also a STM from Omicron was used in this work. The sample was prepared in the main chamber and it has been transferred to the STM chamber by an evacuated mobile chamber.

### 3.6 Nanosecond Laser

The photoinduced processes for the model catalyst system CO/Pt/Al<sub>2</sub>O<sub>3</sub>/NiAl(110) were investigated using a nanosecond Nd:YAG laser from Spectra Physics (Quanta Ray GCR-130). The third harmonic at 355 nm is used in this work and is generated by passing the fundamental Nd:YAG laser to a nitrogen purged nonlinear KDP crystal. Dichroitic mirrors are used to separate the generated wavelengths from the fundamental wavelength which will be damped by a laser damper. The Nd:YAG is set to the optimal Q-switch mode to get the highest fundamental energy required for the third harmonic generation. The laser beam is aligned to the sample by two prisms. The prisms provide freedom to control the height and the direction of the beam.

### 3.7 Sample preparation

During this work two different single crystals were used for the experiments. The first is a NiAl(110) crystal which is used for the preparation of the sample Pt/Al<sub>2</sub>O<sub>3</sub>/NiAl(110), the second crystal is Pt(111) which is used as comparative model for laser induced CO desorption.

#### 3.7.1 Pt/Al<sub>2</sub>O<sub>3</sub>/NiAl(110)

The preparation of the epitaxial alumina film is described in the literature (Jaeger *et al.* 1991). The cleaning of the NiAl(110) single crystal was initiated by repeated sputtering and oxidation cycles. The sample sputtering was done by filling the chamber with argon at  $5 \cdot 10^{-5}$  mbar, heating the sample to 670 K and using 1 kV accelerating voltage. The sputtering current was 5  $\mu$ A at the sample for one hour. After the sputtering, the sample was annealed in a first step to 1070 K for 20 minutes. For the second step annealing the sample temperature was set to 1220 K for 10 minutes. Afterwards the sample was checked by using LEED. In case the LEED showed the typical pattern

for clean NiAl(110), then the oxidation process could be started. The oxidation was achieved by heating the sample to 550 K and filling the chamber with oxygen up to a pressure of  $10^{-6}$  mbar. The amorphous alumina film was transformed into crystalline alumina by annealing the surface by heating to 1120K for 5 minutes. The quality of the alumina was tested by using LEED. After checking the quality of the alumina, the evaporation process was started. A platinum rod was installed in a water cooled electron beam evaporator EBV20 from Omnicvac. The flux of the platinum was measured directly through the current of the produced ions. This allows an accurate flux adjustment and much faster rate control. The beam exit column contains the ion collector electrode which is used as a flux monitor. At a given electron emission current and beam energy the ion flux measured there is directly proportional to the evaporated atom flux. The evaporator is water cooled. The aperture of the evaporator has a manual controlled shutter. By opening and closing this shutter, the beginning and the end of the evaporation process was controlled.

A tungsten wire which surrounded the tip of the Platinum rod was used as electron source by heating it with 2 Ampere. These electrons were accelerated to 1000 Volt.

The quartz micro balance was aligned perpendicular to the direction of the evaporator. The amount of the deposited platinum was calculated as a function of the time. When the evaporator reached a stable rate of evaporating platinum the sample was aligned to face directly the direction of the evaporator.

The temperature of the sample during the evaporation was 300 K. The calibration of the amount deposited was done with the aid of a water cooled quartz microbalance (Tetra, accuracy: 0.01 nm/s rate, 0.1 nm mean thickness). The change of the oscillation frequency of the crystal is proportional to the density, acoustic impedance and thus the quantity of the deposited material. By providing the density the thickness of the platinum can be calculated very easily.

### 3.7.2 Pt(111)

The Pt(111) crystal was used as a comparative model to the Pt/Al<sub>2</sub>O<sub>3</sub>/NiAl(110) system for photoinduced desorption. The crystal was prepared for CO adsorption experiments. First the Pt(111) single crystal was installed in the same sample holder that carried the NiAl(110) single crystal. The Pt(111) was heated to 670 K and the chamber was filled with Argon to a pressure of  $10^{-5}$  mbar for

sputtering the sample. After that the sample was annealed to 1200 K for one minute. Several cycles of the sputtering process were needed to obtain a clean crystal surface. The LEED was used to decide about the quality of the crystal surface by the sharpness of the spots with minimum background. When the typical (1x1) LEED patterns were good, CO adsorption experiments were done.

## 4 Structure and properties of the model catalyst Pt/Al<sub>2</sub>O<sub>3</sub>/NiAl (110)

### 4.1 Introduction

Aluminum oxide is one of the most important supports for dispersed metal catalysts. The electron spectroscopic characterization is very essential, if one intends to carry out model studies on well ordered oxide surfaces. For such studies a thin oxide film on a metal support is created with a well defined geometric and electronic structure identical or close to the properties of the bulk oxide.

In principle there are two ways to prepare an ordinary oxide surface. The first way is to use surfaces of oxide single crystals. In this way samples with a low defect density can be prepared (King *et al.* 1990). But charging problems restrict the use of some methods like electron spectroscopy. The second possible way is to grow an epitaxial oxide surface over a metallic single crystal (Bäumer *et al.* 1991, Cappus *et al.* 1993).

Concerning aluminum oxide it is known that it is possible to prepare thin films on top of aluminum single crystal surfaces (Erskine & Strong 1982, Strong *et al.* 1982, Crowel *et al.* 1986, Chen *et al.* 1987, Chen *et al.* 1987a), but unfortunately these films do not exhibit a well-ordered geometric structure, ie. they form amorphous oxide layers, due to the low melting point of the aluminum single crystal (Bäumer *et al.* 1997). Therefore NiAl is used (Chen *et al.* 1990, Chen & Goodman 1994). The oxidation of the (110) surface of the body centered alloy NiAl leads to the formation of a well-ordered aluminum oxide film (Doychak *et al.* 1989, Isern & Castro 1989). Another advantage of thin films compared to the use of oxide single crystals is its high reflectivity for infrared radiation so that FT-IRRAS can be used with high sensitivity (Guillamet *et al.* 1992).

## 4.2 Electronic and geometric structure

A characteristic LEED pattern of the oxidized NiAl(110) surface shows large numbers of sharp spots additional to the substrate spots (Jaeger *et al.* 1991, Libuda *et al.* 1994) is shown in Figure 4.1.

Because of the two-fold symmetry of the substrate, as shown in Figure 4.2, the formation of two domains A and B rotated by  $\sim 48^\circ$  to each other can be observed.

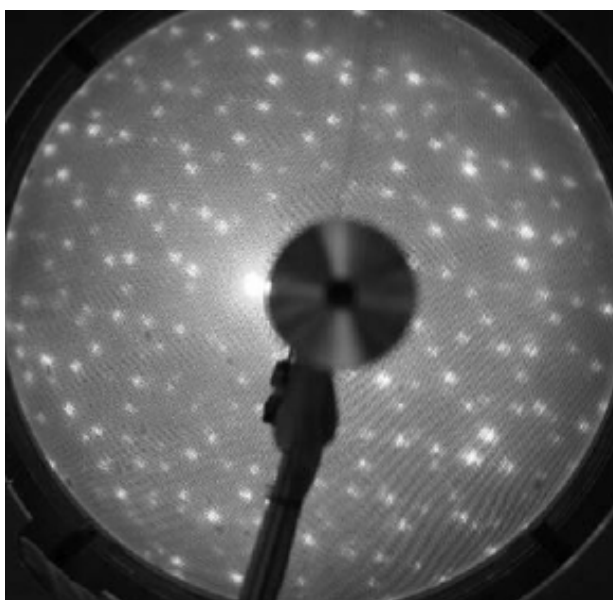


Figure 4.1: LEED pattern of Al<sub>2</sub>O<sub>3</sub>/NiAl(110)

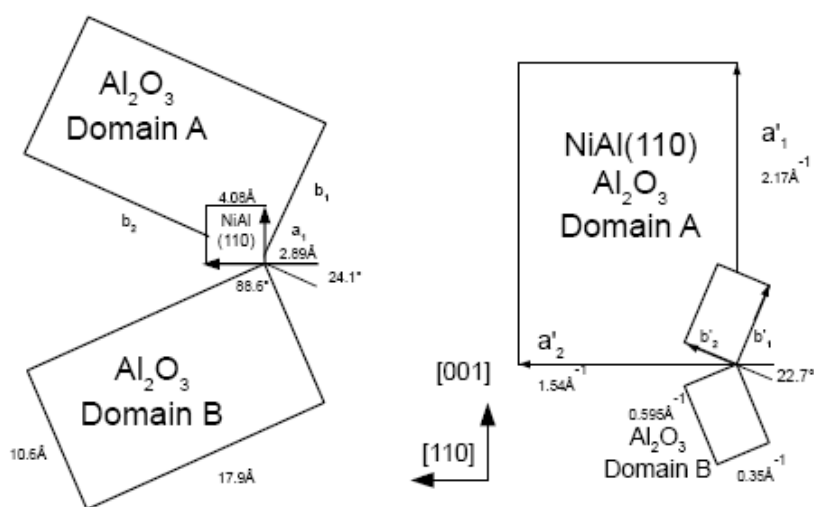


Figure 4.2: Dimension of the Al<sub>2</sub>O<sub>3</sub>/NiAl(110) unit mesh and orientation with respect to the substrate in the real space. (Libuda *et al.* 1994)

Jacobs *et al.* (1994) have proven that the film does not contain any Ni by using ion scattering spectroscopy (ISS) and photo emission as shown in Figure 4.3.

Using EELS it was shown that the oxide is  $\gamma$ -alumina-like. The aluminum ions reside in tetrahedral and octahedral sites (Jaeger *et al.* 1991). Klimenkov *et al.* (1997) agrees that the oxide is like  $\gamma$ -alumina by using TEM. The estimated thicknesses of the alumina is about 5 Å which refers to an oxygen double layer by using Auger electron spectroscopy (AES) and LEED (from the damping of the spots) (Jaeger *et al.* 1991, Isern & Isern 1989).

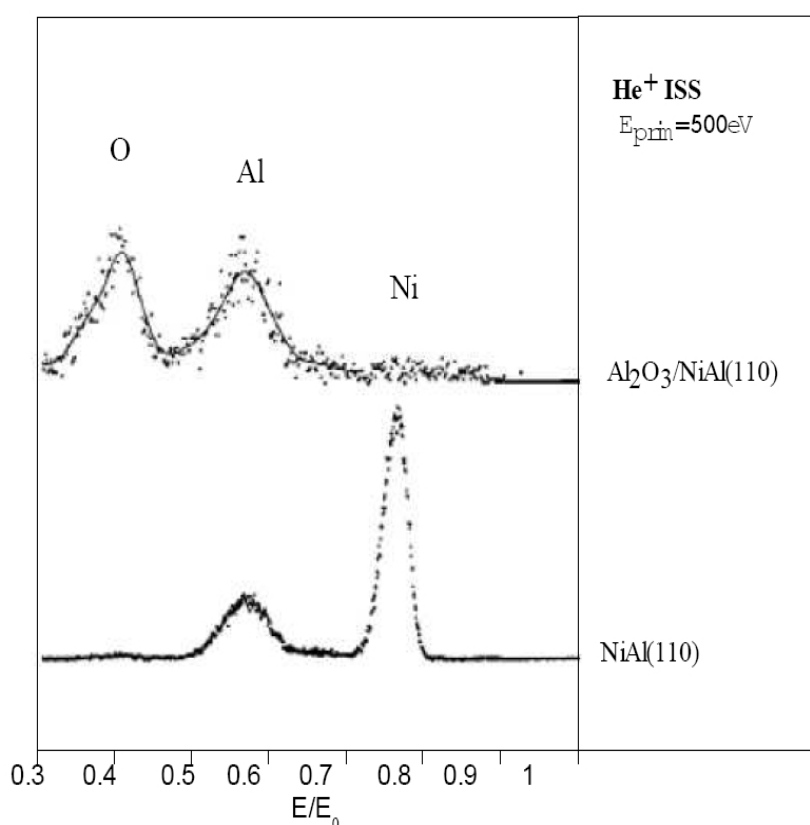


Figure 4.3: He<sup>+</sup> ion scattering spectra of the clean and oxidised NiAl(110) surface. (Jacobs 1994)

From the characterization of the adsorption properties of the alumina for some molecules it was found that it exhibits weak interaction (Jaeger *et al.* 1991, Jaeger *et al.* 1993). The CO desorbs from the alumina between 30 and 70 K as shown in Figure 4.4 which is a TDS spectrum for CO adsorption.

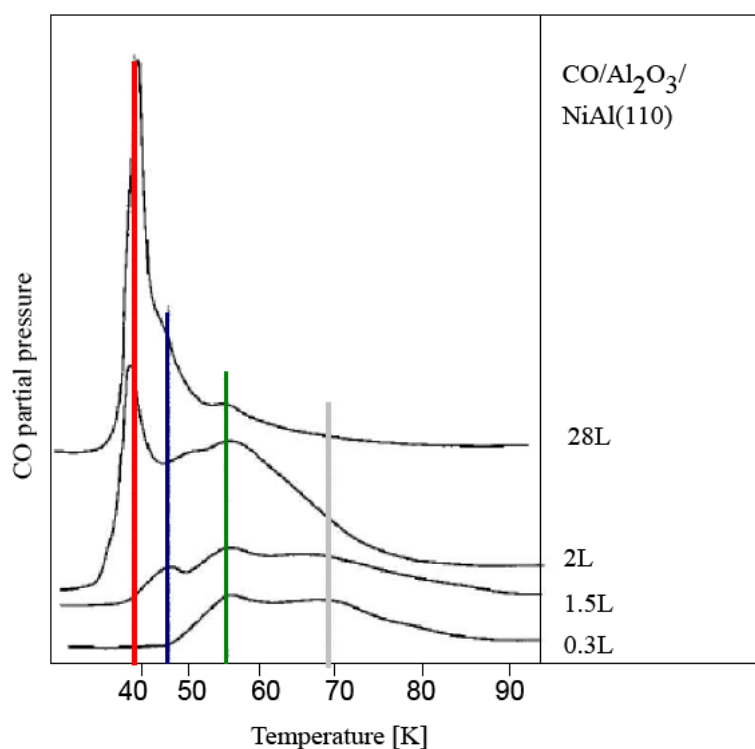


Figure 4.4: Thermal desorption spectra of the system CO/Al<sub>2</sub>O<sub>3</sub>/NiAl(110) (heating rate:  $\sim 0.3$  K/s). (Jaeger *et al.* 1993)

### 4.3 Nucleation and growth at different temperatures

In order to prepare a model catalyst of nanoparticulate particles on the oxidic support metal atoms are evaporated onto the surface. The first step is the adsorption of the incoming platinum atoms on the surface. The surface should accommodate thermally the metal atoms sticking to the surface, if they were not scattered elastically. But it could be safely assumed that all the deposited atoms will stick because no elastic scattering was observed (Henry 1998, Campbell *et al.* 1997). The sticking probability might be less than one because not all the deposited metal atoms will stay on the surface because of the re-evaporation especially at higher substrate temperature. At room temperature it has been shown that many transition metals on oxides condensed completely (Zhou *et al.* 1993, Xu & Goodman 1992). As soon as the deposited atoms adsorb on the surface, they will start to move on the surface depending on their diffusion coefficient:



$$D = \frac{1}{4} (v_o a^2) \exp(-\varepsilon_{Diff} / kT) \quad (4.1)$$

Where  $\varepsilon_{Diff}$  is the activation energy for diffusion (which usually scales with the adsorption energy),  $v_o$  is the prefactor,  $a$  is the distance between two adjacent adsorption sites,  $T$  is the temperature and  $k$  is the Boltzmann constant. In order to travel a distance  $l$ , they need an average time, which is then given by:

$$\tau = l^2 / (4D) \quad (4.2)$$

Heterogeneous nucleation is the name for a growth process in which the adatoms are trapped at the defect sites presented on the surface and forming nuclei necessary for this type of growth. Homogeneous nucleation is the name for the growth mode when the adatoms aggregate on normal sites. The critical cluster size is the minimum number of diffused adatoms which will grow.

The diffusion coefficient and the vapor flux  $F$  are effecting the saturation density of nuclei  $N$  in homogeneous nucleation. One atom of a critical cluster size means that a dimer is stable and the following proportionality is derived (Campbell *et al.* 1997)

$$N \sim (F/D)^{(1/3)} \quad (4.3)$$

(A more general derivation yields  $i/(i+2)$  for the exponent, with  $i$ =critical cluster size (Venables *et al.* 1984).

The saturation density is independent of the diffusion coefficient and the flux when the heterogeneous nucleation is dominant. It would be independent, too, in homogeneous nucleation when the attraction between adatoms and defects  $<$  distance  $L$  between islands  $L = (1/N)^{(1/2)}$  (Giorgio *et al.* 1997, Henry 1998).

When the saturation density of the particles is achieved, there will be no more nucleation and all the adatoms will diffuse until they are captured from an existing island or the adatoms might land directly on an island when its size is large enough. For a given combination of a metal and an oxide

the surface free energies of the metal,  $\gamma_{\text{metal}}$ , the oxide,  $\gamma_{\text{Oxide}}$ , and the free energy of the metal-oxide interface,  $\gamma_{\text{Interface}}$  can reveal from thermodynamic aspect what the growth mode (2D or 3D) or the island will be for a given combination of a metal and an oxide (Venables *et al.* 1984, Zinke-Allmang 1992).

$$\gamma_{\text{Interface}} + \gamma_{\text{Metal}} < \gamma_{\text{Oxide}} \quad (4.4)$$

According to a layer-by-layer growth mode (Frank-van-der-Merwe growth mode), the metal wets the oxide at equilibrium. When the sum of  $\gamma_{\text{metal}}$  and  $\gamma_{\text{Interface}}$  is larger than  $\gamma_{\text{Oxide}}$ , the formation of thick 3D aggregates (Volmer-Weber growth mode) metal is expected. So Eq. (4.4) explains that a layer-by-layer growth mode mostly is an exception because surface free energies of metals are mostly larger than free energies of oxides (Campbell *et al.* 1997, Overbury *et al.* 1975). The 3D particle growth is very likely. This has been observed in many experiments depositing metals on oxides.

In the case of a Volmer-Weber growth mode, the equilibrium shape of the aggregates can also be predicted. As shown in Figure 4.5, it is a Wulff polyhedron truncated at the interface in accordance with the following equation (Henry 1998)

$$\Delta h / h_i = E_{\text{Adh}} / \gamma_{\text{Metal}(i)} \quad (4.5)$$

where  $\gamma_{\text{metal}}$  is the surface free energy of the corresponding crystal face and  $E_{\text{adh}}$  is the adhesion energy, given by Chatain *et al.* (1988)

$$E_{\text{Adh}} = \gamma_{\text{Metal}(i)} + \gamma_{\text{Oxide}} - \gamma_{\text{Interface}} \quad (4.6)$$

If the adhesion energy increases, according to eq. (4.5) the particles become flatter. Eq. (4.6) tells that the adhesion energy depends on the strength of the metal-oxide interaction. If  $\gamma_{\text{Interface}}$  will decrease by partial oxidation, the results will be larger values of  $E_{\text{adh}}$  and we can conclude that the

adhesion energy values are correlated with the negative enthalpies of formation of the oxide of the metal (per mole oxygen) (Diebold *et al.* 1995, Peden *et al.* 1991, Persaud *et al.* 1997).

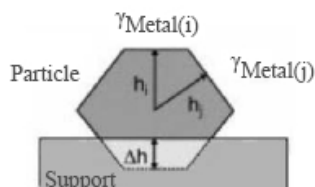


Figure 4.5: Schematic representation of the Wulff-Kaichew construction. (Henry 1998)

The description of the growth might be done within the thermodynamic point of view at elevated temperatures. Because of kinetic limitations, equilibrium normally is not reachable at room temperature.

Campbell's research explains this fact (Campbell *et al.* 1997, Ernst *et al.* 1997, Campbell *et al.* 1994).

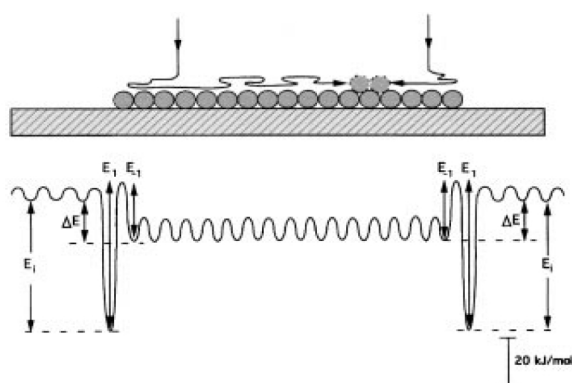


Figure 4.6: Surface potential experienced by a diffusing adatom. (Campbell *et al.* 1997)

The surface  $E_1$  and  $E_{-1}$  are the activation energies for the upstepping and downstepping respectively. The adsorption on a metal island and the oxide is the source of the difference between the energies  $\Delta E$ . Figure 4.6 shows the energy barriers of a metal atom experienced when diffusing along the

surface.  $E_1$  and  $E_{-1}$ . The energy gained by the capture of the adatom at the island edge is  $E_1$  which is an important value in the scheme. The lateral metal-metal bonding induces a strong attraction. It is known that a 2D growth of islands will exist if the upstepping is difficult.

The 3D growth is possible when the islands are large enough. The atoms of the homogeneous nucleation will land on the island and the downstepping will be overcome which makes a start of a second layer growing. The assisted upstepping processes can be the reason of material transport from the substrate level to higher level of the aggregate (Campbell *et al.* 1997, Ernst *et al.* 1993, Campbell *et al.* 1994). An important phenomenon is island thickening (self-thickening) even after the evaporation has been stopped (Campbell *et al.* 1997).

#### 4.4 Growth and Morphology

Several studies have been done to characterize the platinum nanoparticles deposited on alumina. Evidence of a specific metal support interaction was supported by spot profile analysis of LEED (Libuda *et al.* 1994, Winkelmann 1994).

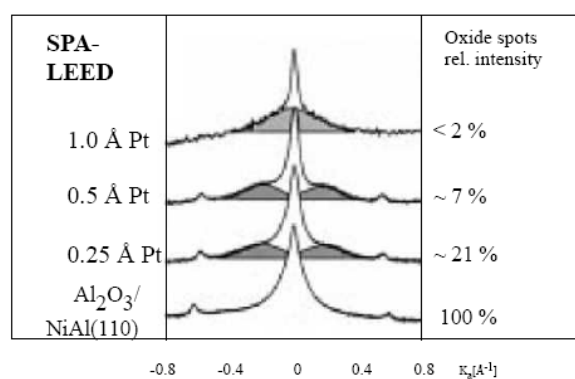


Figure 4.7: Pt/Al<sub>2</sub>O<sub>3</sub>/NiAl(110) comparison of (00) spot profiles after deposition of various amounts of Pt. (Libuda *et al.* 1994a)

Figure 4.7 shows a comparison of (00) spot profiles (45 eV recorded along the [110] direction of the NiAl crystal) after deposition various amounts of Pt measured by Libuda *et al.* (1994).

After deposition of 0.25 Å Pt at 300K which corresponds to a tenth of a monolayer (ML), the

intensity is reduced to 20% from the original intensity. The spots vanished completely after deposition of 1 Å Pt. There was no explanation for the strong attenuation of the oxide LEED pattern even if the 2D growth mode was assumed. A logical reason would be a modification of the substrate vicinity of the deposits resulting in a loss of the characteristic structure of the film.

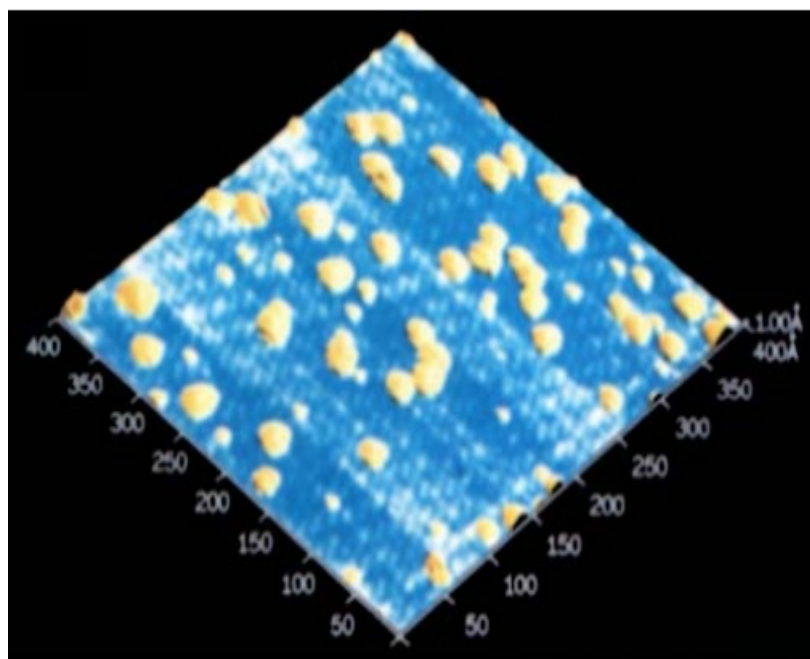


Figure 4.8: STM image (CCT, -4.0 V, 0.8 nA, 400 x 400 Å) of the alumina film covered with 0.25 Å Pt (Bertrams *et al.* 1995)

The results of the SPA-LEED of Pt growth on alumina have been compared with STM results (Bertrams *et al.* 1995). Figure 4.8 shows a STM scan after deposition of 0.25 Å Pt over alumina. Small Pt nanoparticles and the oxide are visible. The line structure is formed by a hexagonal arrangement of protrusions in a distance of nearly 10 Å. The diameters of the Pt nanoparticles are between 10-30 Å with a height of about 1.5 Å and 4 Å for the large ones. The estimated monoatomic islands contain 20-50 atoms. The Pt nanoparticles have been distributed randomly. This is interpreted as strong interaction between the Pt and the alumina and a small diffusion length. The discrepancy of the structural modification of the alumina can be interpreted as the LEED is more sensitive than STM to any small distortions caused by the Pt depositions (Klimenkov *et al.* 1997).

Klimenkov *et al.* (2003) have investigated Pt clusters, prepared at different temperatures on a Al<sub>2</sub>O<sub>3</sub>/NiAl(110) substrate as a function of the effective platinum thickness. Their study supplement TEM investigation in the range of higher coverages, where STM does not yield reliable results.

The Pt was deposited in different thicknesses of 0.2, 0.5, 0.7, 1.0, and 5 ML at 300 K onto

Al<sub>2</sub>O<sub>3</sub>/NiAl(110) substrate. Then the samples were transferred from the UHV to the air to be scanned by TEM “Hitachi-8100” (accelerating voltage of 200 kV and ultimate lattice resolution of 0.144 nm). No change in the Pt clusters happened when the samples were exposed to the air, as proven by Klimenkov *et al.* (1997). The Pt also shows the same behavior when it was deposited on unsupported or supported Pt. When the Pt was deposited onto alumina, the average cluster size increases with increasing the Pt deposition thickness as shown in Figure 4.9.

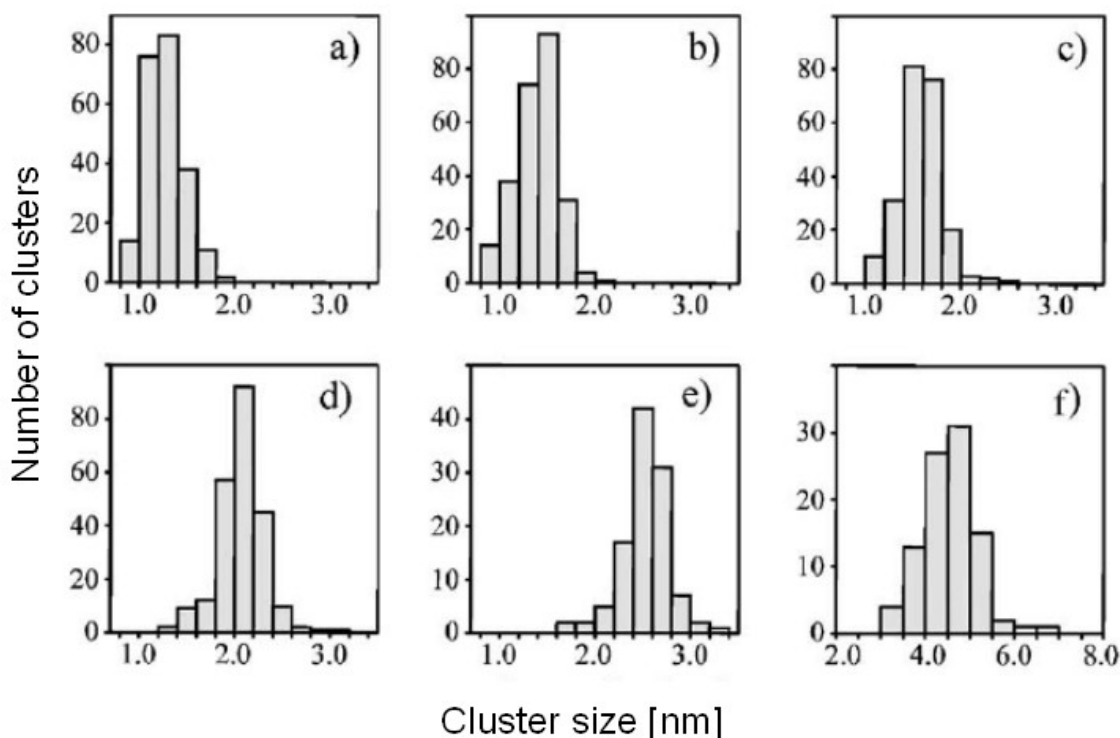


Figure 4.9: Size distributions of Pt particles for effective platinum coverages of  $\Theta_{Pt} = 0.2$  (a), 0.5 (b), 0.7 (c), 1.0 (d), 1.5 (e) and 5 ML (f). (Klimenkov *et al.* 2003)

Characteristic data are listed in Table 1 (Klimenkov *et al.* 2003).

Amount of deposited platinum, ML	0.2	0.5	0.7	1.0	1.5	5.0
Amount of deposited platinum, Å	0.45	1.13	1.58	2.26	3.39	11.3
Cluster density, 10 <sup>12</sup> cm <sup>-2</sup>	7.2	9.8	8.8	6.8	4.3	2.4
Surface coverage, %	9.7	16.2	20.6	21.2	23.1	40.1
Cluster height, nm	0.45	0.70	0.77	1.02	1.37	2.82
Average cluster size, nm	1.23	1.39	1.72	2.07	2.53	4.56

Figure 4.10 shows the results in a comparable way as the average cluster sizes and densities in a clear way. It is shown that as soon as the coverage increases, the average cluster size increases monotonically and at 0.5 ML the cluster density is at maximum. Coalescence of the clusters happens during the deposition of the Pt which points towards Pt homogeneous growth mode on alumina. This type of growth is expected when a strong substrate-cluster interaction is happening. Still the growth mechanism is not clear and more experiments with different Pt thicknesses are needed.

Different cluster growth modes on alumina were found in different metals like Pd and Rh. The STM scans of Pd and Rh depositions at 300 K on alumina show that the clusters are arranged non-homogeneously at the domain boundaries while the growth mode is homogeneous at 77K at points defect.

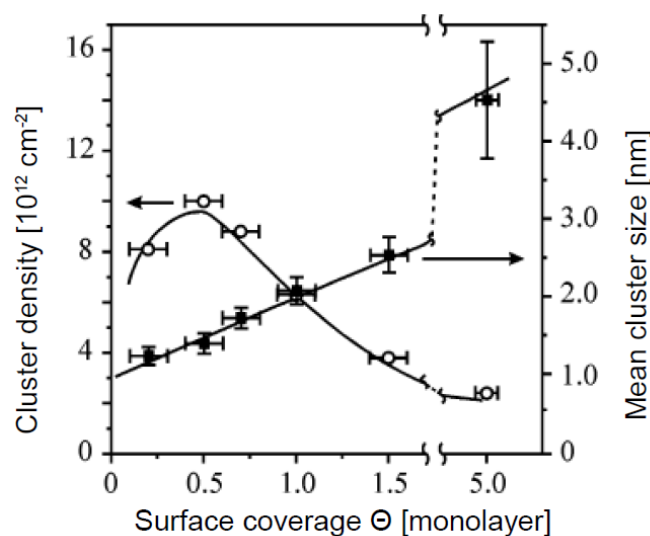


Figure 4.10: Clusters density and mean cluster size as a function of the effective platinum coverage. (Klimenkov et al. 2003)

Silver shows a different behavior than other metals when it is deposited onto the alumina. It grows mainly at step edges which proves a weak interaction with the surface and defects sites. Different growth modes and interactions of metals with alumina though a number of the metals have mostly the same properties.

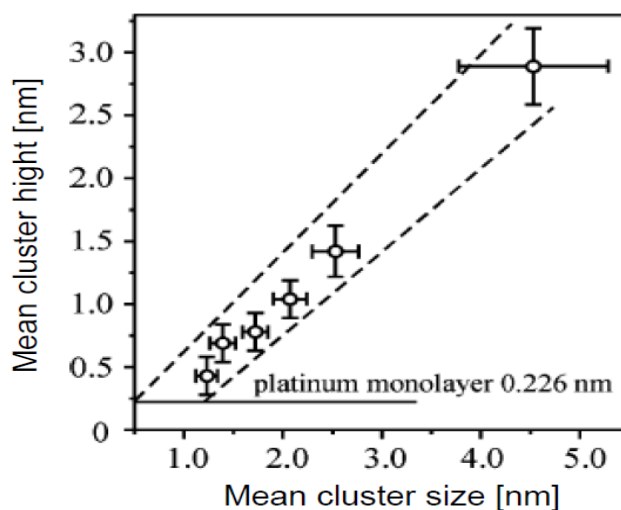


Figure 4.11: Mean cluster height as a function of the mean cluster size. (Klimenkov *et al.* 2003)

Figure 4.11 shows the average of the mean cluster height as a function of the mean cluster diameter of Pt nanoparticles. Klimenkov *et al.* (2003) used two assumptions in order to determine the cluster height. The first is the sticking coefficient of Pt on the Al<sub>2</sub>O<sub>3</sub>/NiAl(110) substrate is unity and the second is that all the Pt atoms are in Pt clusters which are visible by a TEM scan. The presented values of average cluster heights are valid only for planar clusters. The cluster height will be smaller than the calculated if the condensation coefficient is smaller than one. According to this proposal, the estimation of the values deviation between the real one and the calculated one to be in the range of 10% which is the estimated accuracy of the coverage using a quartz microbalance.

There is a linear proportionality between the cluster height and the average size. This shows that the ratio is constant and equal to about  $\frac{1}{2}$ , at least for clusters with a lateral size of more than 1-1.5 nm.



## 4.5 Structural characterization of Pt/Al<sub>2</sub>O<sub>3</sub>/NiAl(110)

The main objective to characterize the deposited Platinum is to get a clue about the dimensions of the platinum particles on the alumina. In this section own AFM scans will be presented. Mainly two different preparation methods were used to deposit Pt on alumina. Two different alumina temperatures were used for the deposition which are 85K, and 300K respectively. The idea to deposit platinum at different alumina temperatures is to test the average island size and island density in connection with the diffusion coefficient. The Pt was deposited in a UHV chamber in different thicknesses. Then the sample was extracted from the chamber and scanned using the AFM under normal pressure.

### 4.5.1 AFM scans of Platinum deposited over Al<sub>2</sub>O<sub>3</sub> at 300K

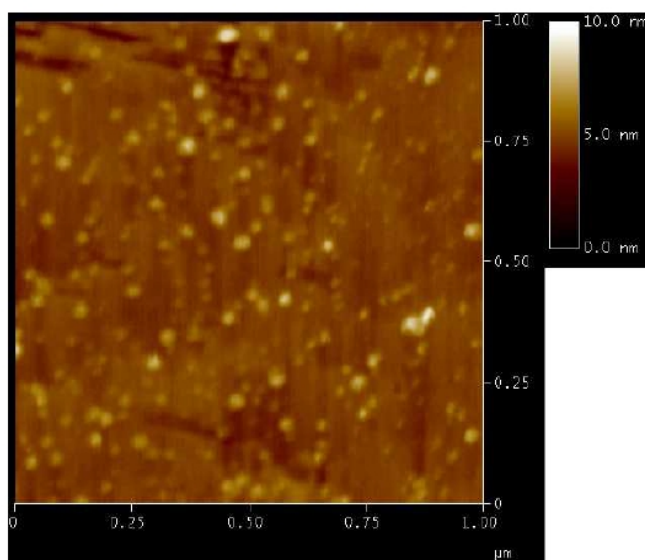


Figure 4.12: Top view of 2ÅPt deposited at 300K/Al<sub>2</sub>O<sub>3</sub>/NiAl(110), image recorded with AFM tapping mode 1x1μm

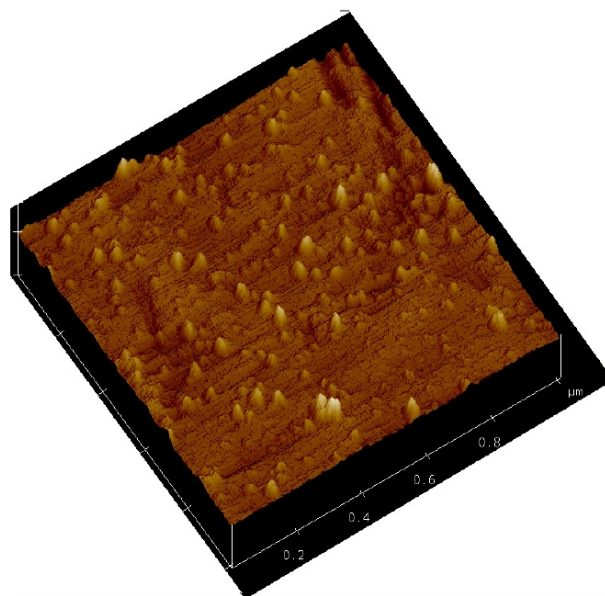


Figure 4.13: 3 dimensional view of 2ÅPt deposited at 300K/Al<sub>2</sub>O<sub>3</sub>/NiAl(110), image recorded with AFM tapping mode 1x1μm

Figure 4.12 and Figure 4.13 show top and three dimensional views of AFM scans in tapping mode with 2ÅPt deposited at 300K/Al<sub>2</sub>O<sub>3</sub>/NiAl(110) respectively. The scan exhibits that the island density is 180 island/square micrometer. The average apparent size of the particles is as follows: radius=66.04 nm height=2.79 nm. It is clear that these islands are very big. The reason will be discussed later.

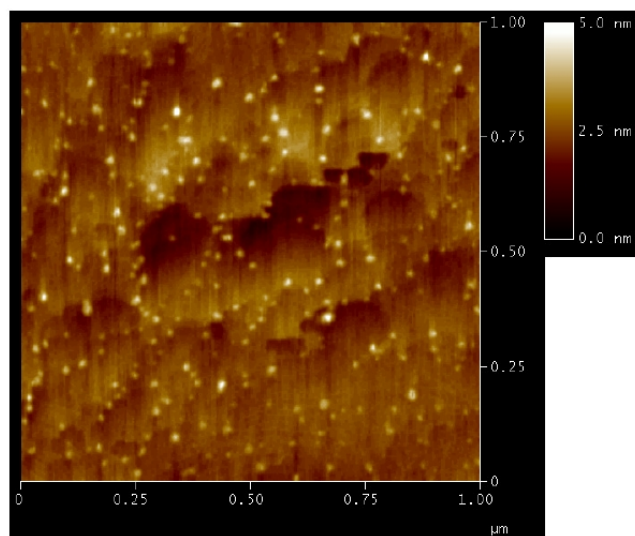


Figure 4.14: Top view of 1ÅPt deposited at 300K/Al<sub>2</sub>O<sub>3</sub>/NiAl(110), image recorded with AFM tapping mode 1x1μm

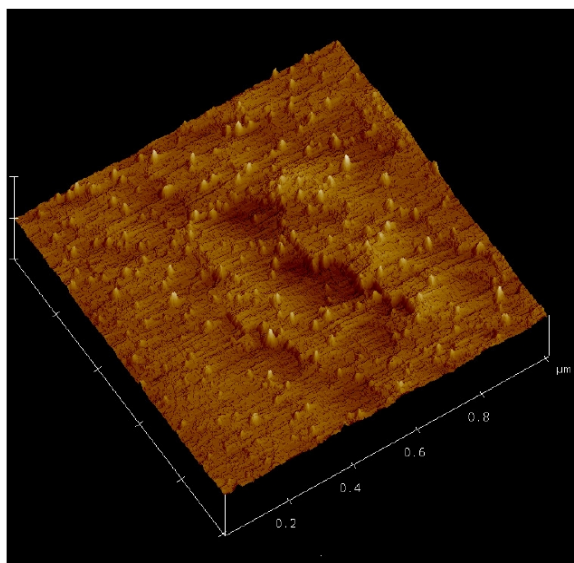


Figure 4.15: 3 dimensional view of 1 Å Pt deposited at 300K/Al<sub>2</sub>O<sub>3</sub>/NiAl(110), image recorded with AFM tapping mode 1x1 $\mu\text{m}$

Figure 4.14 and Figure 4.15 show a top view and a 3 dimensional view of 1 Å Pt deposited at 300K/Al<sub>2</sub>O<sub>3</sub>/NiAl(110). The average of the island dimensions is: radius=32nm and height=1.3nm

Again island sizes are very big and apparently with dimensions nearly of half of the ones in the last experiments. They will be discussed later.

### 4.5.2 Scans of Platinum deposited on Al<sub>2</sub>O<sub>3</sub>/NiAl(110) at 100K

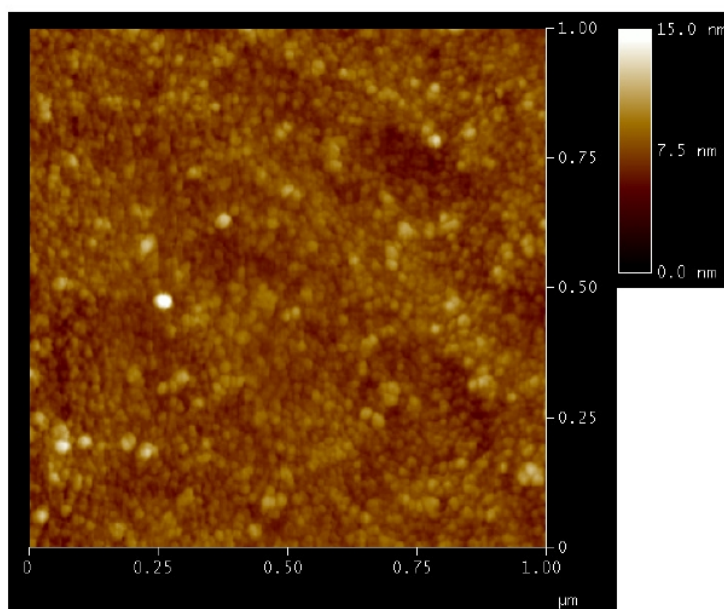


Figure 4.16: Top view of 2ÅPt deposited at 100K/Al<sub>2</sub>O<sub>3</sub>/NiAl(110), image recorded with AFM tapping mode 1x1μm

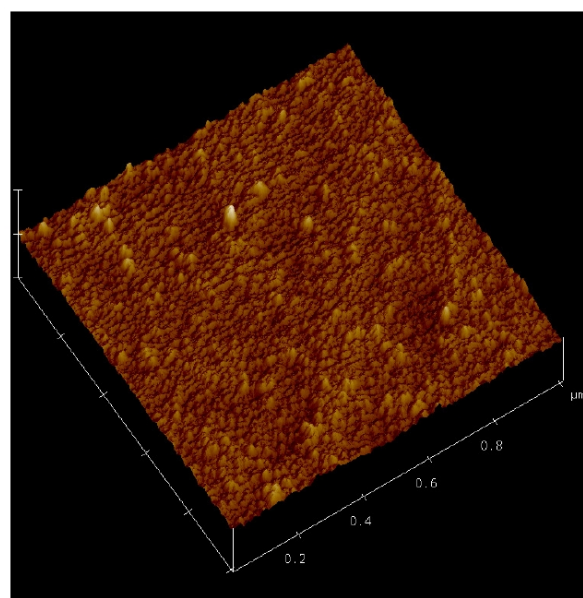


Figure 4.17: 3 dimensional view of 2ÅPt deposited at 100K/Al<sub>2</sub>O<sub>3</sub>/NiAl(110), image recorded with AFM tapping mode 1x1μm

Figure 4.16 and Figure 4.17 exhibit the top view and three dimensional view of AFM image recorded in tapping mode 1x1 $\mu$ m of 2ÅPt deposited at 100K on Al<sub>2</sub>O<sub>3</sub>/NiAl(110). Although Figure 4.16-Figure 4.19 can not be analyzed in detail, it is apparent that at a deposition at T=100K the islands are rather small and have a very high density. The high density of Pt islands points towards a rather strong interaction with the alumina support and a nucleation at local defect sites at T=100K. Such a finding has now been discussed for a larger number of more strongly interacting metal/support systems (Henry 1998, Campbell 1997). As there are no detailed data about aggregate sizes for Pt deposition at T=100K the data presented in this thesis will focus on T=300K deposition.

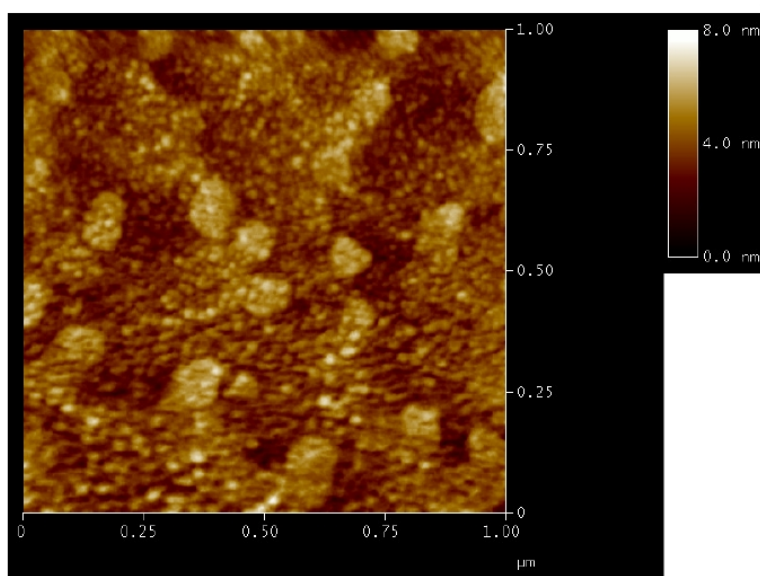


Figure 4.18: Top view of 1ÅPt deposited at 100K/Al<sub>2</sub>O<sub>3</sub>/NiAl(110), image recorded with AFM tapping mode 1x1 $\mu$ m

Note in Figure 4.18 that large protrusions are observed. This might be due to some dealloying at the surface of underlying NiAl or Ni cluster agglomeration underneath the Al<sub>2</sub>O<sub>3</sub> known from the literature which might be particularly pronounced at this preparation.

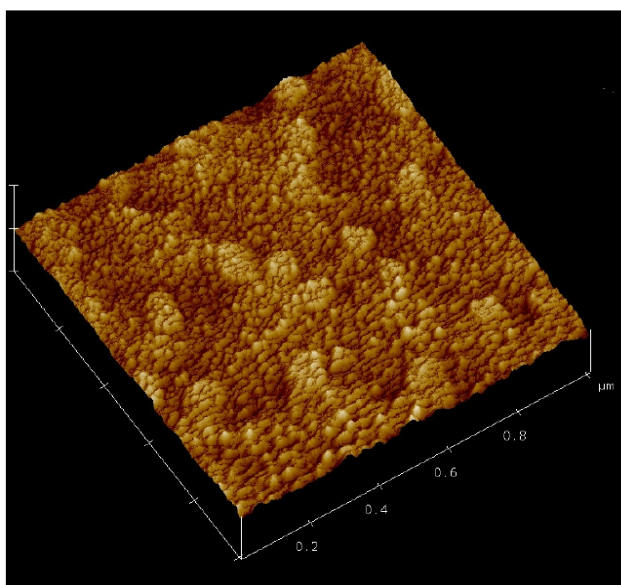


Figure 4.19: 3 dimensional view of 1ÅPt deposited at 100K/Al<sub>2</sub>O<sub>3</sub>/NiAl(110), image recorded with AFM tapping mode 1x1μm

Figure 4.18 and Figure 4.19 show the top view and three dimensional view of an AFM image in tapping mode of 1ÅPt deposited at 100K on Al<sub>2</sub>O<sub>3</sub>/NiAl(110). It is visible that the surface is amorphous.

Deposition thickness(Å)	Temperature	Radius (nm)	Height (nm)	Comments
2	300K	66.4	2.79	180 Island/μm <sup>2</sup> =1.8*10 <sup>10</sup> Island/cm <sup>2</sup>
2	100K			amorphous
1	300K	32	1.3	240 Island/μm <sup>2</sup> =2.4*10 <sup>10</sup> Island/cm <sup>2</sup>
1	100K			amorphous

Table 1: Average island sizes for different preparations

Actually the size of the Pt islands are very big compared with the work of Klimenkov *et al.* (2003). This may be attributed to a convolution effect of the tip of the AFM. The height of the islands could not be compared to Klimenkov results to get the mean cluster size because of the AFM tip convolution though height measurement with AFM can be done more accurately. It has to scale nearly linearly with the Pt amount deposited similar to Klimenkov's results. Also the island density decreases similar to Klimenkov's results though not in the same amount.



#### 4.6 STM scan for 1Å Pt deposited at 300K/Al<sub>2</sub>O<sub>3</sub>

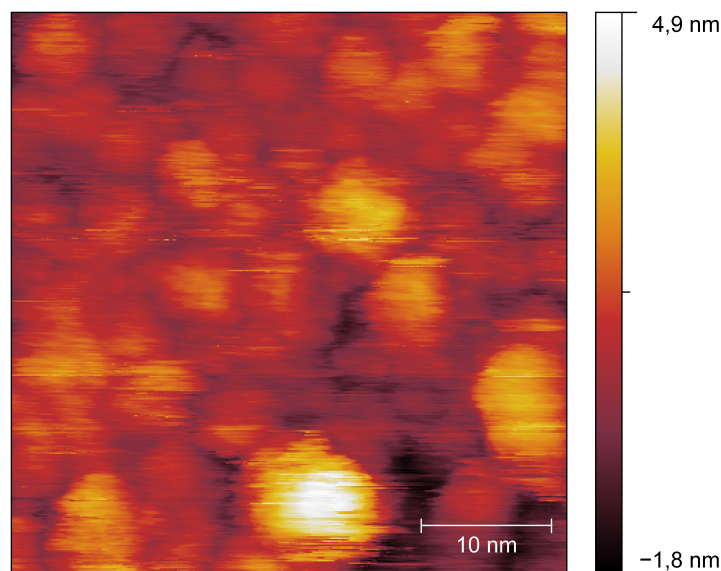


Figure 4.20: Top view of STM scan of 1ÅPt deposited at 300K/Al<sub>2</sub>O<sub>3</sub>/NiAl(110)

1Å platinum has been deposited at 300K on Al<sub>2</sub>O<sub>3</sub> and the sample has been scanned by STM under UHV conditions in the same chamber. Figure 4.20 and Figure 4.21 show the top view and the three dimensional view of the STM scan. The measured particle density was  $9.07 \cdot 10^{10}$  Island/cm<sup>2</sup> and the average particles height= 1.1145 nm and average particle size= 6.1375 nm. The average particles height are very close to Klimenkov measurements and own AFM data. While the average particle density is one order less than Klimenkov results, the average particle sizes are larger from Klimenkov measurement and the expected reason is the tip convolution which is not a problem in Klimenkov's TEM measurements.

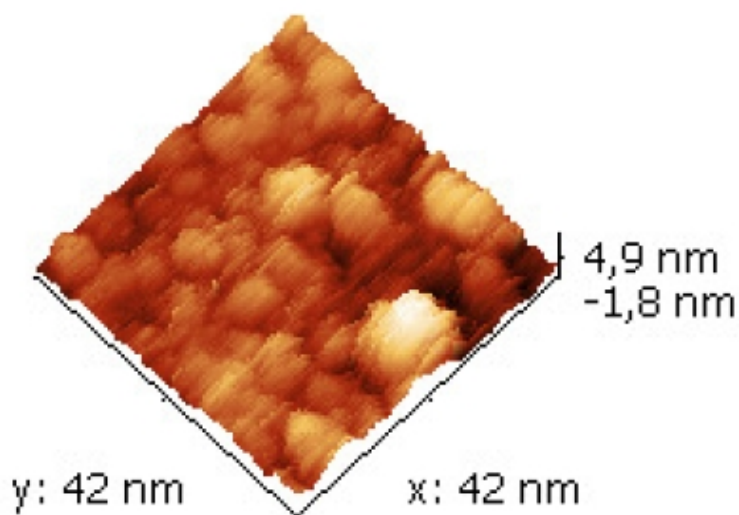


Figure 4.21: Three dimensional view of STM scan of 1ÅPt deposited at 300K/Al<sub>2</sub>O<sub>3</sub>/NiAl(110)

## 4.7 Discussion

Klimenkov *et al.* (2003) found for the deposition of Pt on Al<sub>2</sub>O<sub>3</sub>/NiAl(110) that the average cluster size increases monotonically with increasing coverage while the cluster density exhibits a maximum for a coverage at 0.5 of a monolayer equal to 1.13Å (nominal thickness according to micro balance calibration). Three dimensional growth is observed with the mean cluster height scaling also linearly with the cluster size. For a deposition of 0.5 of a monolayer they found a cluster density of  $9.8 \times 10^{12} \text{ cm}^{-2}$  with an average cluster height of 0.7 nm and an average cluster size of 1.39 nm for a surface temperature of 300 K during deposition. I have verified the growth by means of ex situ atomic force microscopy. In my experiments I found larger particles than reported by Klimenkov by at least a factor of 10 as obtained from the analysis of the AFM measurements. The differences between the literature experiments and my results were attributed to the limitations by the experimental setup, i.e. the dimension of the tip restriction from the AFM.



The STM measurement reported a  $9.07 \cdot 10^{10}$  Island/cm<sup>2</sup> cluster density and 1.1145 nm the average particles height the latter being close to Klimenkov *et al* (2003) measurements. The same STM tip convolution problem appears and the average apparent particles diameter is 6.1375 nm. I conclude that my preparations are not far away from Klimenkov results.

The discrepancy in the island density may also be related to tip convolution effects. Smaller islands might not be detected between close particles. So these measurements are only a lower limit. When comparing my AFM and STM data one may note that STM data exhibit a factor of 5 times higher densities under very comparable conditions. The tip convolution effect is much more pronounced in AFM measurements than in STM. It is also very well known that only at rather low coverages STM data give a good picture.

Another limitation is the quartz micro balance for which the minimum detectable amount of the deposited thickness of metals is 0.1 nm. The growth of the metal particles is reported to be inhomogeneous. Therefore it can be excluded that the discrepancy is being due to a slower deposition rate (by a factor of 10-20 times with a deposition rate of about 0.3-0.4 nm h<sup>-1</sup> at a crystal temperature of T=300 K) compared to the one reported by Klimenkov *et al*. In homogeneous growth such a change in deposition rate may result in larger particles. In view of this discrepancy to the literature the overall amount of the deposited Platinum will be used instead of the average particle sizes in the next chapters. Because I assumed that my measurements are limited by the resolution of the experimental setup I shall refer to Klimenkov's work in case island sizes are relevant for the discussion. The estimated error is within a factor of two when relating the height to cluster diameters for a certain deposition. As will be shown from FT-IRRAS measurements in Chapter 5 the sample preparation is very reproducible for repeated measurements. So one may discuss the changes in laser as a function of cluster size as changes with high reproducibility.

## 5 Adsorption and desorption of CO from Platinum surfaces

Understanding the mechanism of the adsorption of CO on the Platinum nanoparticles is essential to be known in this work. The bonding of the CO on the Platinum depends on the local electronic structure of the Platinum. So different particle sizes and shapes may influence the adsorption. This chapter contains two parts: the first is the adsorption and desorption of CO from Platinum single crystals. It summarizes different cases of flat and stepped Platinum single crystals from different literatures (Heyden & Bradshaw *et al.* 1983, Hayden *et al.* 1985, McClellan *et al.* 1981, Xu & Yates 1995). The second part summarizes the CO adsorption and desorption on Platinum nanoparticles deposited on the alumina. It shows the influence of the amount of Platinum deposited to the vibrational energy of the adsorbed CO.

### 5.1 Adsorption and desorption of CO from Platinum single crystals

Carbon monoxide exhibits a preference for linear adsorption sites at Platinum. However,  $\sigma$ - and  $\pi$ -bonding of CO at defects and other low-coordination sites on platinum give rise to lower C-O stretching frequencies than those at terrace sites. At low coverages first defect sites are populated resulting in absorption bands of relatively low frequency in FT-IR spectra followed by adsorption at terrace sites exhibiting a band approximately shifted by 20  $\text{cm}^{-1}$  to higher frequency. Dipolar interactions transfer intensity from the defect related band to the terrace one, so the absorption peak moves to higher frequency with increasing coverages. This has led to two types of errors in the assignments within the spectra. Firstly, on both supported catalysts and extended substrates, this shift in frequency has been interpreted as a dipolar effect acting on single adsorbed species. Secondly, the relatively small size of the metal particles in supported platinum catalysts results in a high population of edges and defects: intensity transfer may however prevent the observation of bands assigned to edge sites because of dipole-dipole interaction. In order to prevent such errors further experimental methods beside FT-IR have to be considered. TPD can give additional, valuable information on the presence of defect and edge sites. Therefore methods such as FT-IR, LEED and TPD will be discussed in the following.

### 5.1.1 Pt(111)

CO was adsorbed on Pt(111) at 150 K. Figure 5.1 shows TPD spectra as a function of CO adsorption coverage which agree to work at  $\theta < 0.5$  (Ertl *et al.* 1977, Norton *et al.* 1979). A shoulder at the high temperature side was assigned to adsorption at step sites of the surface by Collins & Spicer (1977). No effect on the shoulder intensity in Figure 5.1 was found by changing of cleaning procedure of the crystal or reorientation of the crystal.

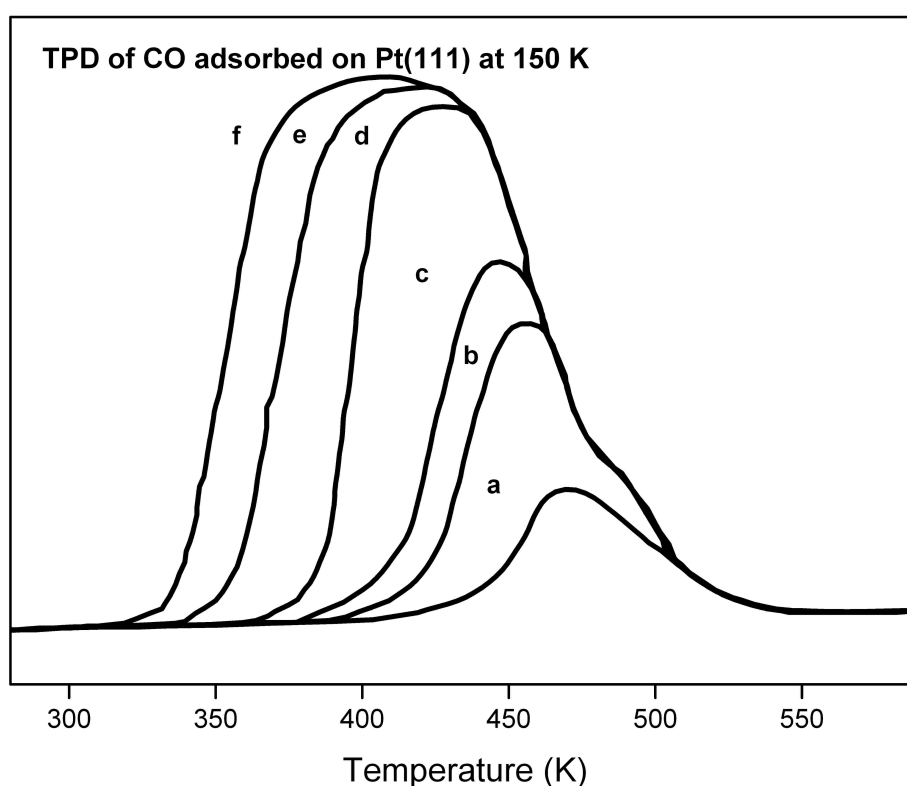


Figure 5.1: TPD spectra for various coverages of CO adsorbed on Pt(111) at 150 K. The coverages  $\theta$  are (a) 0.10, (b) 0.17, (c) 0.25, (d) 0.40, (e) 0.50, (f) 0.62. (Heyden & Bradshaw 1983)

At the same adsorption temperature LEED patterns were visible as reported by Ertl *et al.* (1977). After getting the  $(\sqrt{3} \times \sqrt{3})R30^\circ$  overlayer observed with LEED  $c(4 \times 2)$  start to appear which is related to CO island formation before the coverage of 0.5 is reached (Ertl *et al.* 1977). Using integrated TPD intensities the saturation coverage at low adsorption temperature was estimated to be  $\theta = 0.64$ .

Figure 5.2 shows IRAS spectra of CO adsorbed at 150 K exhibiting three vibrational modes

recorded by Heyden *et al.* (1983). The first peak in the regime ( $2094\text{--}2110\text{ cm}^{-1}$ ) is typical for on-top bonding CO. At low CO adsorption coverage the on-top peak has a shoulder at the lower frequency side. The peak shifts up as the CO adsorption coverage increases ( $2140\text{ cm}^{-1}$ ) which agrees with earlier work of Shigeishi & King (1976) and Crossley & King (1977). Two further vibrational modes were found in the bridging region at  $1840\text{--}1857\text{ cm}^{-1}$  and at  $1810\text{ cm}^{-1}$ . Those peaks were neither observed using EELS measurements (Froitzheim *et al.* 1977, Hopster & Ibach 1978, Baro & Ibach 1979, Avery 1981) nor in some IRAS experiments (Shigeishi & King 1976, Bradshaw & Hoffmann 1976) or it was observed as one peak (Krebs & Lüth 1977). To detect a vibrational mode in  $1800\text{ cm}^{-1}$  is not easy because minor amounts of coadsorbed water from residual gas may cause the disappearance of this adsorption site.

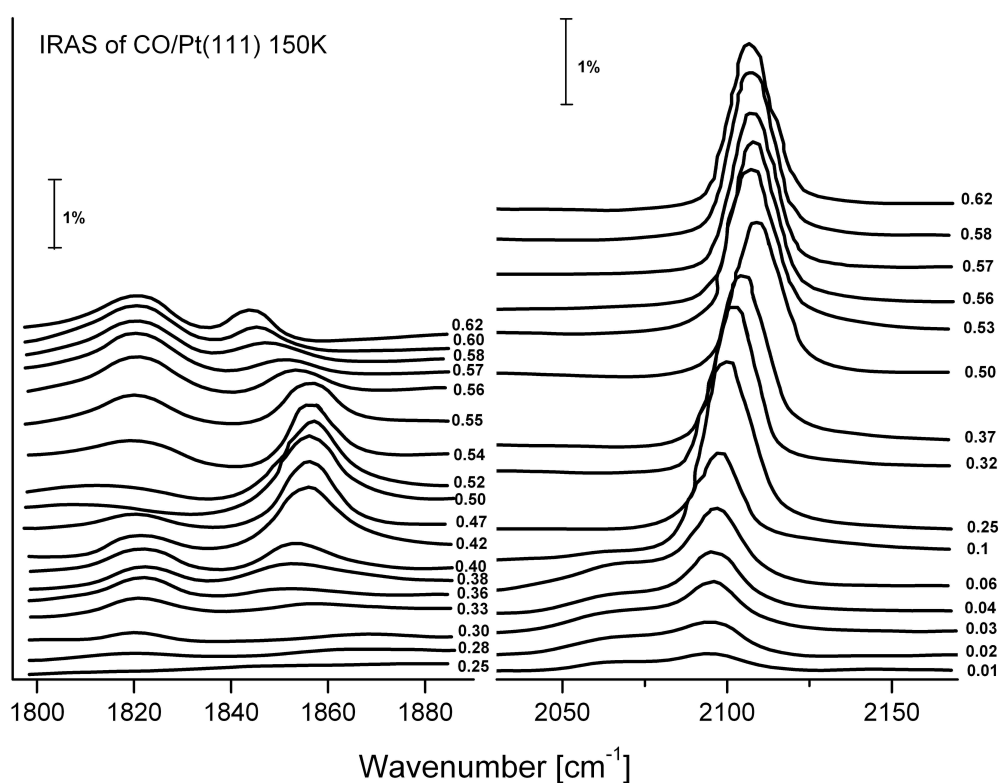


Figure 5.2: IR spectra of the linear and bridging C-O stretch regions for CO adsorbed on Pt(111) at 150 K. The coverage  $\theta$  is calculated from TPD data (Heyden & Bradshaw 1983)

The integrated intensity of the on-top and bridge bond CO as a function of adsorption coverage is shown in Figure 5.3. The related frequency shifts are shown in Figure 5.4.

On-top CO has a maximum integrated intensity at  $\theta = 0.33$  where the LEED pattern is  $(\sqrt{3} \times \sqrt{3})R30^\circ$  and a minimum at  $\theta = 0.5$  where the LEED pattern is  $c(4 \times 2)$ . The natural width of the on-top peak decreases by  $10 \text{ cm}^{-1}$  as the coverage has increased above  $\theta = 0.3$ .

The change in the frequency of the bridge bound CO is strongly dependent on the adsorption coverage. It shifts up from  $1845 \text{ cm}^{-1}$  at  $\theta \sim 0.4$  to the maximum at  $1857 \text{ cm}^{-1}$  where the LEED pattern is  $c(4 \times 2)$  at  $\theta = 0.5$ . Then the peak shifts down to  $\sim 1840 \text{ cm}^{-1}$  at  $\theta = 0.64$ . These results of increasing of the intensity of the bridge bond CO is in good agreement with the EELS results (Hopster & Ibach 1978, Baro & Ibach 1979). It supports the model that only on-top CO are found in  $(\sqrt{3} \times \sqrt{3})R30^\circ$  as shown in Figure 5.5.

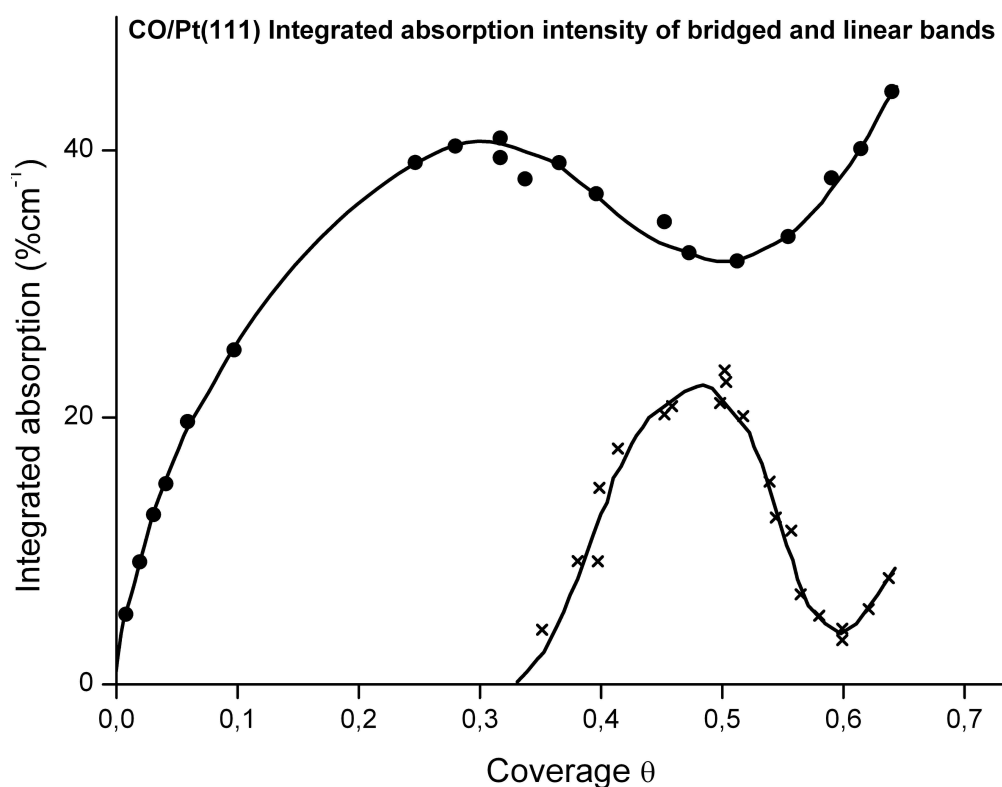


Figure 5.3: The integrated absorption intensity of the bridging (x) and linear (O) C-O stretching vibrational bands as a function of coverage for adsorption at 95 K (Heyden & Bradshaw 1983)

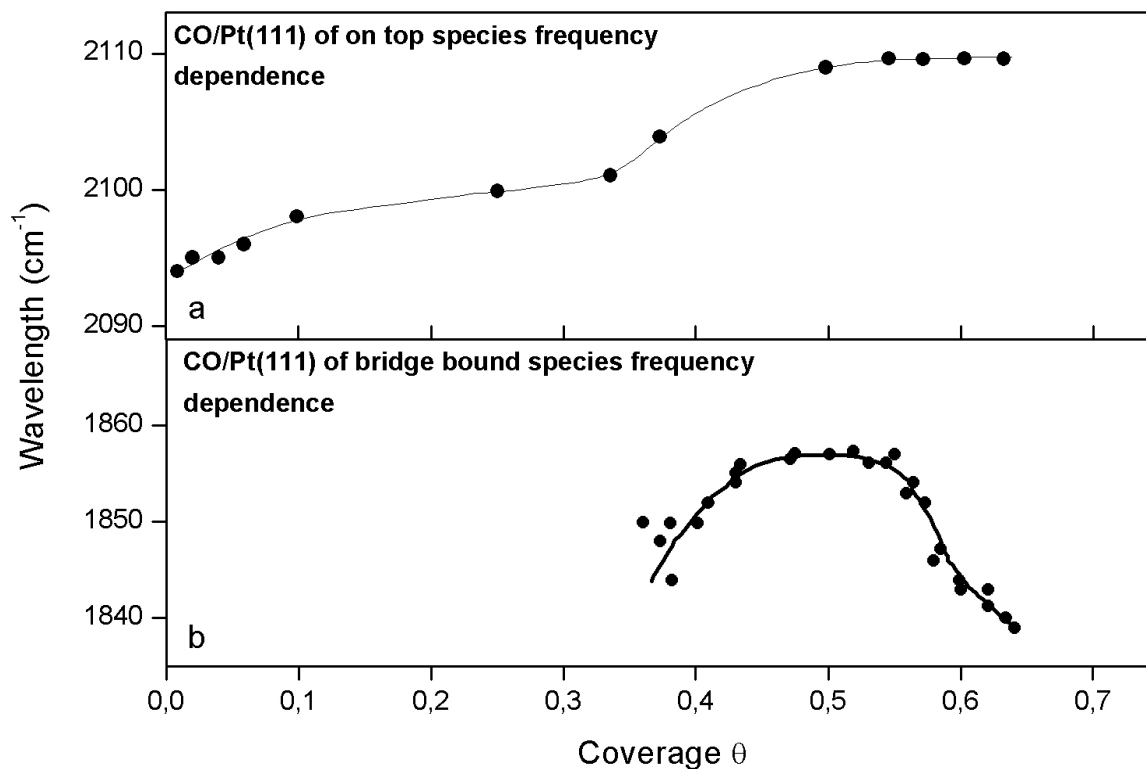


Figure 5.4: The frequency of the linear (a) and bridging (b) C-O stretch bands as a function of coverage for adsorption at 95 K (Heyden & Bradshaw 1983)

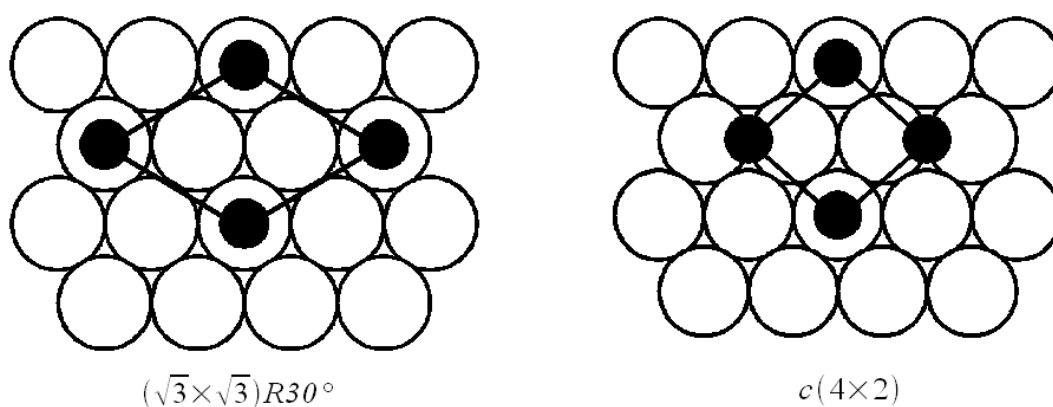


Figure 5.5: Real space models for  $(\sqrt{3} \times \sqrt{3})R30^\circ$  and  $c(4 \times 2)$  structures (Heyden & Bradshaw 1983)

### 5.1.2 Pt(533)

After viewing CO adsorption and desorption on Pt(111), it is necessary to study stepped Pt single crystals. The CO adsorption/desorption on Pt(533) has been studied using infrared reflection-absorption spectroscopy (IRAS), LEED and TPD by Hayden *et al.*(1985). The purpose of this study was to get a clear idea about CO interaction on the step edges likely to be found at Platinum nanoparticles. The Pt-s[4(111)×(100)] surface, which is also described as the (533) surface is shown in Figure 5.6. The (111) terrace area on this stepped crystal could be compared to the results of Pt(111) (Heyden & Bradshaw 1983).

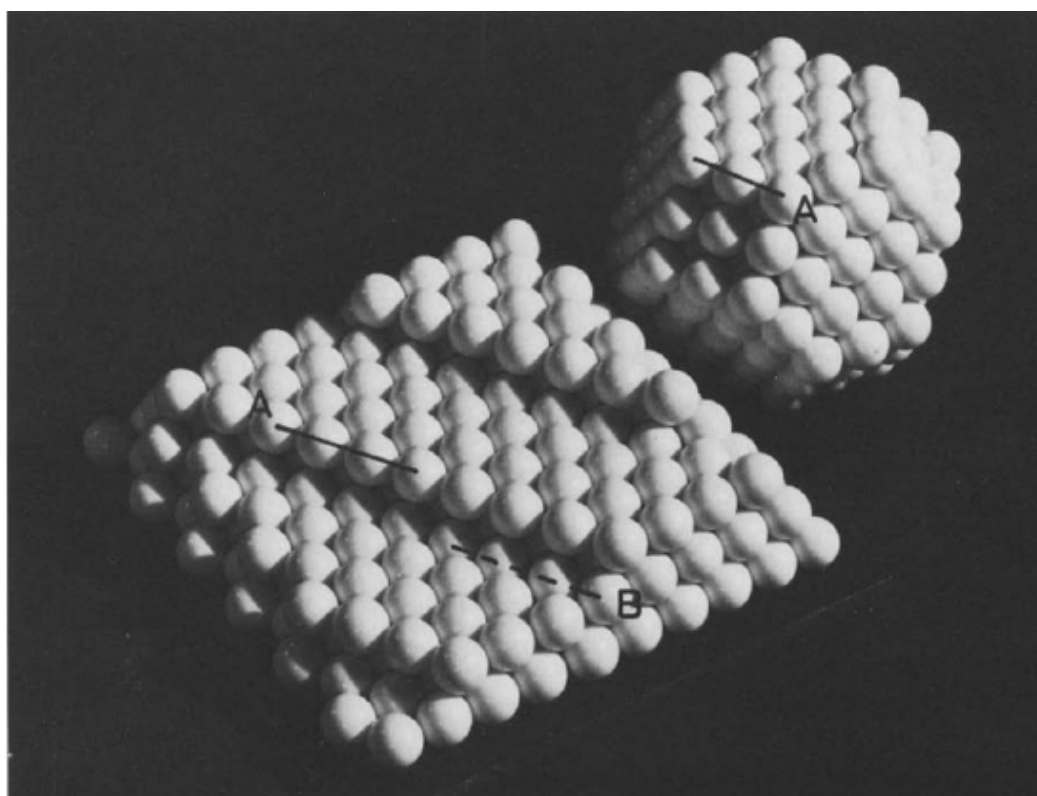


Figure 5.6: Stepped Pt surface [4(111)×(100)], or (533), with step atoms A which simulate edge atoms in the truncated octahedron (also marked A) (Hayden *et al.* 1985).

Figure 5.7 shows TPD spectra of CO adsorbed at 85 K on Pt(533). At low coverages a single peak appears at 550 K. This peak is continuing to grow in intensity and reaches its maximum intensity at  $0.3 \theta_{\max}$ . At the same coverage a low temperature peak starts to appear. As the CO coverage was increased the high temperature peak is still constant while the low temperature peak was shifting down. The TPD spectra of CO desorbed from Pt(111)(Ertl *et al.* 1977, Steininger *et al.* 1982) were compared to the actual results. The high temperature desorption peak is assigned to desorbing CO from step edges. This conclusion agrees with the conclusions of Collins & Spicer (1977) and Hopster & Ibach (1978).

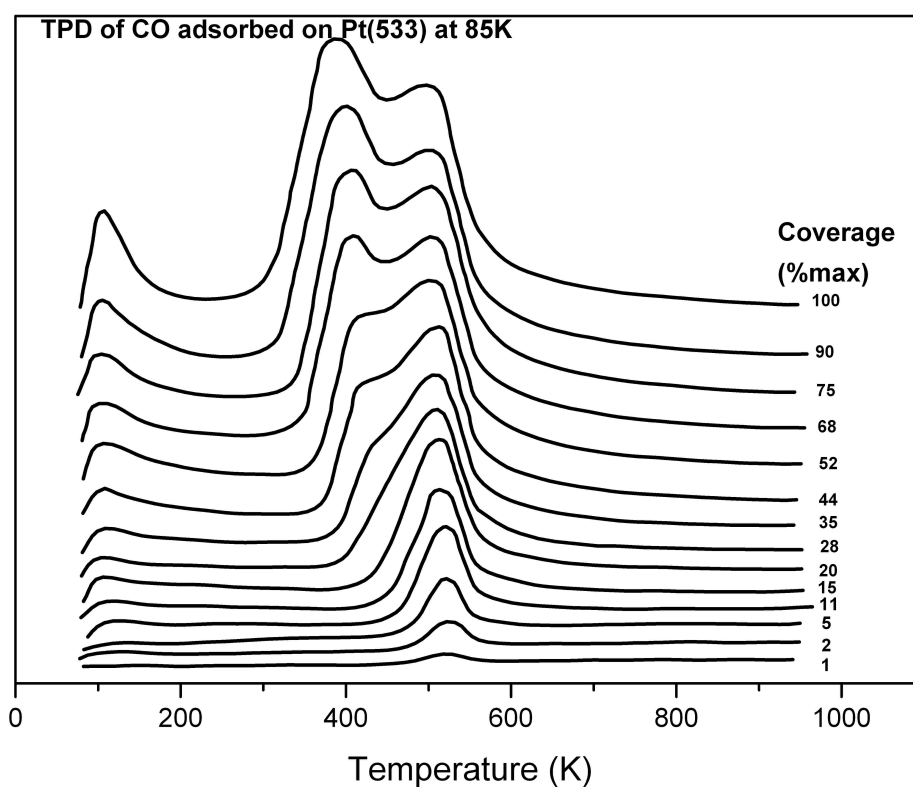


Figure 5.7: Thermal desorption spectra for CO/Pt(533) after adsorption at 85 K (Hayden *et al.* 1985).



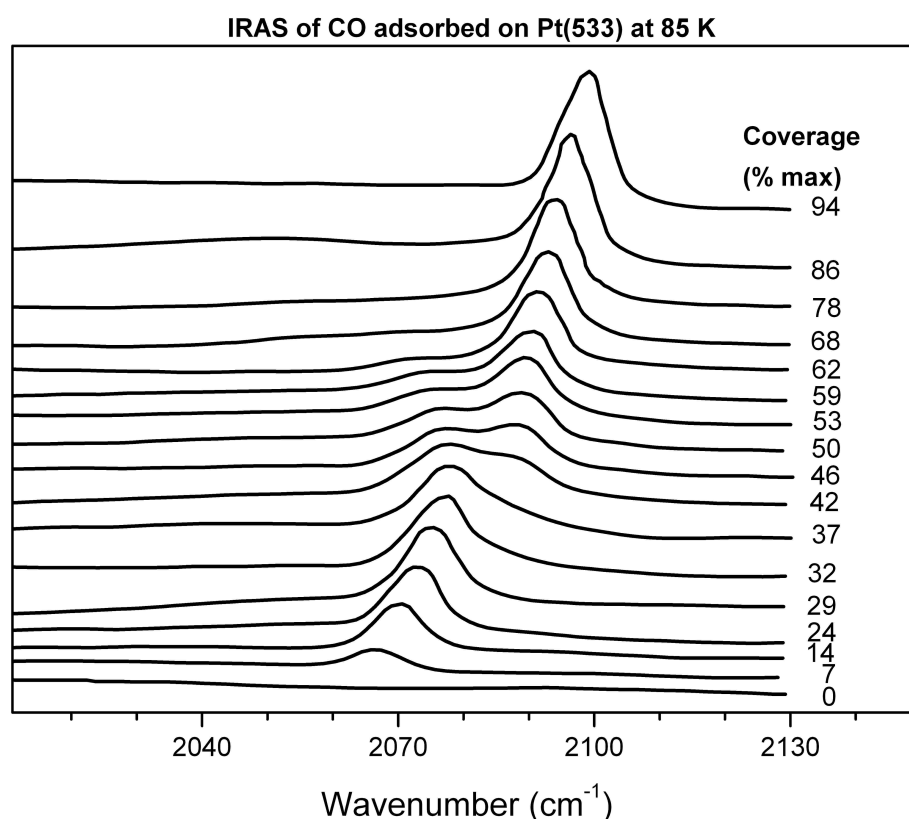


Figure 5.8: Infrared reflection-absorption spectra in the C-O stretch region from the system CO/Pt(533) as a function of increasing relative coverage (Hayden *et al.* 1985)

Figure 5.8 shows IRA spectra of CO adsorbed on a Pt(533) single crystal at 85 K presented by Hayden *et al.* (1985). It is clear that there is no vibrational mode less than  $2000 \text{ cm}^{-1}$ . That means there is no CO adsorbed in bridge bonded sites. The found vibrational bands were observed in the range of  $2060\text{--}2100 \text{ cm}^{-1}$ . The IRA spectra of the adsorbed CO show that first the peak appears at  $2067 \text{ cm}^{-1}$  with its intensity growing as a function of CO adsorption coverage to  $2076 \text{ cm}^{-1}$  up to  $\sim 0.30 \theta_{\text{max}}$ . Another peak appears at  $2086 \text{ cm}^{-1}$  and grows as the CO adsorption coverage further increases. As soon as this peak intensity increases the first peak intensity vanishes. So it was identified that two distinct CO species are present and the frequencies of those peaks are similar to the CO on-top species on Pt(111) (Hopster & Ibach 1978, Steininger *et al.* 1982, Heyden & Bradshaw 1983, Shigeishi & King 1976).

The growth of the first peak in the range of ( $2065\text{--}2078 \text{ cm}^{-1}$ ) is synchronized to the growth of the high temperature TPD peak as shown in Figure 5.7. This band was characteristic to adsorbed CO at on-top bonding sites on the step edges. The same is the case for the second peak that appears at CO adsorption coverages more than  $\theta > 0.30 \theta_{\text{max}}$  within a frequency range of  $2086\text{--}2097 \text{ cm}^{-1}$ . It was

characteristic to the adsorbed CO on the (111) terraces. The appearance of the high desorption temperature at low CO adsorption coverage means that the adsorption happens sequentially because re-arrangements may happen in the non-equilibrated CO layer through heating up the sample.

The low frequency peak in the IR was assigned to CO adsorbed on step edges by implementing partial desorption experiments.

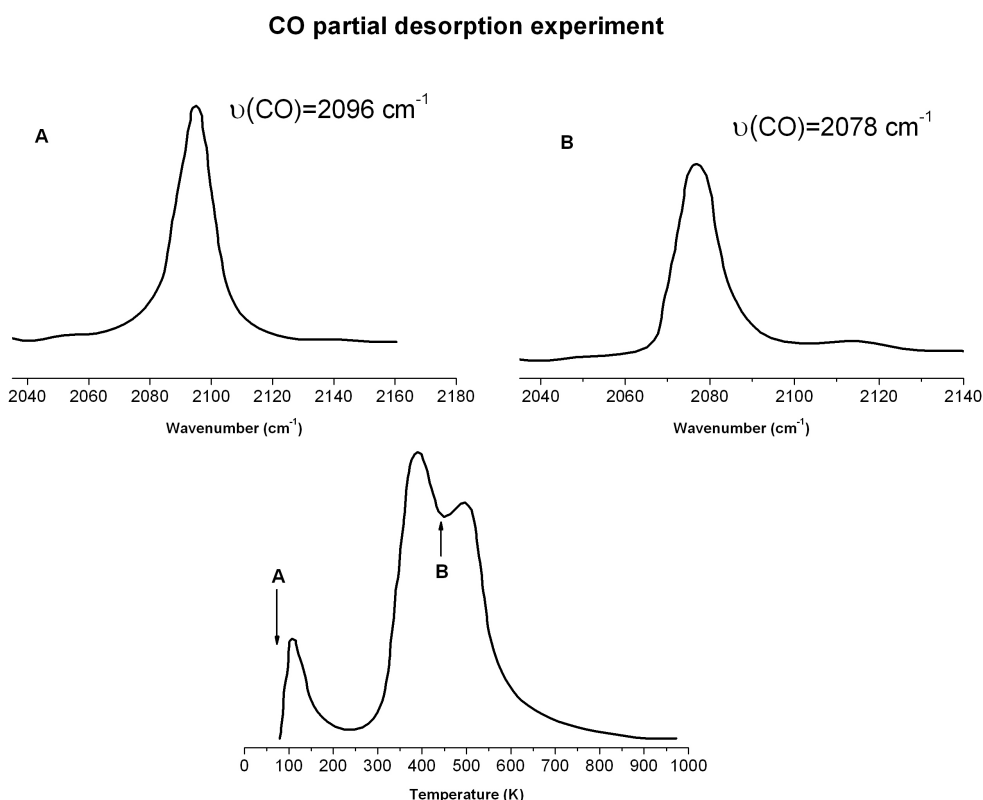


Figure 5.9: The partial desorption experiment of CO/Pt(533): the saturated overlayer at 90 K gives the IR spectrum A. Stopping the TPD flash at the point B between the two peaks gives rise to the IR spectrum B (Hayden *et al.* 1985).

Figure 5.9 A is the IRA spectrum of a saturation coverage of CO from Hayden *et al.* (1985). TPD experiments were implemented and stopped at point B. IRA spectrum B shows that the peak was shifted down to  $2078 \text{ cm}^{-1}$ , which is the same vibrational frequency as the Pt(533) exposed to a coverage of  $\sim 0.30 \theta_{\text{max}}$ . Continuing the TPD, the results show only the high temperature peak. Then Hayden *et al.* (1985) concluded that no bridging bond of CO adsorbed on the stepped edges occur while at the coverages  $\theta > 0.3$  on Pt(111) both linear and bridge CO were visible (Heyden & Bradshaw 1983).

### 5.1.3 Pt(321)

The stepped crystals give a clear view about different interaction of CO with edges and terraces. Pt(321) single crystal is a stepped crystal which has an extremely rough surface because of  $n=40\%$  of the surface atoms are coordinately unsaturated as shown in Figure 5.10 (McClellan *et al.* 1981). Using this crystal Pt [3(111) $\times$ (311)] will allow to investigate the effect of local surface morphology on adsorbates (Iwasawa *et al.* 1976).

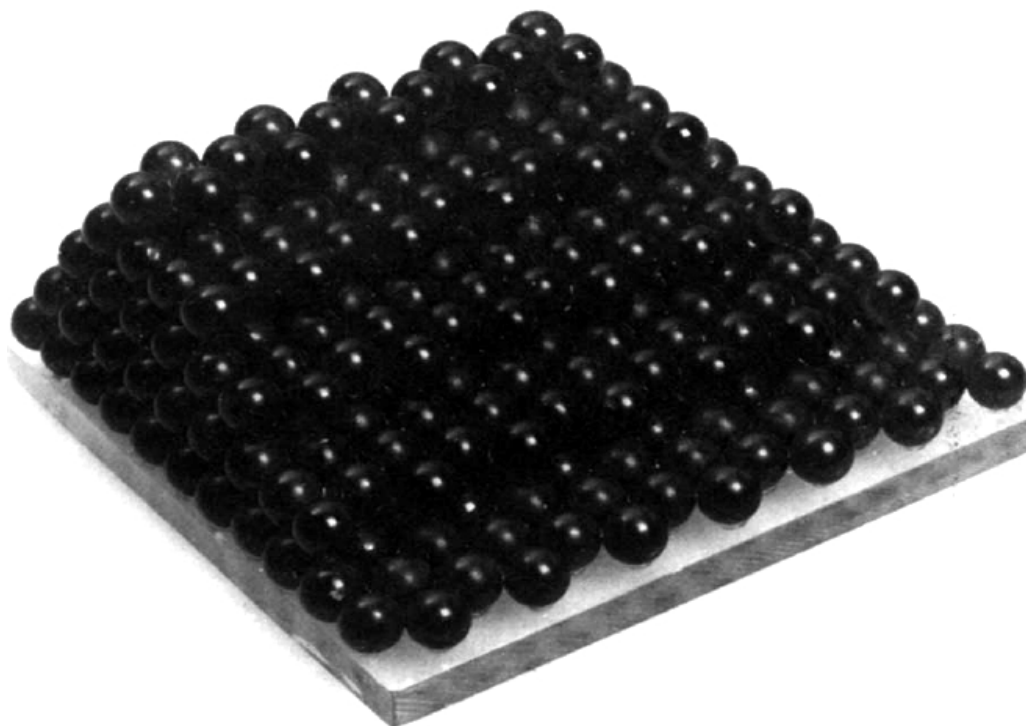


Figure 5.10: Photograph of a ball model of the Pt(321) surface. (McClellan *et al.* 1981)

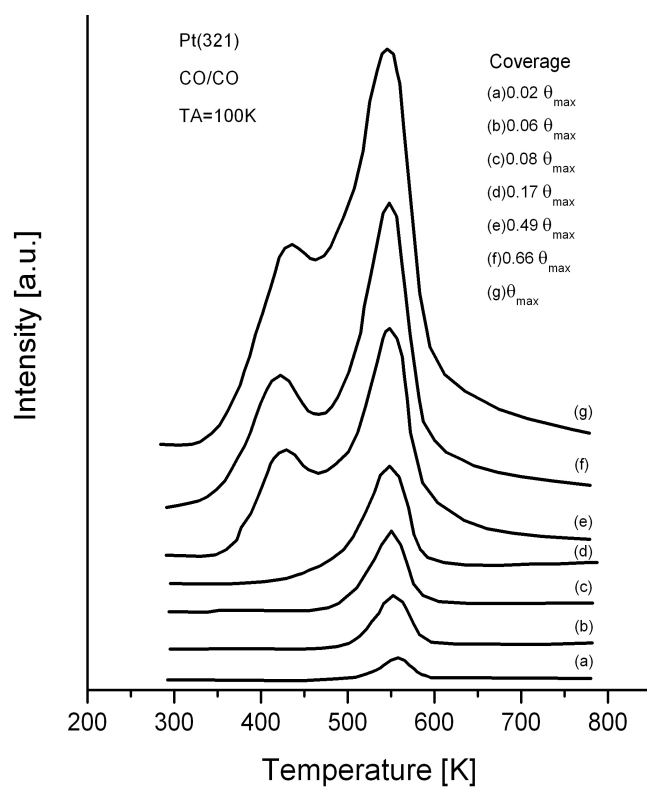


Figure 5.11: A series of carbon monoxide desorption spectra for various CO coverages on the Pt(321) surface at 100K. The heating rate was 10 K/s. (McClellan *et al.* 1981)

Figure 5.11 shows TPD as a function of CO adsorption coverage for a Pt(321) surface. A single peak was observed at 556 K for low CO coverages (McClellan *et al.* 1981). This peak grows and shifts down to 546 K as the coverage increases as shown in Figure 5.11 a-d. A low temperature desorption peak starts to appear for coverages above  $0.2\theta_{\max}$ . Let us compare this desorption peak at 436 K to the results and analogy of Pt(111) (Hopster & Ibach 1978, Collins & Spicer 1977). It was concluded that this desorption peak is from desorption of CO from (111) terraces. The higher desorption peak ( $>500$  K), is a well known desorption from the step edges (Hopster & Ibach 1978, Collins & Spicer 1977, McCabe & Schmidt 1977, Fair & Madix 1980). Then it was classified that the higher temperature peak can be assigned to the CO desorption from step sites of the crystal.

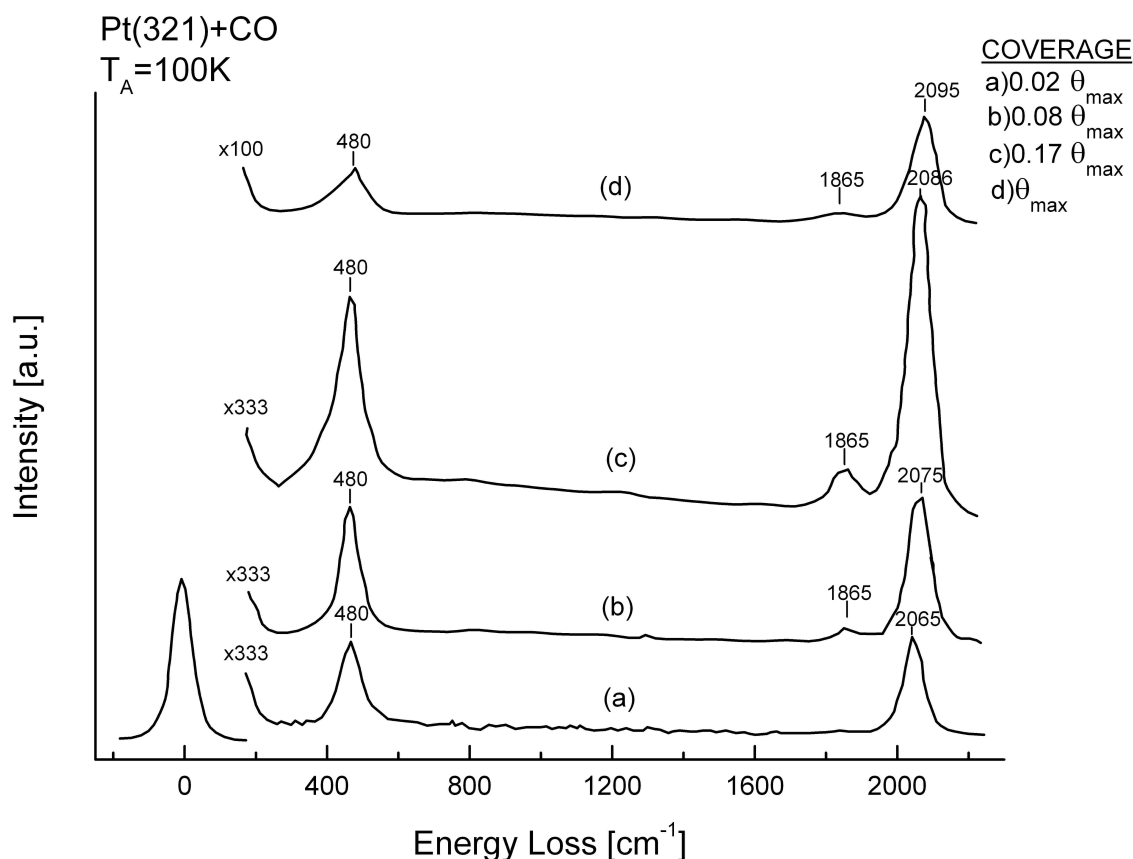


Figure 5.12: A series of high resolution electron energy loss spectra for carbon monoxide adsorbed on the Pt(321) surface at 100K. The beam energy was  $\sim 5 \text{ eV}$  (McClellan *et al.* 1981)

Figure 5.12 shows spectra of high resolution electron energy loss spectra (HREELS) as a function of CO adsorption coverage on Pt(321) surface. At low CO coverage, two peaks were visible at  $480 \text{ cm}^{-1}$  and  $2065 \text{ cm}^{-1}$ . The two peaks were assigned to CO on-top bonding on the platinum surface. The  $480 \text{ cm}^{-1}$  vibrational peak was assigned to adsorption at kink sites (Hopster *et al.* 1978) which was never reported elsewhere. A new peak at  $1865 \text{ cm}^{-1}$  appears as the CO adsorption coverage increases. This new peak is assigned to bridge bonded CO on Platinum. As soon as the CO coverage further increases, the band shifts from  $2065 \text{ cm}^{-1}$  to  $2095 \text{ cm}^{-1}$ . This up shift is due to dipole-dipole coupling and this phenomena has been observed in CO adsorption on Pt(111) surface (Shigeishi & King 1976). To prove that these two peaks are caused from two different desorption sites partial desorption experiments were done by McClellan *et al.* (1981).

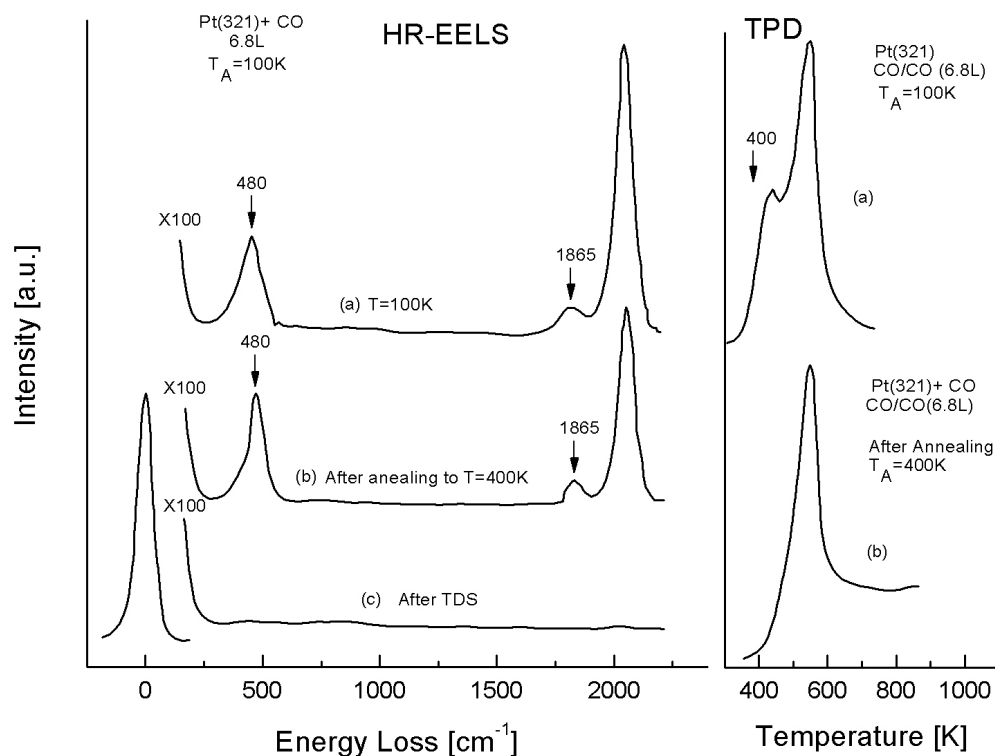


Figure 5.13: Left side: A series of high resolution electron energy loss spectra taken after carbon monoxide is (a) adsorbed at 100K, (b) desorbed from the terraces, and (c) desorbed from Pt(321) surface. Right side: (a) TPD of 6.8L CO (b) TPD of 6.8L CO after annealing to  $T_A=400\text{K}$  (McClellan et al. 1981)

As shown in Figure 5.13, the CO low temperature peaks were desorbed by heating the sample to 400 K. After cooling down, a subsequent TDS shows that just the high temperature desorption peak is visible indicating that no redistribution of CO occurs. That means the two peaks correspond to different chemisorption species which are sequentially desorbed. Therefore a relationship between the vibrational peaks that appear in Figure 5.11 and the two chemisorption peaks which appeared in the TDSs may be found. After annealing the sample to 400 K, HREEL spectra show the vibrational peaks at  $1865\text{ cm}^{-1}$  and  $2095\text{ cm}^{-1}$ . This means that the CO adsorbs on the step edges forming on-top and bridge bonds. Annealing the sample to 900 K, no peak of CO adsorbed is observable, indicative for a complete CO desorption from the Pt(321) single crystal. If the results of the HREEL spectrum of CO adsorbed on step edges are compared in details with saturation coverage results, some changes in the peak broadening are found. The saturation coverage peaks in both cases ( $2095\text{ cm}^{-1}$  and at  $480\text{ cm}^{-1}$ ) are broader. These results have been interpreted as there is just small difference for bounding of CO on step or terrace sites.

## 5.2 Pt(335) & Pt(112)

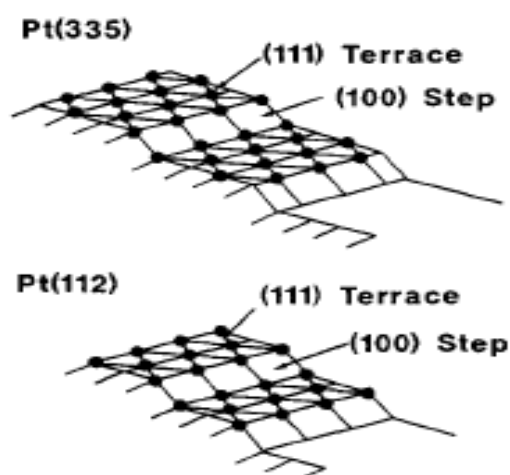


Figure 5.14: Schematic comparison of Pt(335) and Pt(112) single crystal surfaces. The terrace orientation is (111) while the step orientation is (100). (Xu & Yates 1995)

A schematic drawing of Pt(335) and Pt(112) is shown in Figure 5.14 (Xu & Yates 1995). Terrace sites orientated in the (111) direction separated by a single step of the (100) are exhibiting in both single crystals. The terrace width is different with Pt(112) having a width one atom less than Pt(335). The width of the 4 (111) terrace and a single step of (100) are the same for Pt(533) and Pt(335) but the difference is the orientation.

### 5.2.1 TPD measurements

The adsorption of CO on the stepped crystals Pt(335) (four-atom wide terraces) and Pt(112) (three atom wide terraces) has been studied by infrared reflection absorption spectroscopy (IRAS) and TPD by Xu & Yates (1995).

On Pt(335) CO adsorption and desorption has been studied using TPD as shown in Figure

5.15.  $\theta_{\text{CO}}^r$  is relative to the saturation coverage. The heating rate was 1.3 K/s. Two desorption features are visible with peaks at  $\sim 400$  K and  $\sim 500$  K. The  $\sim 500$  K desorption feature that appears at the low coverage is related to the CO desorption from the step sites. This feature does not appear for CO desorption from Pt(111) (McCabe & Schmidt 1977, Collins & Spicer 1977). At higher coverages low temperature desorption is visible which is related to the desorption from the terraces (Luo *et al.* 1992).

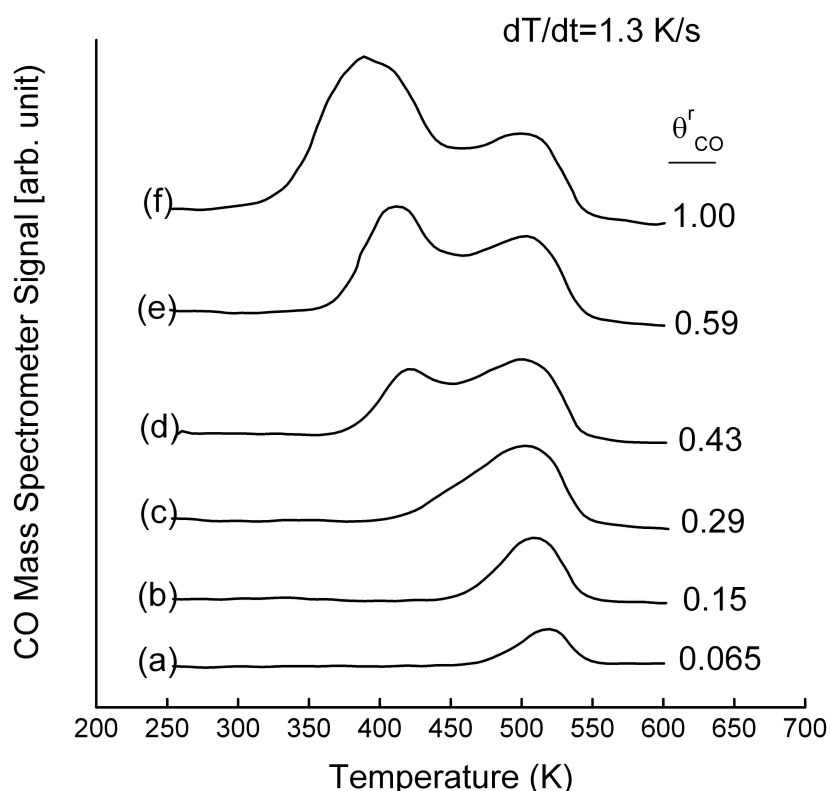


Figure 5.15: Temperature programmed desorption of CO on Pt(335). Heating rate was 1.3 K/s. CO was dosed at 90 K. The coverages,  $\theta_{\text{CO}}^r$ , were determined with respect to the saturation coverage. (Xu & Yates 1995)

The TPD spectra of CO desorption from Pt(112) is shown in Figure 5.16. The heating rate was 1.4 K/s and the coverages  $\theta_{\text{CO}}^r$  is given relative to the saturation coverage. Two desorption features are visible in Figure 5.16. The CO desorption features in Pt(335) and Pt(112) are similar in the subsequent coverages and the desorption temperature.

The CO saturation coverage shows that the ratio of the two peaks in both crystals are different. CO/Pt(112) exhibits a higher ratio of higher temperature desorbing feature which is consistent with the higher step density.



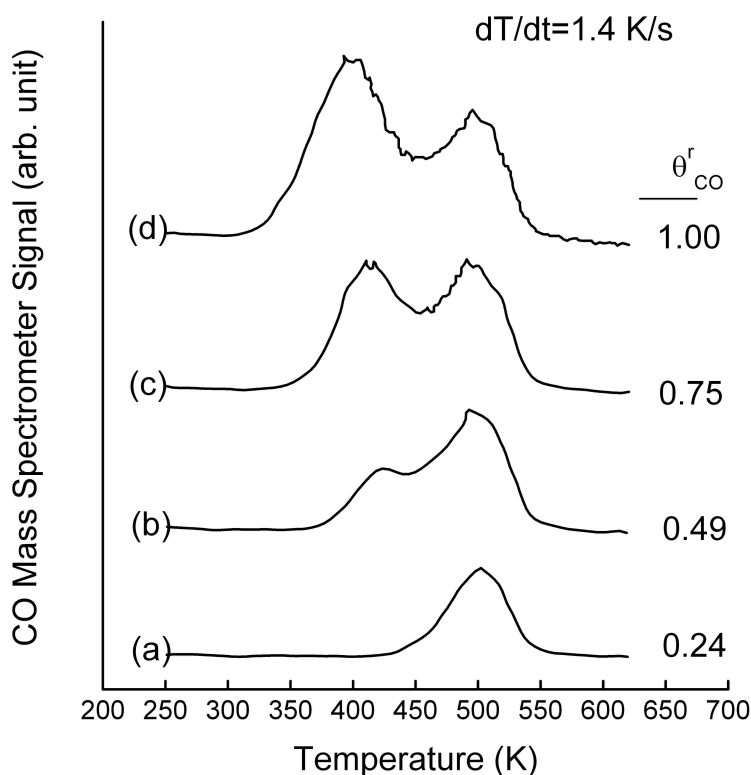


Figure 5.16: Temperature programmed desorption of CO on Pt(112). Heating rate was 1.4 K/s. CO was dosed at 90 K. The coverages were determined with respect to the saturation coverage. (Xu & Yates 1995)

The desorption kinetics of CO on Pt(335) and Pt(112) at 90 K are shown in Figure 5.17. For both crystals, the starting rate of the CO adsorption is constant up to  $\sim 70\%$  of the saturation and then the sticking probability decreases. Those results are in a good agreement with other studies on Pt(335), Pt(112) and Pt(321) by (Luo *et al.* 1992, Henderson *et al.* 1989, McClellan *et al.* 1981).

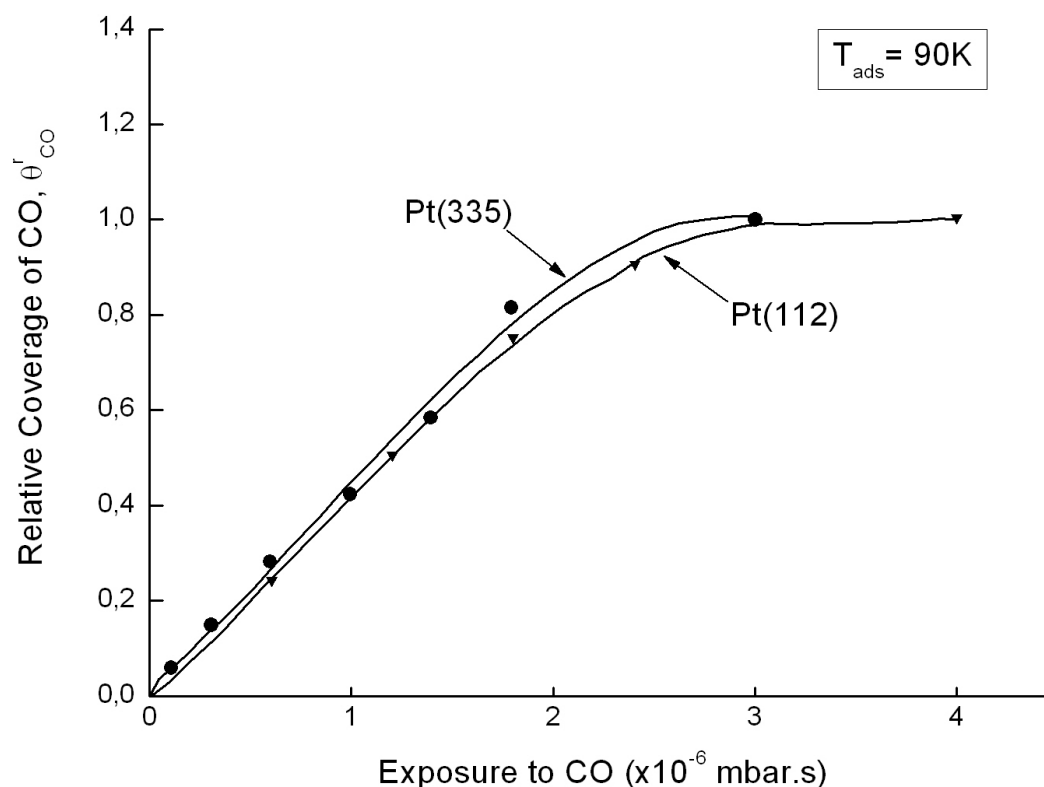


Figure 5.17: Comparison of CO adsorption kinetics on Pt(335) and Pt(112) single crystal surfaces. The adsorption temperature was 90 K. (Xu & Yates 1995)

## 5.2.2 FTIR measurement

The CO adsorption coverage on Pt(335) is shown in Figure 5.18 (Xu & Yates 1995). The spectra were averaged over 900 scans and recorded with  $4 \text{ cm}^{-1}$  resolution. The CO was adsorbed at 90K and then the surface was annealed to 290K. From different adsorption coverages in Figure 5.18 it is shown that four vibrational species are visible subsequently on the surface. At a low coverage Figure 5.18(a-b), shows a CO vibrational peak at  $\sim 2075 \text{ cm}^{-1}$  which is attributed to on-top species at step sites. As the coverages increase in Figure 5.18(c-d) a CO vibrational species is visible at  $\sim 1880 \text{ cm}^{-1}$  which is bridge CO on step sites. At higher CO coverages in Figure 5.18(e-f) it is shown that CO vibrational species is observed at  $\sim 2092 \text{ cm}^{-1}$ . At 0.6 ML, bridged CO start to appear at the terrace. This adsorption coverage is discussed in details in (Xu *et al.* 1994) and it agrees with other studies like (Luo *et al.* 1992, Henderson *et al.* 1990).

It was noted that as the coverages increase, the ratio of the high frequency to the low frequency mode is increasing for both on-top species and the bridged species. The high vibrational frequency is attributed to the on-top species adsorbed on edge and terrace sites vibrating in phase together. This is because of the well known intermolecular vibrational coupling effects (on-top CO on steps and on-top CO on terraces)(Hoffmann 1983).

FT-IRRA spectra of CO adsorption coverage on Pt(112) is shown in Figure 5.19. The IR spectra in Pt(112) was simpler than for Pt(335). The first vibrational species appeared at  $2068\text{ cm}^{-1}$  for low coverages. This frequency is not exactly the same as in Pt(335) but it is in the same region for low coverages. So we can say that this vibrational band is due to CO adsorbed on the step edge Pt(100). As the coverage of CO increased, there is no visible intermediate adsorption phenomena as in Pt(335). So the development of CO step and terrace adsorption bands was not resolved. The CO bridge adsorption has only a small intensity at  $1845\text{ cm}^{-1}$  for a CO saturation coverage shown in Figure 5.18 e-f. The occurrence of this low frequency band, and from comparison to the Pt(335) spectra with bridged CO on edges at  $1854\text{ cm}^{-1}$ , it was concluded that this low frequency band is bridged CO on edge sites of Pt(112).

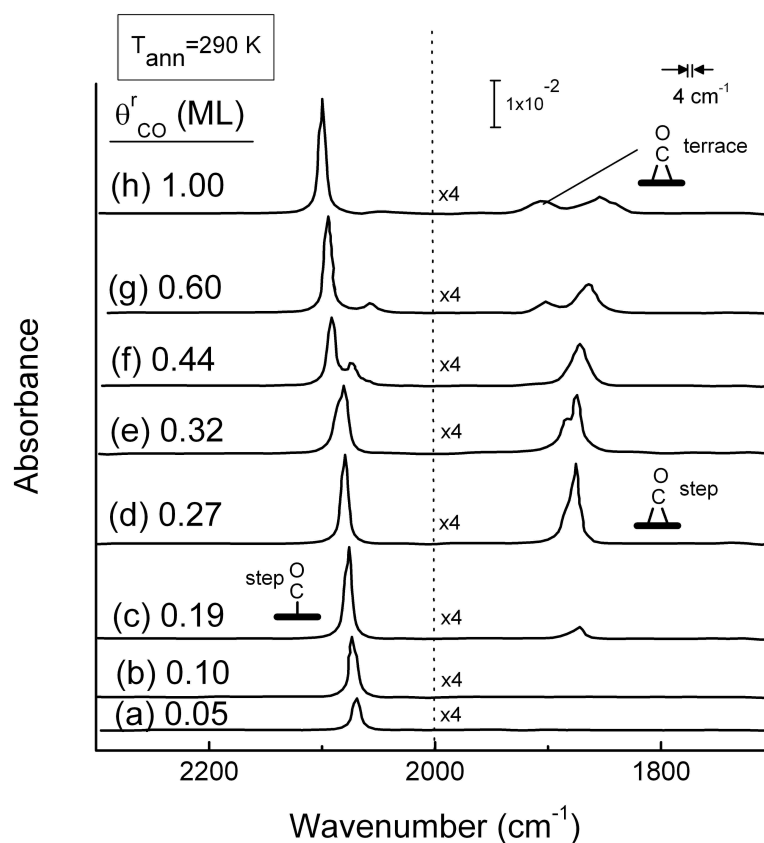


Figure 5.18: IRAS studies of CO stepwise adsorption as a function of coverage on Pt(335). The spectra were averaged over 900 scans at  $4 \text{ cm}^{-1}$  resolution. The spectra were taken at 90 K after annealing the adsorbate-covered surface to 290 K. (Xu & Yates 1995)

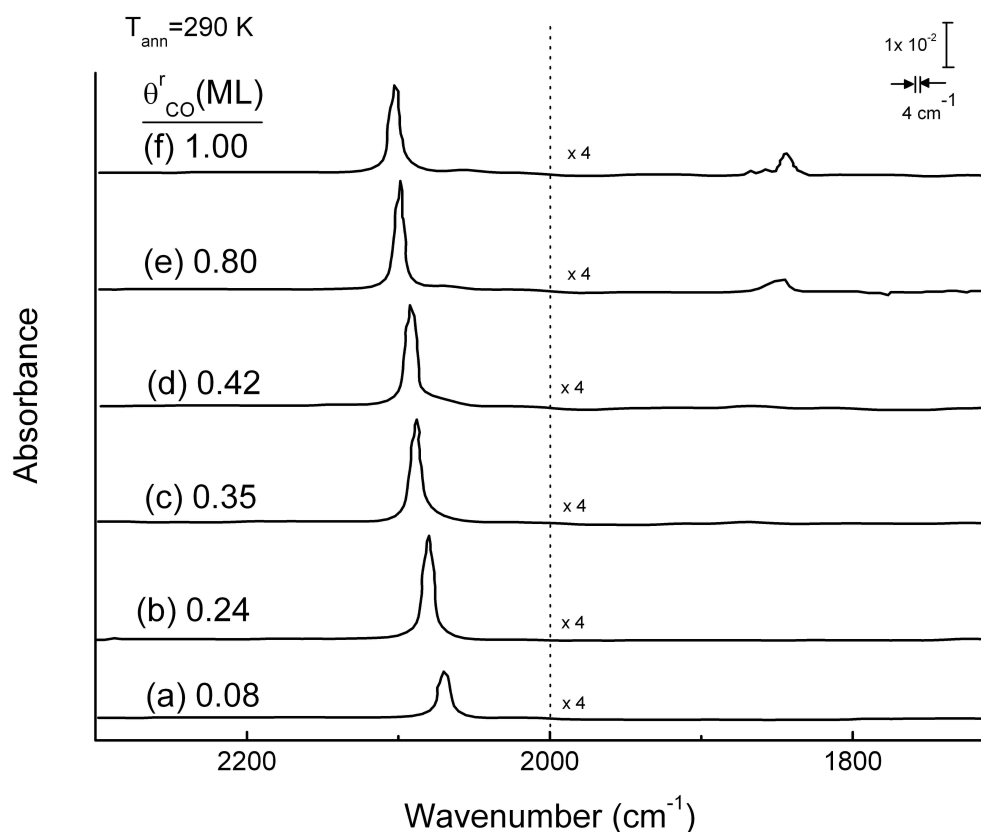


Figure 5.19: IRAS studies of CO adsorption as a function of coverage on Pt(112). The spectra were averaged over 900 scans at 4 cm resolution. The spectra were taken at 90 K after annealing the adsorbate-covered surface to 290 K. (Xu & Yates 1995)

### 5.3 Adsorption of CO on Pt Nanoparticles

In the following section own data on the CO adsorption at Pt nanoparticles at Al<sub>2</sub>O<sub>3</sub> will be presented and compared to the literature including HREELS and TPD data by Winkelmann *et al.* (1994) for Pt deposits on alumina at 300K.

Figure 5.20 shows FT-IRRA spectrum of a saturation coverage of 33L CO adsorbed on 3 Å of Pt (deposited on Al<sub>2</sub>O<sub>3</sub>/NiAl(110) at T= 300K) recorded at a crystal temperature of T=90K. Figure 5.20 shows that there are no 2-fold or 3-fold species, just on-top species.

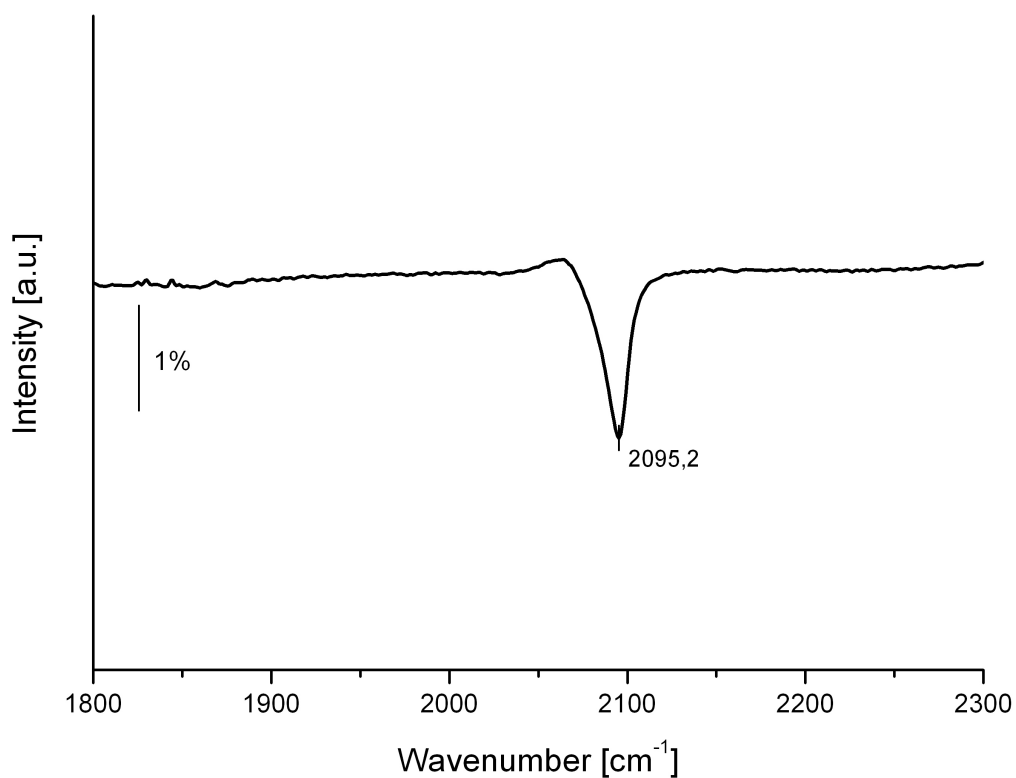


Figure 5.20: FT-IRRA spectrum of a saturation coverage (33L) CO adsorbed on 3 Å Platinum deposited at  $T=300\text{K}$  on  $\text{Al}_2\text{O}_3/\text{NiAl}(110)$ , spectrum recorded at  $T=90\text{K}$

Then CO was adsorbed on Platinum nanoparticles which were deposited onto alumina in different thicknesses. The thicknesses of the deposited Platinum are 0.5 Å , 1 Å , 2 Å , 3 Å according to the reading of the quartz microbalance. The experimental setup described in chapter three was used.

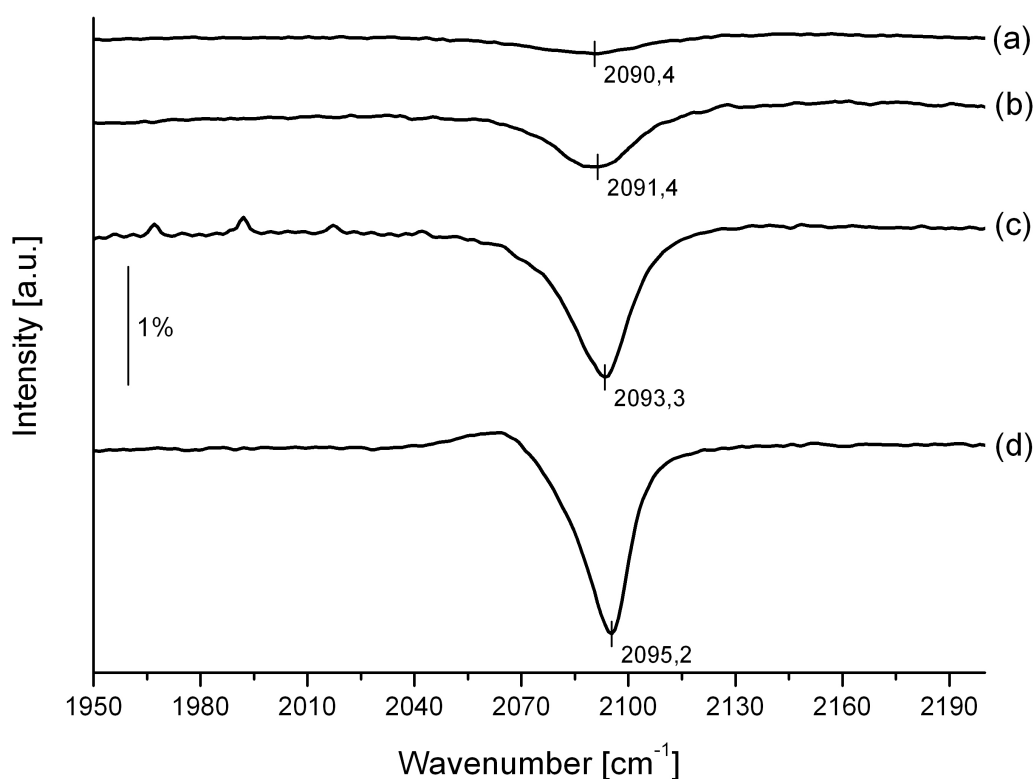


Figure 5.21: FT-IRRA spectra of a saturation coverage of (33L) CO adsorbed on different Platinum deposits. (a)  $0.5\text{\AA}$ , (b)  $1\text{\AA}$ , (c)  $2\text{\AA}$ , (d)  $3\text{\AA}$  (coverage according to microbalance) (Pt deposition:  $T=300\text{K}$ )

The results shown in Figure 5.21 exhibit FT-IRRA spectra of CO adsorbed at the Platinum nanoparticles at 90 K as a function of Pt coverage for CO saturation (33 Langmuir). The frequency of the vibrational peak is  $2090.4\text{ cm}^{-1}$  at  $0.5\text{\AA}$ . The frequency of the vibrational peak increases to  $2095.2\text{ cm}^{-1}$  as the platinum thickness increases up to  $3\text{\AA}$ . First of all the range of the frequencies ( $2090.4\text{-}2095.2\text{ cm}^{-1}$ ) show that the CO adsorbes as on-top species which agree with the results on stepped surfaces [Pt(111), Pt(533), Pt(112)-Pt(335)]. There is no observation of bridge site species.

The CO binds with the  $5\sigma$  orbital to the metal. Meanwhile the electrons of the metal flow to the empty  $2\pi^*$  orbital of the CO. Both these effects will influence the C-O bonding order which results in a change in the vibrational frequency of the adsorbed CO. It was assumed for Platinum that the magnitude of the  $\pi$  back bonding determines the binding strengths. For linear CO on-top species adsorbed on Pt, the overlap between the  $2\pi^*$  orbital of the CO with the d-orbitals of the Pt is small which leads to the small deviation of the vibrational frequency from the gas phase. By increasing

the coordination number the overlap of the  $5\sigma$  orbital of CO with the d-orbitals of the metals is going to be smaller, which make the overlapping of the antibonding  $2\Pi^*$  of the CO with the d-orbitals of the Pt larger. Thus the population of the  $2\Pi^*$  orbital of the CO increases, with a concomitant further weakening of the CO-binding which will decrease the vibrational frequency of the adsorbed CO.

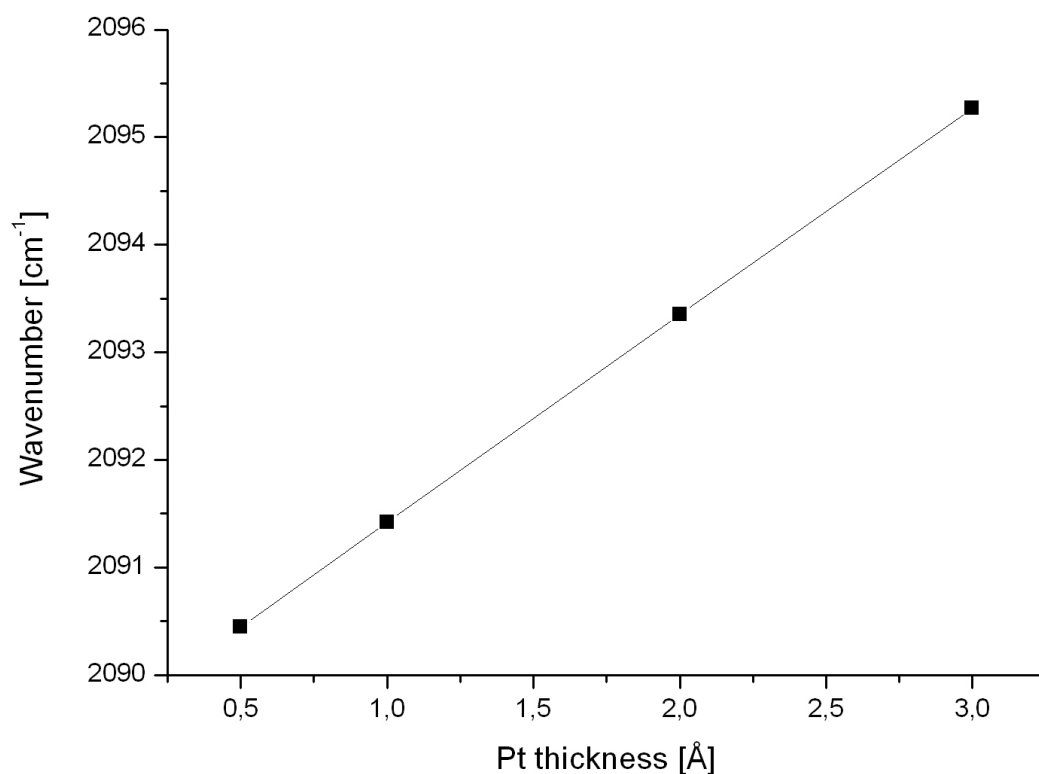


Figure 5.22: The frequency of CO vibrational coverage as a function of nominal Pt thickness according to the microbalance reading (for a saturation coverage of CO)

The frequencies of IR spectra in Figure 5.21 were analyzed. The frequencies of the IR peaks were drawn as a function of the Platinum deposited onto the alumina as shown in Figure 5.22. It is clear that the vibrational frequencies of the CO adsorbed at the platinum increases linearly in this region.



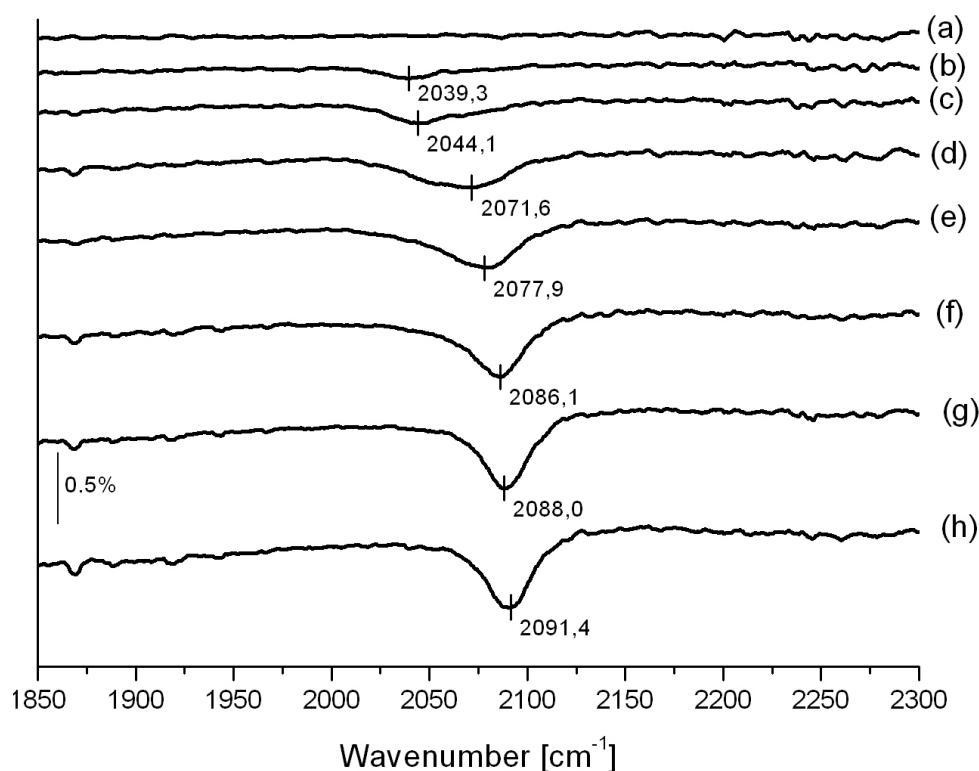


Figure 5.23: FT-IRRAS spectra of CO adsorption coverage on 1 ÅPt deposited at 300K/ $\text{Al}_2\text{O}_3/\text{NiAl}(110)$ . (a) 0L, (b) 0.25L, (c) 0.5L, (d) 1L, (e) 1.25, (f) 1.5L, (g) 2L, (h) 32.25L (CO adsorbed at  $T=90$  K).

Figure 5.23 shows FT-IRRA spectra as a function of CO adsorption coverage on 1 ÅPt deposited at 300K on  $\text{Al}_2\text{O}_3/\text{NiAl}(110)$ . The CO vibrational peak is  $2039.3 \text{ cm}^{-1}$  at 0.25 Langmuir and shifts up to  $2091.4 \text{ cm}^{-1}$ . This strong shift by  $\sim 50 \text{ cm}^{-1}$  is due to 2 species like in Figure 5.8 and due to CO dipole-dipole coupling. An increase in CO coverage further affects the nanoparticle electronic structure in a much stronger way than for the bulk material. Sandell *et al.* (1997) observed changes from a metallic to a molecule like character increasing CO adsorption for Pd aggregate of  $\sim 100$  Pd atoms per island. The bridged bond species was not observed in Pt nanoparticles which would exhibit a frequency of  $1830\text{-}1900 \text{ cm}^{-1}$

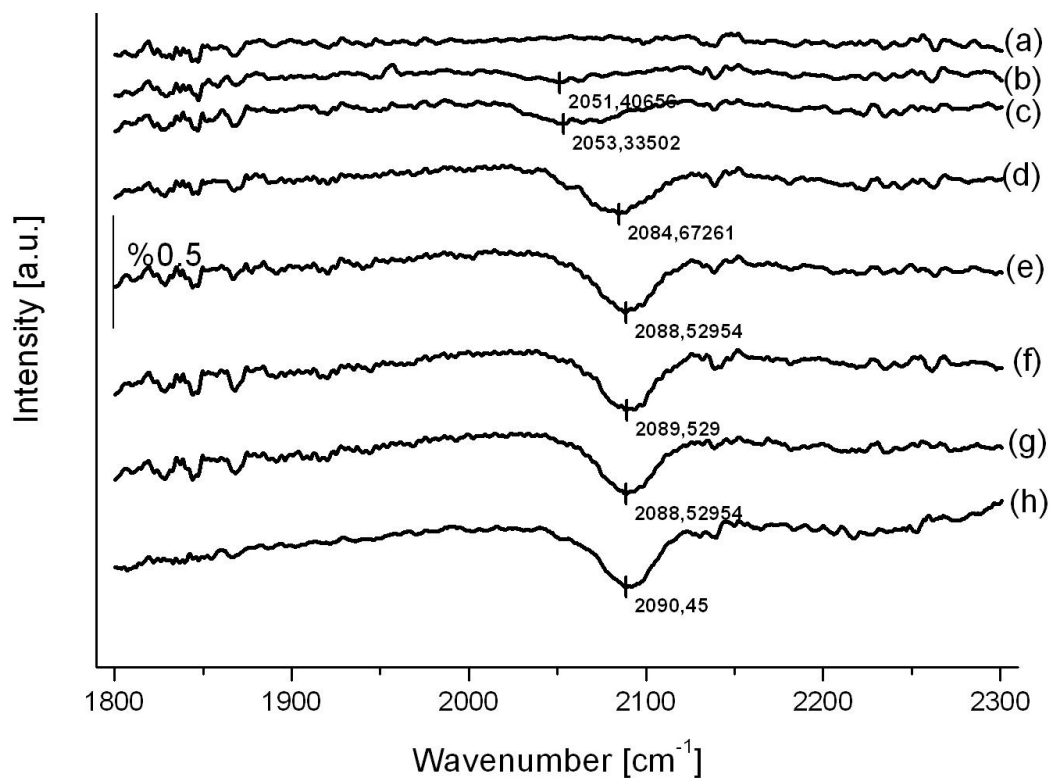


Figure 5.24: FT-IRRAS spectra of CO adsorption coverage on 0.5 Å Pt deposited at 300K/ $\text{Al}_2\text{O}_3/\text{NiAl}(110)$  (a) 0L, (b) 0.25L, (c) 0.5L, (d) 1L, (e) 1.25L, (f) 1.5L, (g) 2L, (h) 33L

Figure 5.24 shows FT-IRRA spectra as a function of CO adsorption coverage on 0.5 Å Pt deposited at 300K on  $\text{Al}_2\text{O}_3/\text{NiAl}(110)$ . The CO vibrational peak is 2051.4  $\text{cm}^{-1}$  at 0.25 Langmuir and shifts up to 2090.45  $\text{cm}^{-1}$ .

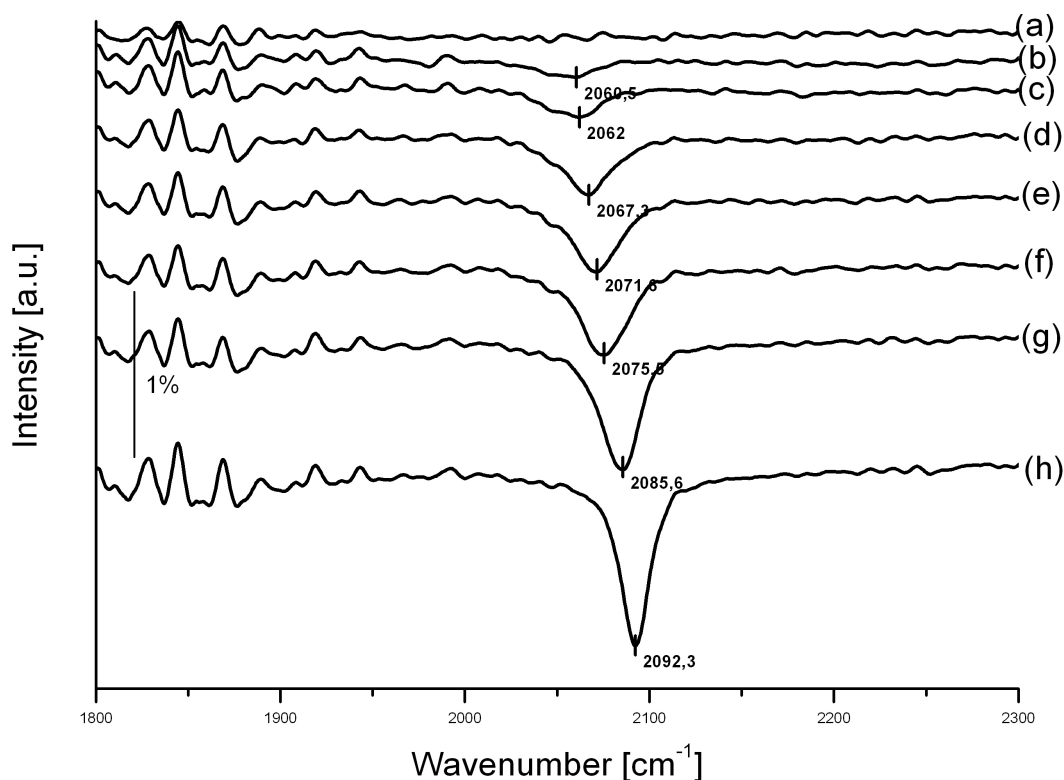


Figure 5.25: FT IRRAS spectra of CO adsorption coverage on 2 Å Pt deposited at 300K/ $\text{Al}_2\text{O}_3/\text{NiAl}(110)$  (a) 0L, (b) 0.25L, (c) 0.5L, (d) 1L, (e) 1.25L, (f) 1.5L, (g) 2L, (h) 33L

Figure 5.25 and Figure 5.26 show FTIRRA spectra as a function of CO adsorption coverage on 2 Å and 3 Å Pt deposited on  $\text{Al}_2\text{O}_3/\text{NiAl}(110)$  respectively. The CO spectra did not show as big shifts as in Figure 5.23 and Figure 5.24.

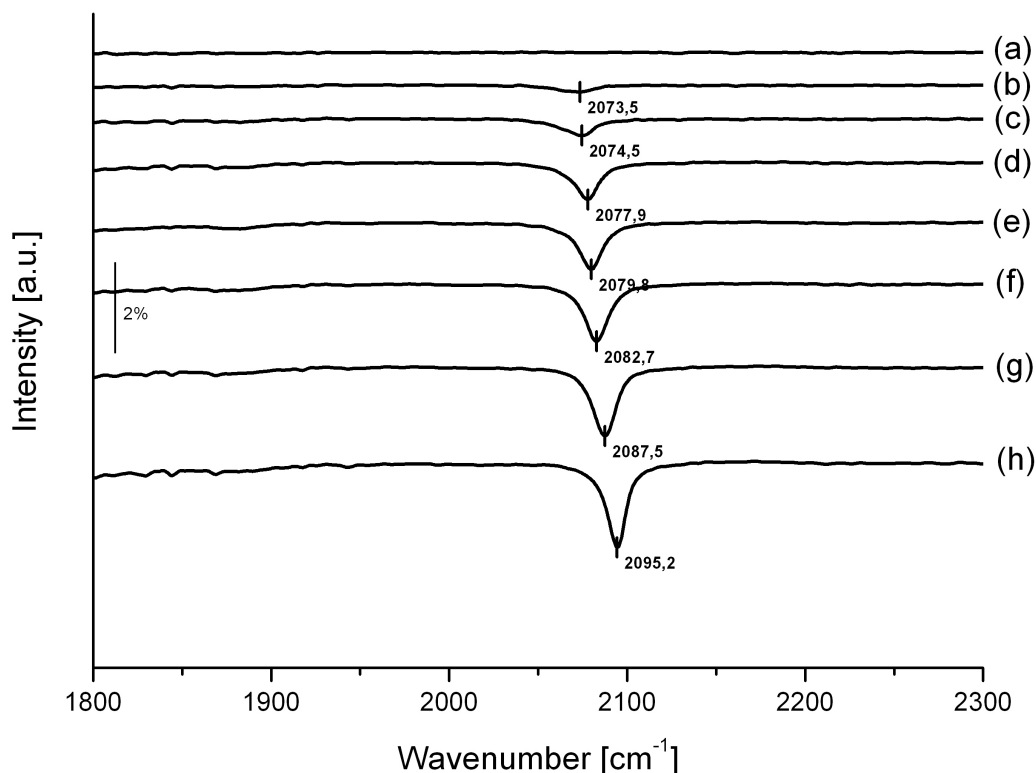


Figure 5.26: FT IRRAS spectra of CO adsorption on 3 Å Pt deposited at 300K/ $\text{Al}_2\text{O}_3/\text{NiAl}(110)$ (a) 0L, (b) 0.25L, (c) 0.5L, (d) 1L, (e) 1.25, (f) 1.5L, (g) 2L, (h) 33L

The spectra in Figure 5.23, Figure 5.24, Figure 5.25 and Figure 5.26 were analyzed. Figure 5.27 shows the growth of the CO peak intensity at different Platinum thicknesses as a function of CO coverage. The figure shows that the growing of the intensity seems to indicate that the intensity saturates near 3 Langmuir. It shows also the difference between the intensities with different Pt thicknesses deposited. The difference is not linear as a function of Platinum thickness, while the vibrational frequencies increase nearly linearly as a function of Platinum thickness. This was interpreted that the IR intensity is proportional to the square of the dipole change (which is nonlinear) according to Güzler (2002).

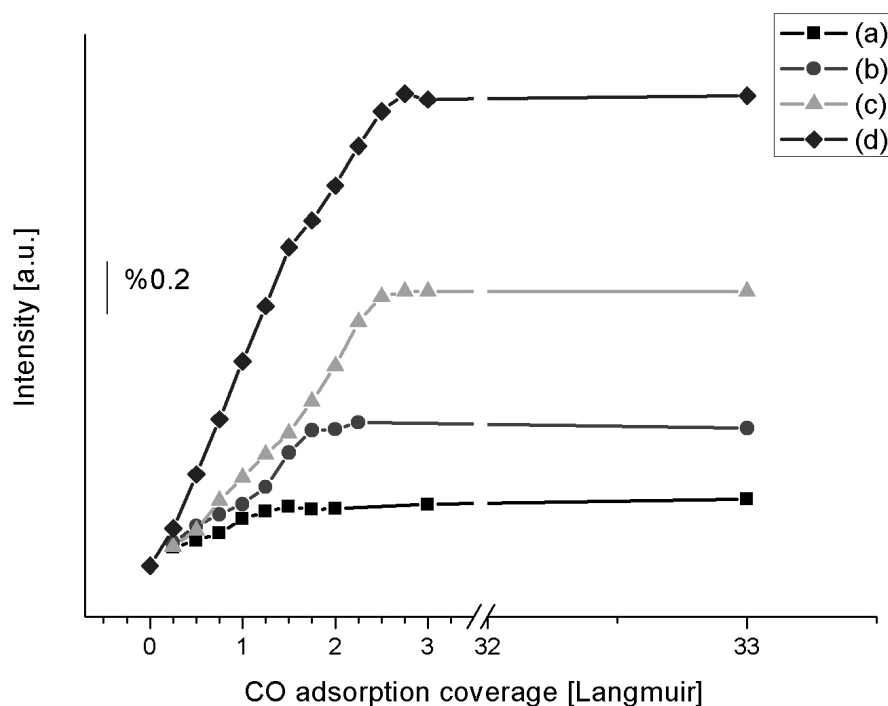


Figure 5.27: Diagram of the intensity of the IR peaks of the CO adsorbed on different Pt nanoparticles as a function of CO adsorption coverage (Pt deposition given in the inlet according to the microbalance reading) (a)  $0.5\text{ \AA}$  Pt (b)  $1\text{ \AA}$  Pt (c)  $2\text{ \AA}$  Pt (d)  $3\text{ \AA}$  Pt

The frequency shift observed is due to the increase of the Platinum thickness because as the thickness of the Platinum increases, the amount of the adsorbed CO will increase, too. Also, the image potential state of the dipole on the surface will be high too which will increase the IR intensity due to the more extended electronic structure. It has to be noted that there is a change within the curves at  $0.9\text{L}$  ( $0.5\text{ \AA}$ ) to  $1.5\text{L}$  ( $3\text{ \AA}$ ) which may indicate a change within the adsorption site (like from edge to terrace site).

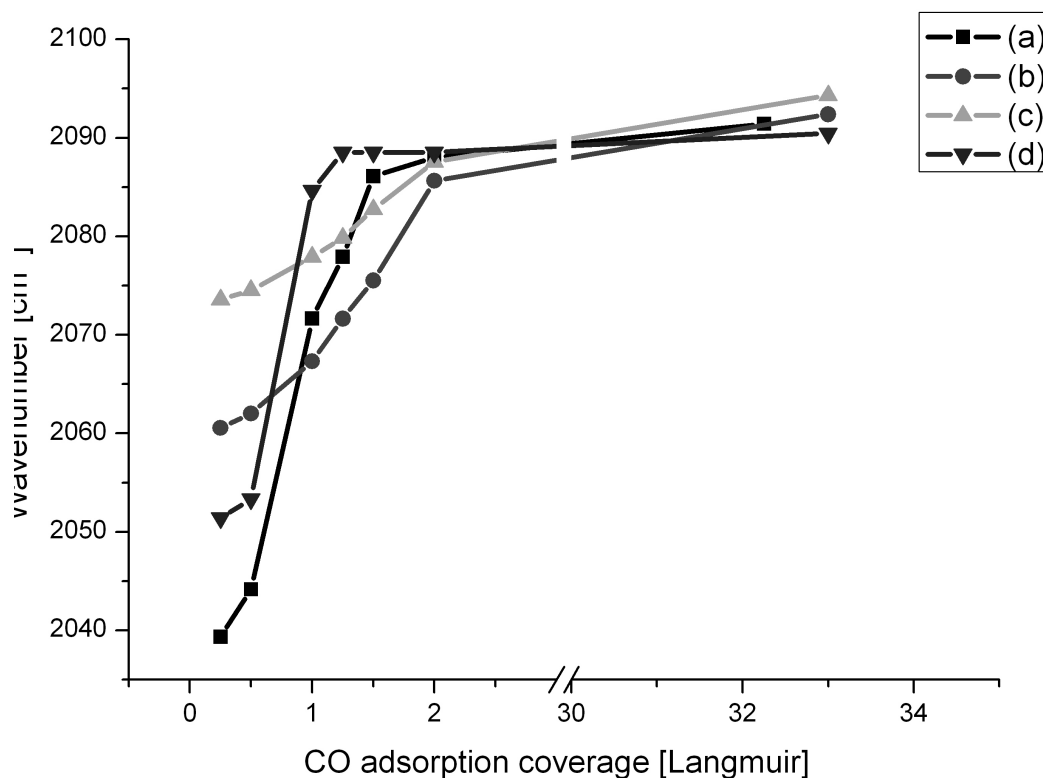


Figure 5.28: Vibrational frequency shifts for different Platinum thickness as a function of CO adsorption coverage (a) 1 Å Pt, (b) 2 Å Pt (c) 3 Å Pt (d) 0.5 Å Pt

Figure 5.28 shows the vibrational frequencies of different Platinum thicknesses as a function of CO adsorption coverage. In general it shows that the vibrational frequency shift decreases as the Platinum thickness increases. The fact is related with the electronic states of the Platinum nanoparticles. The adsorption probability is small according to the area of the Platinum so that only small amounts of the CO adsorb. While in large Platinum nanoparticles, the adsorption probability is larger because of the larger area covered by the Platinum and larger dimensions of the particle. In the larger Platinum particles the effects due to image potential states are larger. While in small Platinum deposition the dipole-dipole effects are stronger. It was recognized in the figure at 0.5 Å that the IR frequency peak starts at lower frequencies than the IR frequency peak of 1 Å. This will be discussed in the next chapter.

#### **5.4 CO desorption from Platinum nanoparticles**

The IR spectra of the Platinum nanoparticles provide us information that the CO adsorbs as on-top linear species. But the question now is where this on-top adsorbs on the Platinum nanoparticles. In general, it could adsorb on terraces and on step-edges and kinks.

Figure 5.29 shows the TPD spectra of the CO adsorbed at  $T=90\text{K}$  on Platinum nanoparticles deposited at the alumina at  $300\text{ K}$ .  $30\text{ Langmuir}$  were adsorbed. The spectra are for different Platinum thicknesses. It shows two different species of the CO on the Platinum and can be classified to high temperature species and low temperature species. The high temperature species peaking at  $443\text{K}-498\text{K}$  belong to the step-edge species which agree with the TPD experiments of the stepped Platinum single crystals. These CO desorption peaks at  $498\text{ K}$  for a deposition of  $0.5\text{ \AA}$  Platinum. The temperature peak is going to shift towards lower temperatures as soon as the Platinum thickness increases. At  $2\text{ \AA}$  Pt the peak is at  $443\text{ K}$ . The lower ability of electron delocalization of the small Pt nanoparticles will weaken the part of the sigma donation and may be also the back donation. This will weaken the adsorption and this explains why the desorption temperature of CO on-top species adsorbed on the Pt nanoparticle are less than on Pt single crystals.

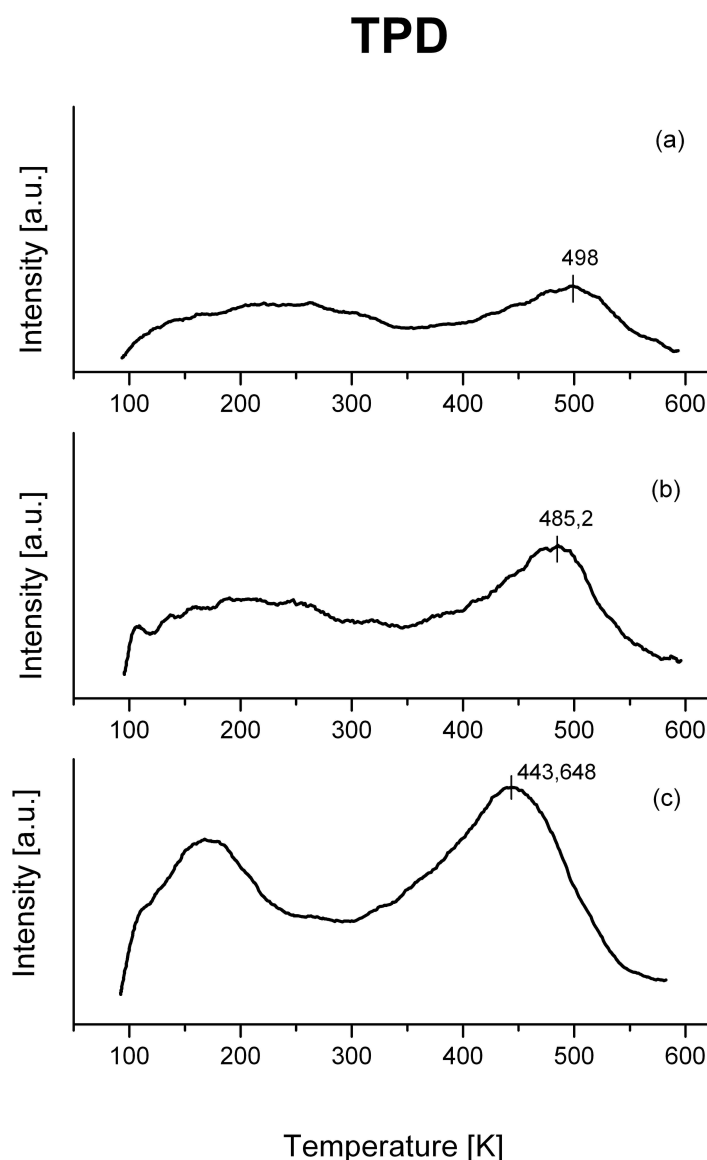


Figure 5.29: TPD experiments of CO saturation coverage adsorbed on Pt nanoparticles. (a)  $0.5\text{\AA}$ , (b)  $1\text{\AA}$ , (c)  $2\text{\AA}$  deposited Pt according to microbalance reading,, heating rate  $1.5\text{ K/s}$  (Pt deposition at  $300\text{K}$ ).

The findings of Figure 5.29 may be compared to data from Winkelmann *et al.* (1994) which are shown in Figure 5.30. They interpreted that at small Platinum deposition the dimensions of the Platinum nanoparticles are small. According to the type of the nucleation of the Platinum at the alumina (which is described in Chapter 4), because of the amorphous aggregation of the deposited Platinum, at low Platinum coverage particles have a higher number of edges and defects. As soon as the Platinum thickness increases the dimensions of the Platinum particles increase. Winkelmann *et*



*al.* (1994) recorded TPD data for Pt nanoparticles at  $\text{Al}_2\text{O}_3/\text{NiAl}(110)$  as a function of Pt coverage (saturation coverages of CO/Pt deposited at 300 K). A second peak appears attributed to a terrace species at high coverages at 7.6 Å see Figure 5.30.

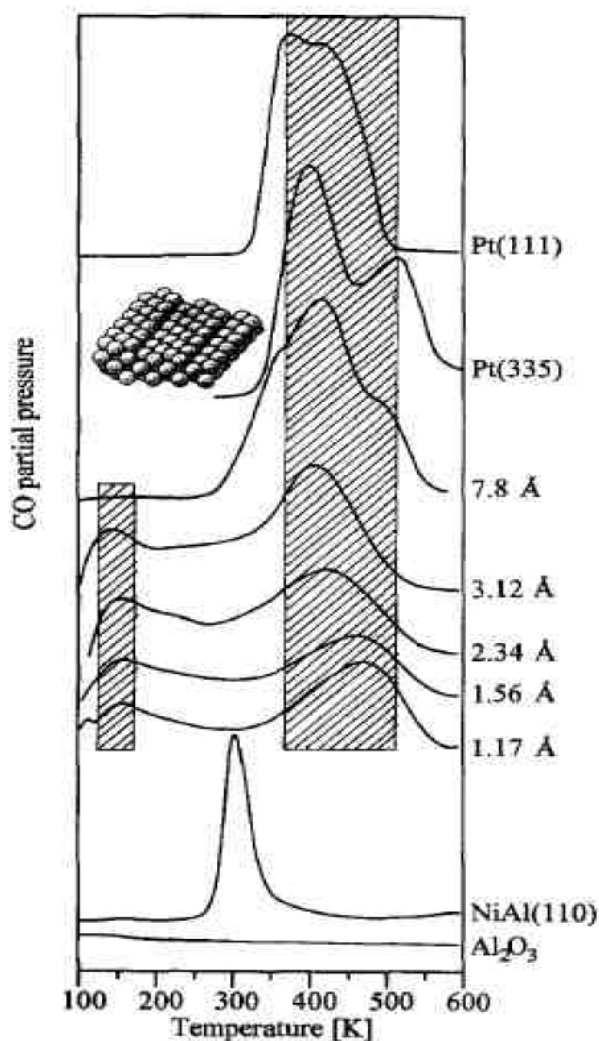


Figure 5.30: Thermal desorption spectra of CO desorbing from  $\text{Pt}/\text{Al}_2\text{O}_3/\text{NiAl}(110)$ . For comparison the TD spectra taken from the literature are included. The two spectra at the bottom refer to the clean  $\text{NiAl}(110)$  substrate and the clean  $\text{Al}_2\text{O}_3(111)/\text{NiAl}(110)$  system. The latter does not adsorb CO above 100 K (Winkelmann *et al.* (1994))

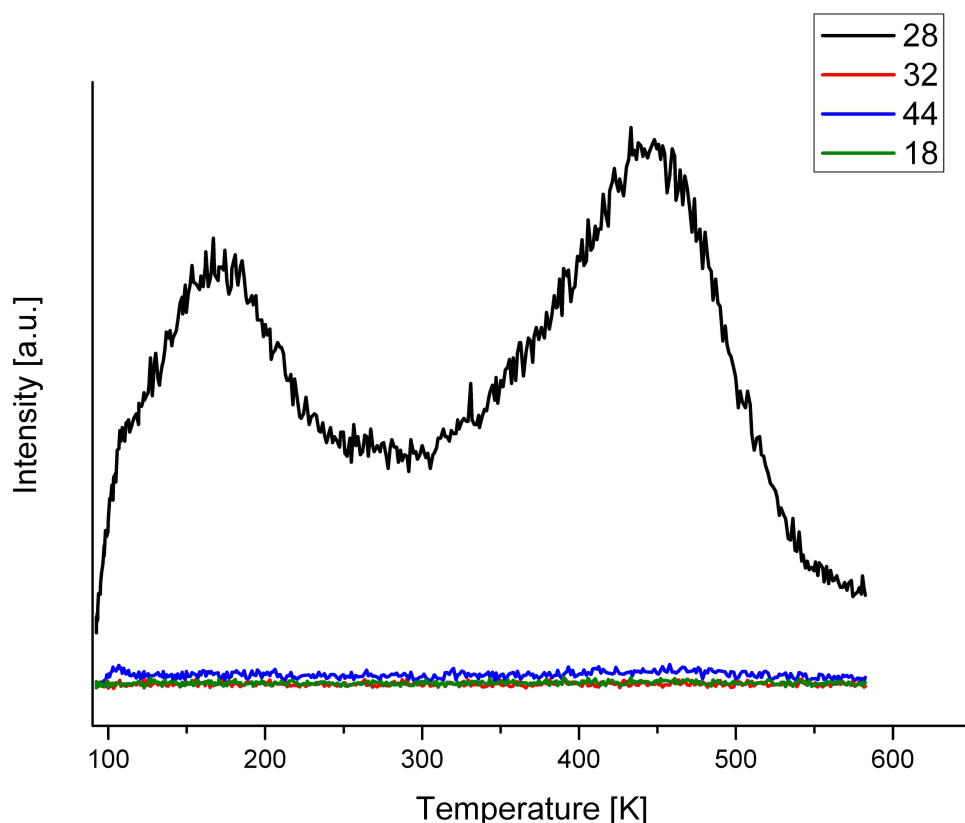


Figure 5.31: TPD spectra of CO saturation coverage adsorbed at 90K on 2 Å Platinum deposited at 300K on alumina. (heating rate 1.5 K/s)

Figure 5.29 also shows low temperature desorption peaks. The desorption temperature start at 220 K in 0.5 Å Platinum deposited on the alumina and it shifts to lower temperatures as the deposition thickness increases, until it reaches 170 K at 2 Å. Winkelmann *et al.* (1994) pointed out that the low temperature peak was not visible at Pt(111) single crystals and not in Pt(335) single crystals. At the same time at these temperatures the CO could not adsorb on alumina and on NiAl(110). So Winkelmann's *et al.* (1994) interpretation for the low temperature desorption peak was that it has to be attributed to the fragmentation of CO<sub>2</sub>. TPD results were analyzed in detail to check if there were CO<sub>2</sub> peaks or other gas desorption peaks. The TPD of 2 Å in Figure 5.31 is a typical example of the TPD of O<sub>2</sub>, CO, CO<sub>2</sub>, N<sub>2</sub>. It is clear that there is no dominant peak beside the CO peak. The conclusion is that in contrast to Winkelmann's *et al.* (1994) interpretation the low temperature peak is not from any residual gases like CO<sub>2</sub>.

Figure 5.7 shows TPD spectra of the CO adsorbed on Pt(533) single crystal and one may be tempted to conclude that this peak belongs to step like adsorption sites. The TPDs of other stepped Platinum single crystals don't show this peak because their figures do not show this temperature range.

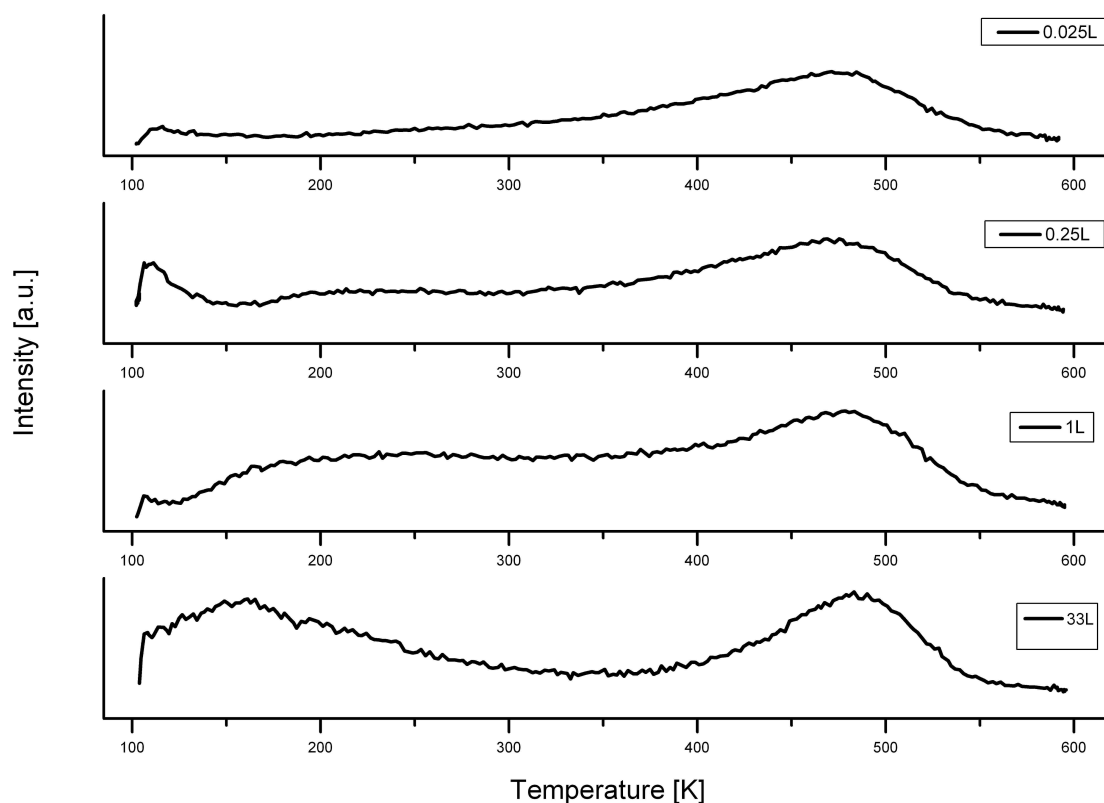


Figure 5.32: TPD spectra of CO adsorbed at  $T=90\text{K}$  on  $2\text{\AA}$  Platinum deposited at  $300\text{K}$  on alumina as a function of CO coverage (normalized to the peak maximum)

One last possibility about this peak is that it may be attributed to the switch on peak when the filament is turned on. CO may adsorb on the filament or the metals of the sample holder. Figure 5.32 shows the TPD of the CO adsorption coverage on  $2\text{\AA}$  Platinum deposited at  $300\text{K}$  onto alumina. These TPD spectra have been normalized to the high temperature peak intensity. The TPD spectrum of the CO adsorbed at  $0.025\text{Langmuir}$  shows that there is no low temperature peak and it is visible that the start on peak at  $120\text{K}$  is small compared to the high temperature peak. The TPD spectrum of the  $0.25\text{Langmuir}$  show that the low temperature peak grows up like a shoulder at  $230\text{K}$ .

It is also easy to distinguish from the start peak of the filament because the start of the filament is very sharp. At 1 Langmuir CO the shoulder is growing and at 33 Langmuir it covers the switch on filament peak.

Another opinion about this peak is that it could be the CO adsorbed on the defect sites of the alumina or in the interface region of the three dimensional Platinum nanoparticles and the alumina. Because the desorption temperature is relatively low, this would result in physisorption bonding.

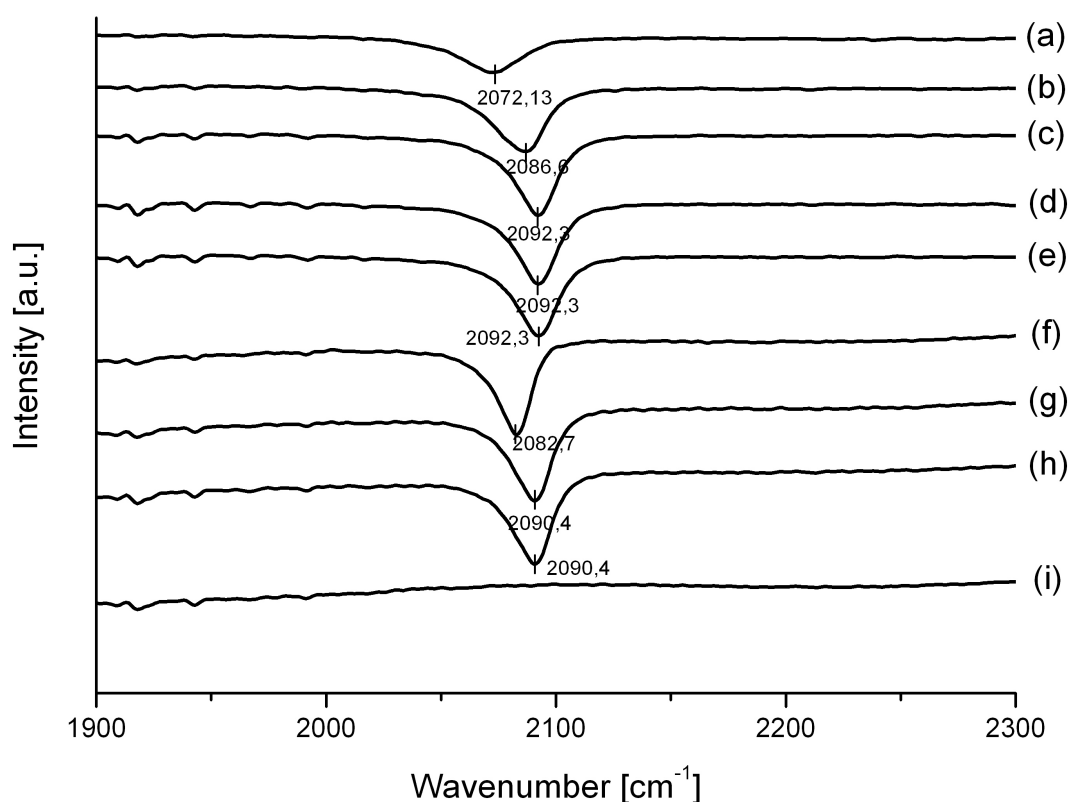


Figure 5.33: FTIRRA spectra of CO adsorbed at  $T=90\text{K}$  on  $2\text{\AA}$  Pt deposited at  $300\text{K}/\text{Al}_2\text{O}_3/\text{NiAl}(110)$ . (a) 1L, (b) 2L, (c) 3L, (d) 4L, (e) 5L, (f) Tempering to 230 K, (g) Tempering to 230 K+3L, (h) 230 K+4L, (i) TDS to 600K

A CO tempering experiment was done. As shown in Figure 5.33, the spectra (a), (b) to (e) is the CO adsorption at  $T=90\text{K}$  coverage on  $2\text{\AA}$  Platinum deposited onto alumina at  $300\text{K}$ . Figure 5.34 (a) shows a TPD experiment of the same sample heated to  $300\text{K}$ . Figure 5.33. (f) is the corresponding FTIRRAS after the tempering. It shows that the CO vibrational peak shifts which is due to desorption of CO at the low temperatures.

However, it is remarkable that the intensity is stronger than in Figure 5.33. (e) despite the fact that there is less CO adsorbed. There is apparently less intensity transfer to higher vibrational frequencies as these adsorption species are not present. From this results it was concluded that the low temperature peak in the TPD is from on-top adsorbed CO. The (g) & (h) spectra show the CO vibrational peak after dosing 3 Langmuir and 4 Langmuir respectively. They show how the CO vibrational peaks start to shift to higher frequencies as normal to CO adsorption. However, the final frequency is by  $2\text{ cm}^{-1}$  lower than for Figure 5.33. (e) although the coverage should be comparable. The intensity of the peak also decreased slightly from Figure 5.33. (f) to Figure 5.33. (h). After that a TPD was done up to 600 K and the results are shown in Figure 5.34 (b). Two desorption peaks of the CO are apparent. Apparently there is a shift of the low temperature desorption peak indicating some dynamical changes during tempering experiment. The shift towards lower temperature indicates some surface annealing. This is also apparent from the FT-IRRA spectra which are different from simple background dosing. After another TPD was done, we see that the CO vibrational peak has disappeared as shown in Figure 5.33 (i).

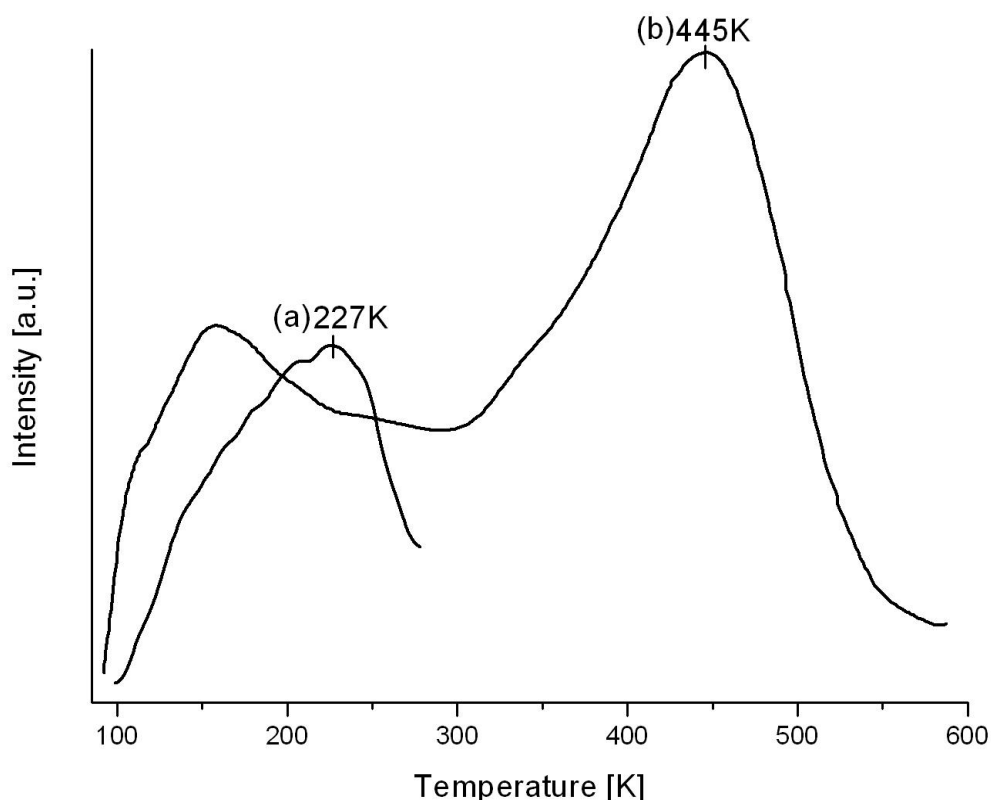


Figure 5.34: TPD of CO adsorbed at  $T=90\text{ K}$  on  $2\text{ \AA}$  Pt deposited at 300 K at alumina. (a) TDS to 300 K, (b) TDS to 600 K after redosing 4L CO (heating rate 1.5 K/s)

## 5.5 Discussion

The CO adsorption on the platinum nanoparticles is clearly assigned to on-top bonding when comparing the vibrational frequency to on-top CO on single crystals. There are no indications for bridge bonding. The vibrational frequency of the CO shifts to higher frequencies as the thickness of the Platinum deposited on the alumina increased. The TPD experiments exhibits two peaks which depend on the average particle size. An unusual low temperature peak may give rise to two interpretations. TPD data on Pt(533) from Hayden could indicate a species found on stepped surfaces though their data do not allow a clear distinction from a “switch on” peak. Another option is that this species is adsorbed on the interface boundary of the Platinum nanoparticles and the alumina. The low temperature peak is clearly depending on the particle size. The CO-interaction of the physisorbed species is strongest for the smallest particles and for lower CO coverages which clearly excludes a “switch on” peak. Such strong shifts for smaller particles are not apparent for the high temperature peak which was clearly attributed to edge sites. So the low temperature peak is more sensitive to the particle size which indicates a stronger influence of the particle-support interaction. Therefore the interpretation is favored that adsorption at perimeters occurs. From the tempering experiments it is clear that the initial coverage density on the metal particle itself is very delicately influenced by the perimeter-adsorption.

Crystal	On-top species frequency (cm <sup>-1</sup> )	Bridged species frequency (cm <sup>-1</sup> )		Reference
Pt(111)	2140	1857	405K	Heyden & Bradshaw (1983)
Pt(533)	2097		104-385.2-497.7K	Hayden <i>et al.</i> (1985)
Pt(321)	2095	1865	435.8-545.5	McClellan <i>et al.</i> (1981)
Pt(335)	2092	1880	392.5-495.6	Xu & Yates (1995)
Pt(112)	2091	1854	388.8-506	Xu & Yates (1995)
0.5ÅPt/Al <sub>2</sub> O <sub>3</sub>	2090.4		498	
1ÅPt/Al <sub>2</sub> O <sub>3</sub>	2091.4		485.2	
2ÅPt/Al <sub>2</sub> O <sub>3</sub>	2093.3		443.6	
3ÅPt/Al <sub>2</sub> O <sub>3</sub>	2095.2			

## 6 Laser induced processes of CO at Pt surfaces using nanosecond laser

Chapter five has shown the mechanism of CO adsorption at Platinum surfaces (single crystals, nanoparticles) and the CO temperature programmed desorption (TPD). The focus of this chapter will be on the laser induced CO desorption from Platinum surfaces. First laser induced CO desorption from Platinum single crystals will be discussed. After that it will be compared to the laser induced desorption from Platinum nanoparticles.

Photoinduced processes on solid surfaces are increasingly important and interesting (Chiang 2000, Avouris & Walkup 1989, Zhou *et al.* 1991). Photons can selectively induce a specific process at a specific state. So the use of photons may provide us with a tool to control a surface reaction in a delicate way which is not achievable in a thermal process. There are few studies reported on CO photo desorption from metallic surfaces. In the previous studies, photons at 193 nm induced CO desorption from Pt(001) and Pt(111) (Peremans *et al.* 1993, Peremans *et al.* 1993a). The CO desorption from Pt(001) and Pt(111) was detected by (2+1) REMPI via the B←X transition, (Peremans *et al.* 1993, Peremans *et al.* 1993a, Fukutani *et al.* 1993) which could not resolve each rotational state. In the electron-stimulated desorption (ESD) studies, on the other hand, excited neutral CO\* in the  $a^3\Pi$  state desorbed from Pt(111) as detected by (1+1) REMPI via the b←a transition (Burns *et al.* 1987, Burns 1993).

On a clean Ni(111) surface CO molecules are not desorbed by UV photons (Guo *et al.* 1990, Magkoev *et al.* 1995). Application of a short pulse laser succeeded in stimulating desorption of CO from Cu(111)(Prybyla *et al.* 1992). On insulating surfaces, on the other hand, CO molecules are desorbed by photons irradiation from NiO(111)/Ni(111)(Asscher *et al.* 1992, Yoshinobu *et al.* 1991) and Cr<sub>2</sub>O<sub>3</sub>/Cr(110)(Al-Shamery *et al.* 1994) with large cross sections. In contrast to photostimulated desorption, there are some ESD studies reported for CO from Ru(001),(Auer *et al.* 1987) W(001), (Kronauer & Menzel 1972) Pt(111), (Kiskinova *et al.* 1988, Burns *et al.* 1987, Burns 1993) and Ni(110) (Alvey *et al.* 1986).

The fluence dependence of the desorption yield suggests that CO desorption occurs as three-

photon and single-photon process from Pt(001) and Pt(111), respectively. For CO from Pt(001), adsorbate excitation seems to be responsible for the desorption.

## 6.1 Laser induced CO desorption from Pt(111) single crystal

In order to get a comparison to literature data and own work on nanoparticulate Pt particles measurements were done with the experimental set up used in this work with a Pt(111) crystal.

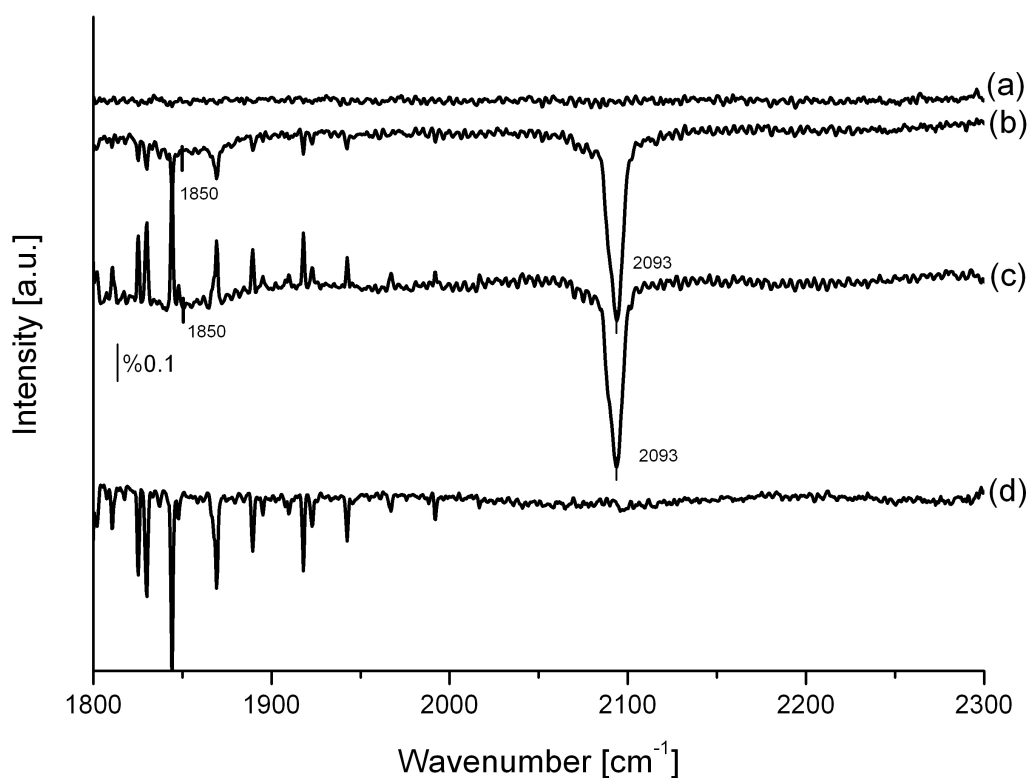


Figure 6.1: FT-IR spectra of CO adsorbed on Pt(111) crystal. (a) 0L, (b) 30 L, (c) after Laser irradiation, (d) (b)-(c) with a laser fluence of  $25.5 \text{ mJ/cm}^2$  ( $\lambda=355 \text{ nm}$ )

After the well known Pt(111) LEED pattern was obtained from cleaning the surface by sputtering, the sample was transferred to the T-piece chamber for FT-IR measurements. After measuring the background, the spectrum (a) in Figure 6.1 was recorded as background spectrum indicating the lack of CO adsorption.



30 Langmuir of CO were dosed to the Pt(111) single crystal. The FT-IR spectrum in Figure 6.1(b) shows two CO vibrational peaks. The first vibrational frequency is  $2093\text{ cm}^{-1}$  which is related to the on top species. The second vibrational frequency at  $1850\text{ cm}^{-1}$  is related to bridge bond species. Due to fluctuations of humidity during the measurements there are different amounts of water vapor in the spectrometer visible as rather sharp peaks. These results are in agreement to the Pt(111) results discussed in Chapter 5.

Laser pulses of 6 ns pulse duration at  $\lambda=355\text{ nm}$  were generated by frequency tripling of 1064 nm from a Nd:YAG Laser with energies up to  $25.5\text{ mJ/cm}^2$ . The beam was aligned perpendicular to the sample. Figure 6.1(c) shows the FT-IR of a CO saturation coverage adsorbed on Pt(111) after irradiation of  $1.33 \times 10^{20}$  photons. There is no change in the intensity and the frequency of the CO vibrational peak. The spectrum in Figure 6.1(d) exhibits the subtraction of (c) from (b) which is practically zero. That means according to the FT-IR spectra no CO desorption occurs at this laser intensity. The same experiment was repeated with different laser intensities of  $6.4\text{ mJ/cm}^2$ ,  $12.7\text{ mJ/cm}^2$ ,  $19.1\text{ mJ/cm}^2$  and  $25.5\text{ mJ/cm}^2$ . All of them show the same results, i.e. no CO desorption occurs from Pt(111) at these intensities.

Figure 6.2(a) shows a FT-IR spectrum of 0.5 L of  $^{13}\text{CO}$  on Pt(111) at 80 K from the work of Fukutani *et al.* (1995). In order to avoid adsorption of residual  $^{12}\text{CO}$  in the UHV chamber, the isotope of  $^{13}\text{CO}$  was used for this low-coverage experiment. According to the previous studies, an absorption peak appearing at  $2045\text{ cm}^{-1}$  is assigned to the stretching vibration of  $^{13}\text{CO}$  adsorbed on the on-top site.

The sample was irradiated at 193 nm with an incident fluence of  $4\text{ mJ/cm}^2$  for 10, 20, and 30 min at 10 Hz. The on-top CO decreases gradually in intensity as shown in Figure (b)(c) and (d), respectively. While on-top CO decreases, bridge-bound CO seems to remain intact (Hayden *et al.* 1983, Tüshaus *et al.* 1987).

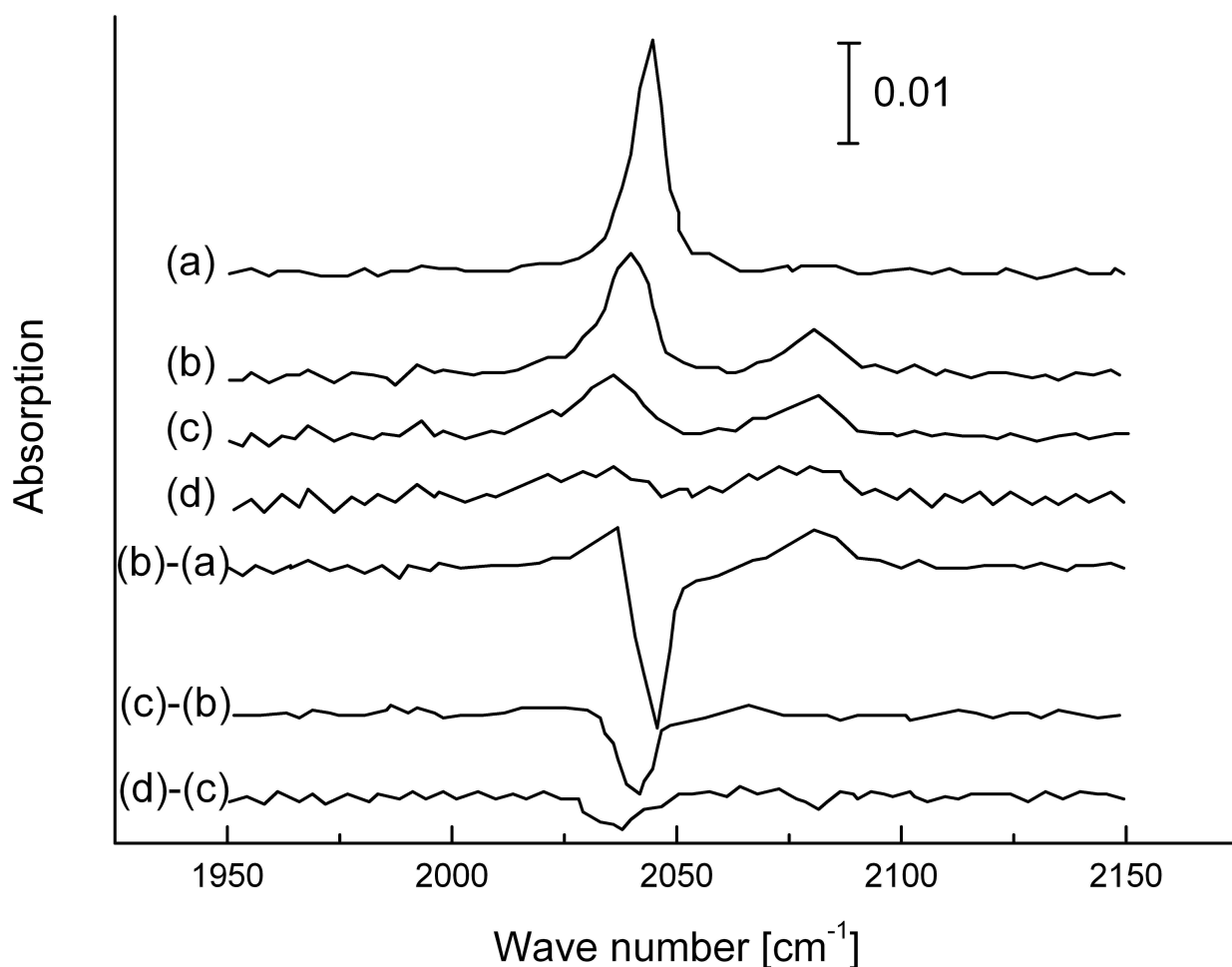


Figure 6.2: FTIR spectra for  $^{13}\text{CO}$  on Pt(111) at 80 K, (a) after 0.5L dose of CO, (b), (c), and (d) after laser irradiation on the sample corresponding to (a) at 193 nm with  $4 \text{ mJ/cm}^2$  for 10, 20, and 30 min with a repetition rate of 10 Hz, respectively. Also shown are difference spectra. (Fukutani et al. 1995)

The absorption peak that appears at  $2080 \text{ cm}^{-1}$  in Figure 6.3(b)-(d) corresponds to the stretching vibration of  $^{12}\text{CO}$ . Figure 6.3(b),(c),(d) show the change of the spectrum due to laser irradiation ( $\lambda=193 \text{ nm}$ ) for 10, 20, and 30 min, respectively, with an incident pulse fluence of  $4 \text{ mJ/cm}^2$  at 10 Hz. The absorption peak intensity decreases with photon irradiation on the sample indicating that the CO coverage decreases by desorption and/or dissociation. The peak position slightly shifts to the lower frequencies with photon irradiation. The difference spectra between two of these are also shown in Figure 6.3. It can be concluded that the Laser induced desorption of CO adsorbed on the Pt(111) occurs at 193 nm even at lower laser intensities, while nearly no CO desorption is observed at 355nm even for the higher laser intensities. This is because of the difference of the photon energy

to excite the necessary electrons to desorb the CO. It was decided to use a photon energy of  $\lambda = 355$  nm for the experiments with the Platinum nanoparticles.

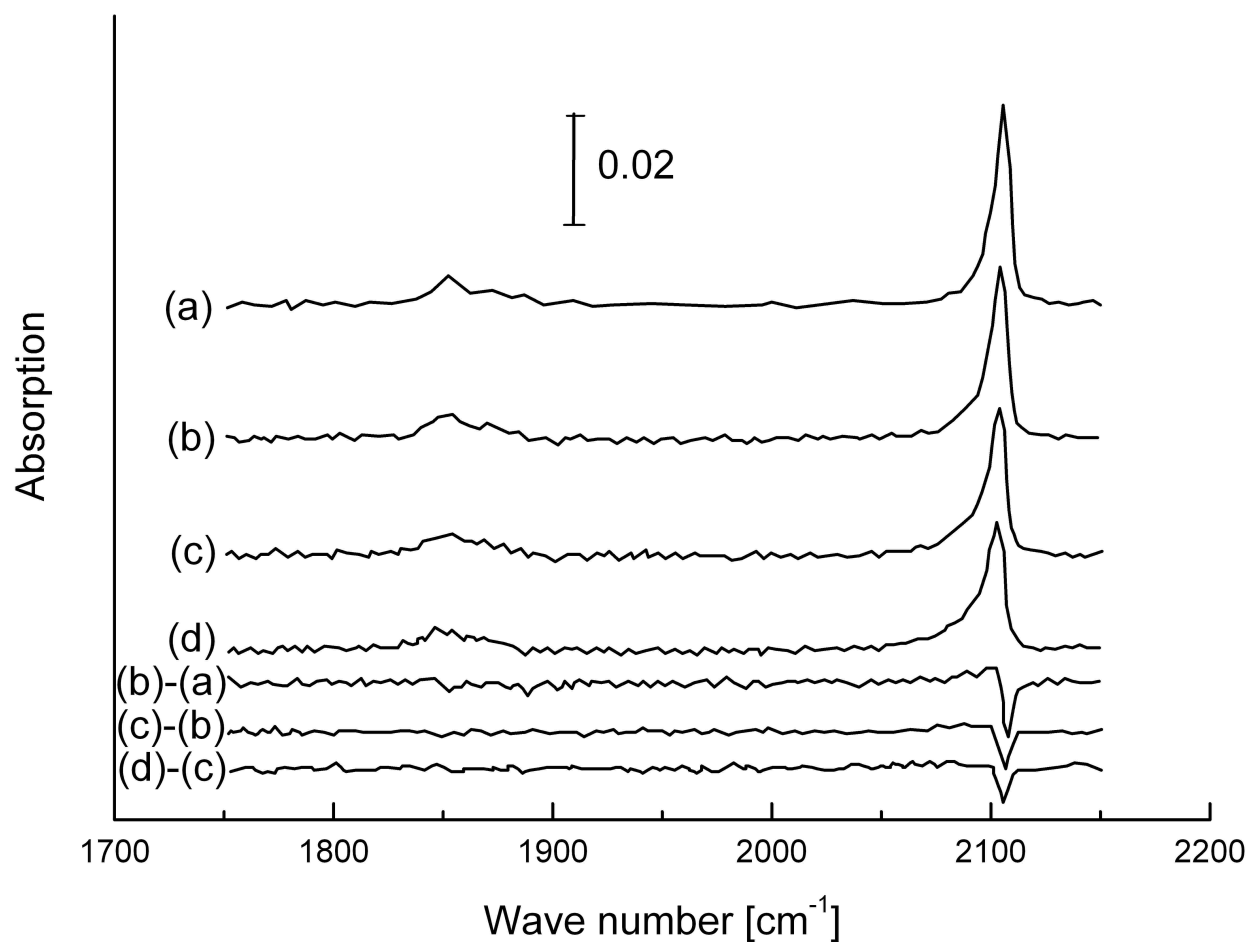


Figure 6.3: FTIR spectra for CO on Pt(111) at 80 K, (a) after 2 L dose of <sup>12</sup>CO, (b), (c), and (d) after laser irradiation on the sample corresponding to (a) at 193 nm with 4 mJ/cm<sup>2</sup> for 10, 20, and 30 min with a repetition rate of 10 Hz, respectively. Also shown are difference spectra (Fukutani et al. 1995)

## 6.2 The effect of Laser induced CO desorption from Pt deposited at 300K

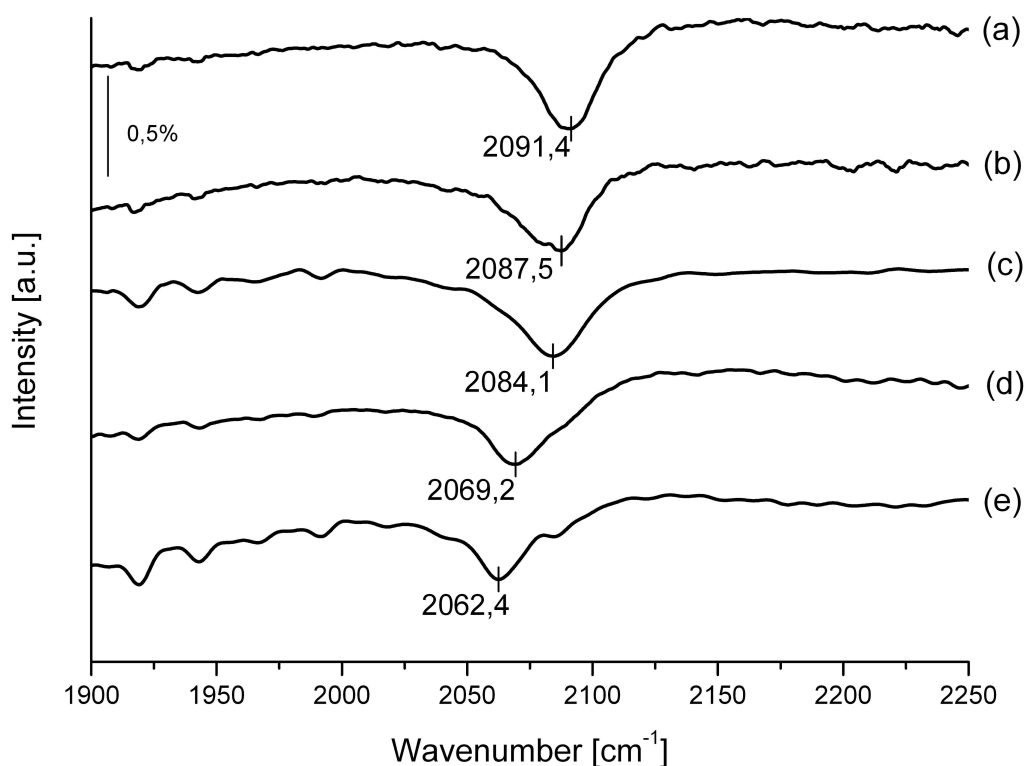


Figure 6.4: FTIR spectra of CO adsorbed at  $T=90\text{K}$  on  $1\text{\AA}\text{Pt}$  deposited at  $300\text{K}$  after laser irradiation. (a)33L, (b) $6.4 \text{ mJ}/\text{cm}^2$  ( $1.78 \times 10^{19}$  Photons), (c) $12.7 \text{ mJ}/\text{cm}^2$  ( $1.78 \times 10^{19}$  Photons), (d) $19.1 \text{ mJ}/\text{cm}^2$  ( $2.67 \times 10^{18}$  Photons), (e) $25.5 \text{ mJ}/\text{cm}^2$  ( $3.57 \times 10^{18}$  Photons)

In this section the effect of the laser intensity is studied for CO desorption from Pt nanoparticles from  $1\text{\AA}$  deposition at  $300\text{K}$  onto alumina. The sample was irradiated with a Nd:YAG laser at  $355\text{nm}$ ,  $6 \text{ ns}$  pulse duration with a repetition rate of  $10 \text{ Hz}$ . Figure 6.4 shows FTIR spectra of the CO after excitation of a saturation coverage with different laser fluences. Figure 6.4 (a) exhibits a CO saturation coverage of the adsorbed CO. Figure 6.4 (b)-(e) show the frequency shift and intensity changes in the CO vibrational peaks as a function of laser fluence. It is clear that the stronger the sample was irradiated the more the vibrational frequency shifts to lower frequencies

accompanied by a decreasing of the peak intensity. These changes are observed for the first hundred pulses of the irradiation for higher laser fluence. The overall amount of photons impinged onto the surface which is necessary to reach the final state depends on the laser fluence and ranges from  $1.78 \times 10^{19}$  photons to  $2.67 \times 10^{18}$  with increasing laser fluence. Figure 6.5 depicts the corresponding shift of the CO stretching vibration peak as a number of photons impinged onto the surface for various laser fluences used.

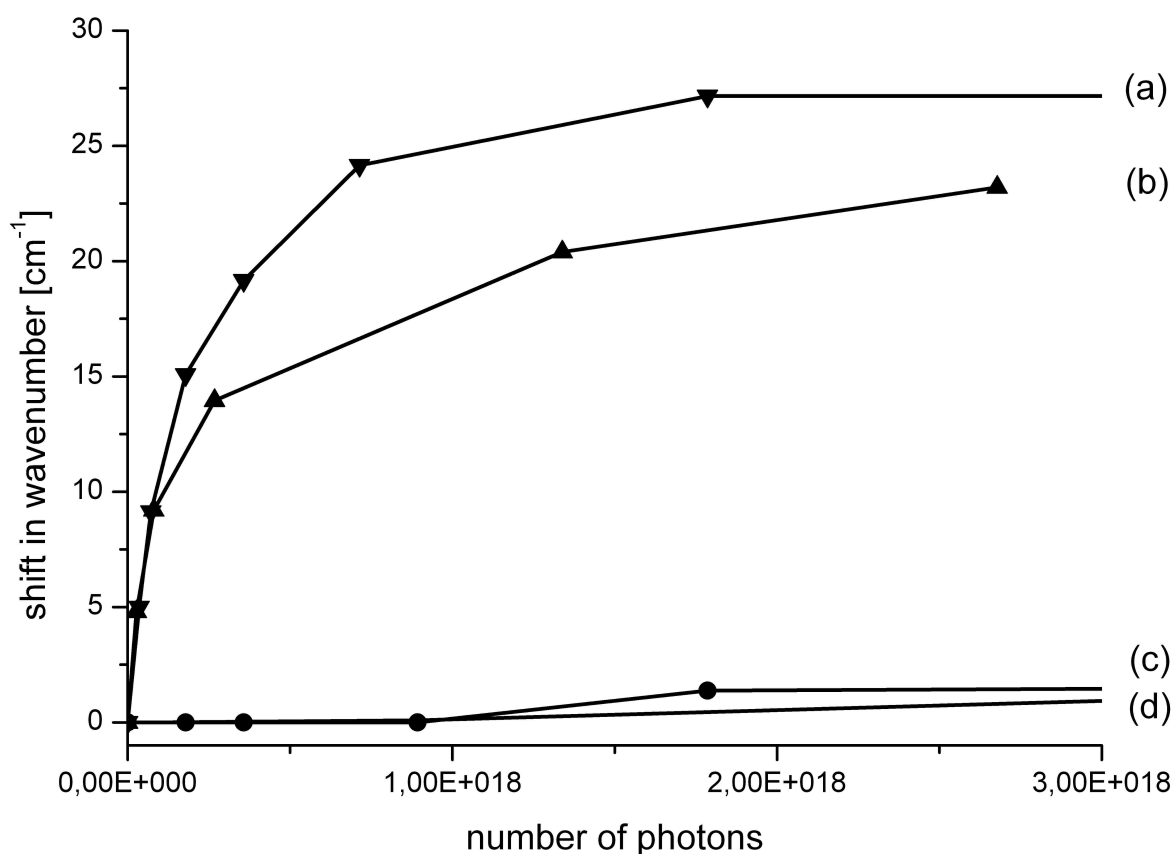


Figure 6.5: Frequency shift of CO vibrational peaks after laser irradiation as a function of laser fluence. (a) 25.5 mJ/cm<sup>2</sup>, (b) 19.1 mJ/cm<sup>2</sup>, (c) 12.7 mJ/cm<sup>2</sup>, (d) 6.4 mJ/cm<sup>2</sup> for 33L CO adsorbed at 1 Å Pt/alumina at 300K

As shown in Figure 6.5(d), for 6.4 mJ/cm<sup>2</sup> the frequency shift does not occur for the first laser pulses. It starts to occur slowly in the range of 1000 pulses. The IR-peak shifts maximally by 2-3 cm<sup>-1</sup>. Figure 6.5(c) exhibits the experiments using 12.7 mJ/cm<sup>2</sup>. They do not differ significantly to

Figure 6.5(d). For the first single shots no changes in the frequency of the vibrational peak is found. Frequency shifts start to appear at more than 600 pulses and the maximal shift is 3-4  $\text{cm}^{-1}$ .

Prominent changes in the frequency are observed for 19.1  $\text{mJ}/\text{cm}^2$  shown in Figure 6.5 (b) even for the first pulses. This shift by 5  $\text{cm}^{-1}$  is larger than the shift observed for thousands of pulses at lower intensities. It continues to grow by increasing the number of photons impinged. The frequency shifts reach maximally a range of 22  $\text{cm}^{-1}$ . The 25.5  $\text{mJ}/\text{cm}^2$  experiment has the same behavior as the 19.1  $\text{mJ}/\text{pulse}$  experiment, the frequency shift starts with the first laser pulses. The difference is that it has higher frequency shifts up to 25  $\text{cm}^{-1}$  as shown in Figure 6.5(a).

Figure 6.6 shows the FTIR spectra of the CO adsorption coverage on 1 Å Pt at 300K / $\text{Al}_2\text{O}_3/\text{NiAl}(110)$ . The frequency shift of the CO vibrational peak was discussed in Chapter 5 as related to a dipole-dipole interaction and to a second on-top species. Figure 6.6 shows the FTIR of CO stretching vibration region after exposing a saturation coverage of CO at 33L dosed at 90 K to laser pulses of fluence 19.1  $\text{mJ}/\text{cm}^2$ .

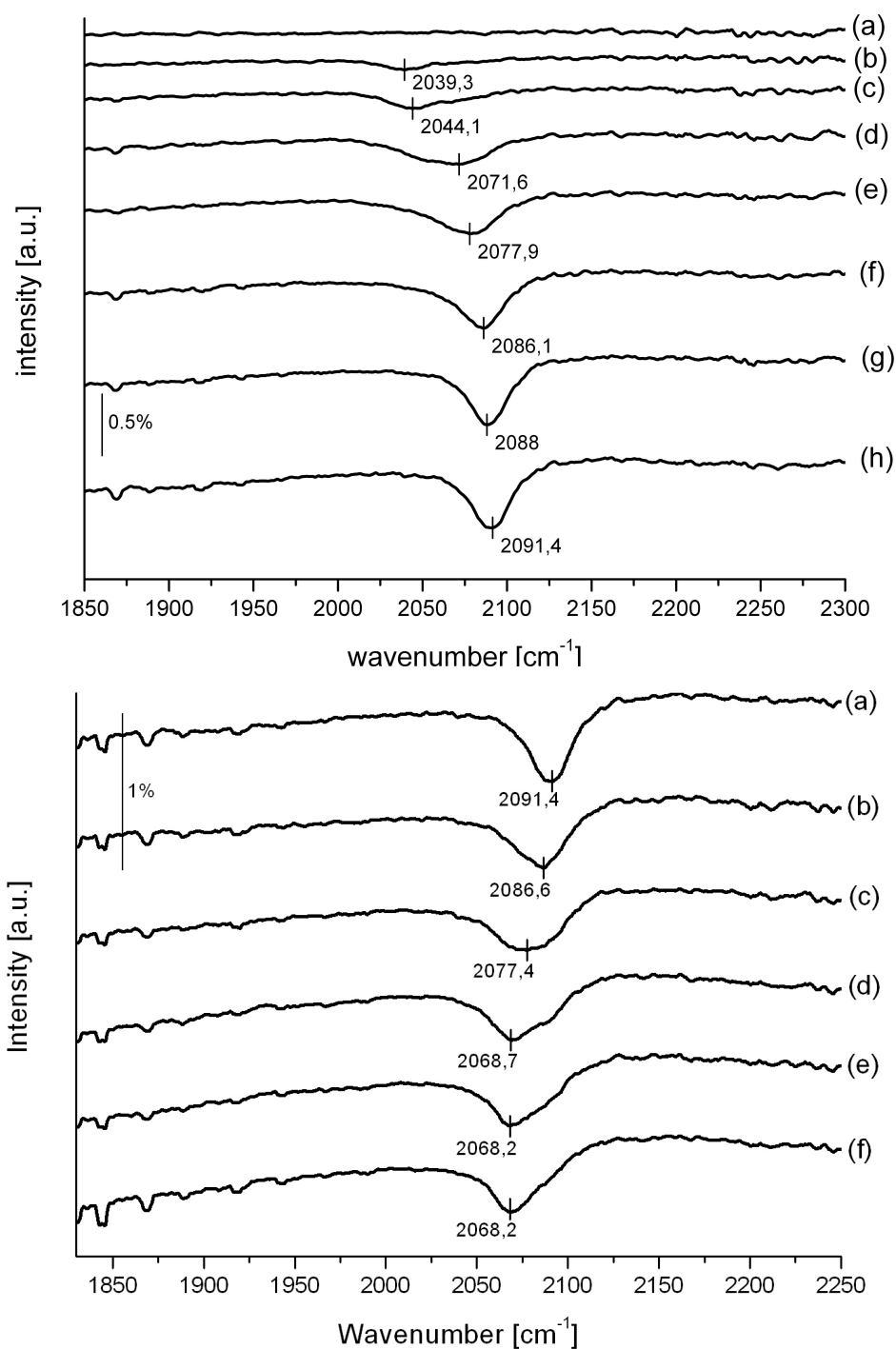


Figure 6.6: FTIR spectra of CO adsorption coverage on 1 Å Platinum deposited at 300K over alumina. (a)0L, (b)0.25L, (c)0.5L, (d)1L, (e)1.25L, (f)1.5L, (g)2L, (h)32.25L FTIR spectra of CO adsorbed on 1 ÅPt at 300K before and after laser irradiation 19.1 mJ/cm<sup>2</sup> (a)33L, (b)1.78\*10<sup>19</sup> Photons, (c)1.78\*10<sup>19</sup> Photons, (d)2.67\*10<sup>18</sup> Photons, (e)3.57\*10<sup>18</sup> Photons

Figure 6.7 summarizes the change in the intensity from the saturation coverage (in percent). One has to be careful with relating IR intensities to a certain coverage. Both, peak shifts and intensity changes indicate a substantial desorption of CO with increasing laser fluence. At  $6.4 \text{ mJ/cm}^2$  the intensity change starts smoothly and slightly earlier than the frequency shift. The intensity change linearly increases up to 5% from the CO saturation coverage. Similar to the frequency shift, the  $12.7 \text{ mJ/cm}^2$  experiments exhibits slightly bigger shifts than the  $6.4 \text{ mJ/cm}^2$  experiment. The change in the intensity scales linearly with the photon flux and it saturates near 10% from the CO saturation coverage. The big dominant change happens at  $19.1 \text{ mJ/cm}^2$ . Within the first pulses the percentage change is near 20%. After a few pulses the change reaches its maximum around 33% from the CO saturation coverage. Then it saturates after slightly decreasing to 30% from the CO saturation coverage. The same was observed for the  $25.5 \text{ mJ/cm}^2$  experiments. The changes occur at the first pulses and stop after a total change of 35% from the CO saturation coverage.

The conclusion from Figure 6.5 and Figure 6.7 is that the changes in the CO vibrational peak do not change linearly with the laser intensity.

There is an apparent change between the results of the laser intensities of  $6.4 \text{ mJ/cm}^2$ ,  $12.7 \text{ mJ/cm}^2$  as a group and the results of  $19.1 \text{ mJ/cm}^2$ ,  $25.5 \text{ mJ/cm}^2$  as another group. It could be speculated that multi photon processes could occur at higher laser intensities.

In general the phenomenon of the frequency shift in the CO vibrational peaks and the change in the peak intensity can be attributed to the inverse process of the CO adsorption coverage. When the CO amount decreases because of the laser induced desorption, the dipole-dipole interaction will decrease with a concomitant frequency shift.



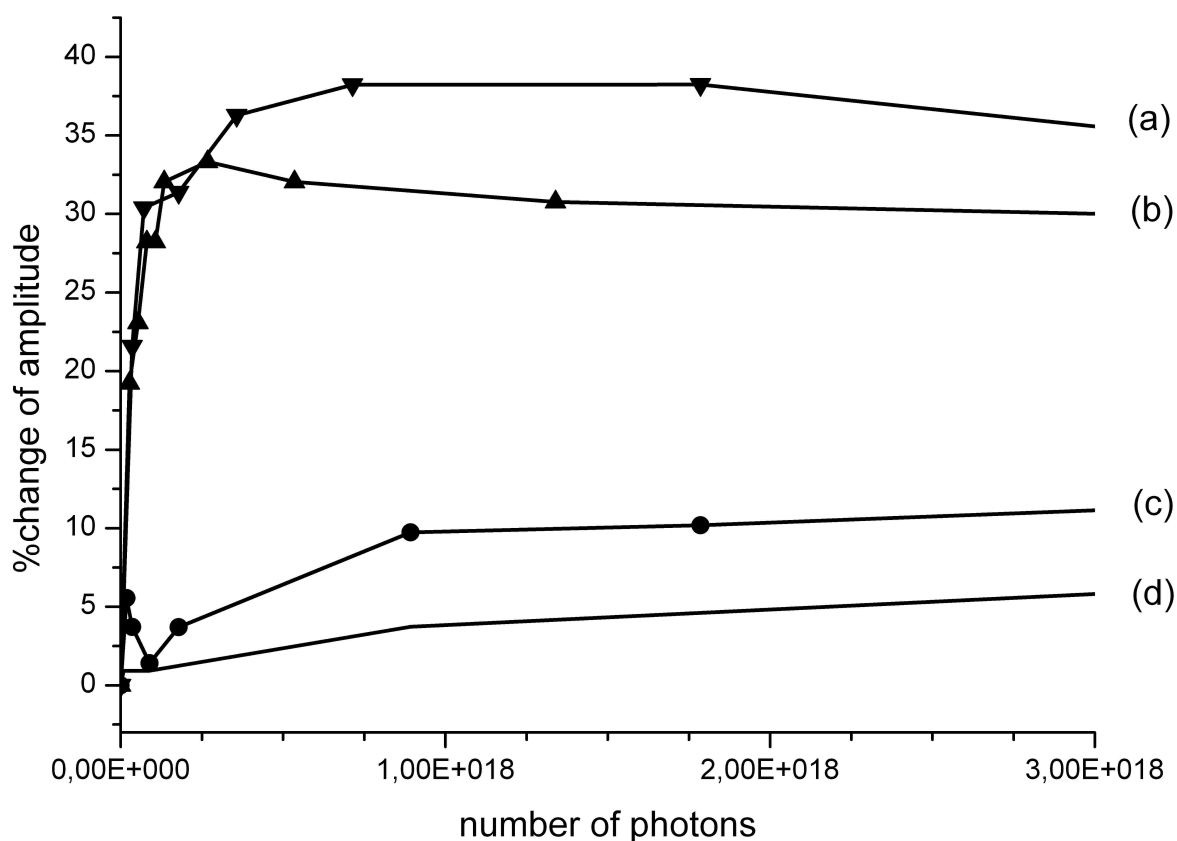


Figure 6.7: Relative change of FT-IR intensity of CO-stretching vibration (in percent) with respect to full saturation coverage of CO after Laser irradiation as a function of laser fluence. (a) 25.5 mJ/cm<sup>2</sup>, (b) 19.1 mJ/cm<sup>2</sup>, (c) 12.7 mJ/cm<sup>2</sup>, (d) 6.4 mJ/cm<sup>2</sup>

The data have been analyzed in more detail. The IR spectral shifts observed as a function of photons impinged onto the surface have been taken to calculate the coverage from a series of curves of IR-spectra taken as a function of coverage without laser irradiation. This analysis assumes a sticking probability of one and also assumes that the coverage changes are like under thermal equilibrium conditions. According to the tempering experiments in Fig. 5.28 this is not obvious but apparently during the laser experiments some diffusion processes occur. The molecules therefore are redistributed like under background dosing conditions and no metastable high density areas such as occurring in Fig. 5.28 are stable under laser irradiation. The frequency shifts are more sensitive to the coverage than the IR intensities which exhibit saturation of the intensity before reaching the full coverage.

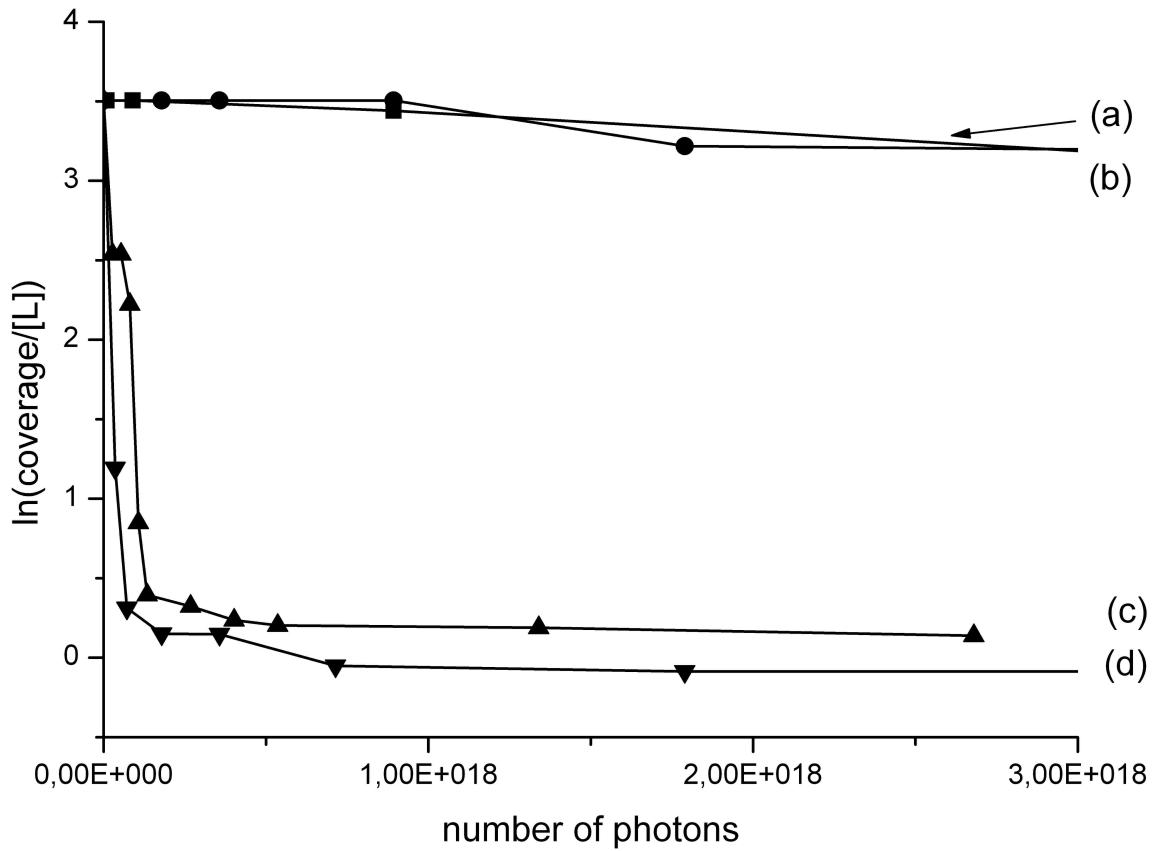


Figure 6.8: Logarithmic plot of the coverage of CO (extrapolated from frequency shifts of Figure 6.7) as a function of photons impinging onto the surface (nominal 0.1 nm platinum on alumina film at  $T=300$  K) (a)  $6.4 \text{ mJ/cm}^2$  per pulse, (b)  $12.7 \text{ mJ/cm}^2$  per pulse (c)  $19.1 \text{ mJ/cm}^2$  per pulse, (d)  $25.5 \text{ mJ/cm}^2$  per pulse

Figure 6.8 exhibits the plots of the logarithm of the coverages (given in Langmuir) as a function of photons impinging onto the surface. Assuming desorption processes with a first order kinetics the desorption cross section of the laser induced desorption may be extracted using the equation

$$\ln(N/N_o) = -\sigma n_{ph} \quad (1)$$

with  $N$  being the amount of molecules remaining on the surface,  $N_o$  being the initial coverage,  $\sigma$  being the desorption cross section and  $n_{ph}$  the number of photons impinging onto the surface shown in Figure 6.9. While at the two lower laser fluences desorption cross sections of  $(1.1 \pm 0.2) \times 10^{-19} \text{ cm}^2$  are obtained, the larger laser fluences have to be fitted with a biexponential. For the first laser pulses at high CO coverages one obtains a cross section of  $(2.3 \pm 0.2) \times 10^{-17} \text{ cm}^2$  for  $19.1 \text{ mJ cm}^{-2}$  per pulse and  $(4.4 \pm 0.2) \times 10^{-17} \text{ cm}^2$  for  $25.5 \text{ mJ cm}^{-2}$  per pulse while for prolonged laser exposure a

value similar to the lower laser fluence regime of  $(1.1 \pm 0.2) \times 10^{-19} \text{ cm}^2$  can be found. So the type of cross section found is also depend on the overall amount of molecules present at the surface. As both factors, the laser fluence and the CO coverage play a role a simple model consideration involving one or multiple photon processes is not sufficient to explain the findings. However, the high order change of the cross section might indicate that multiphoton processes might happen.

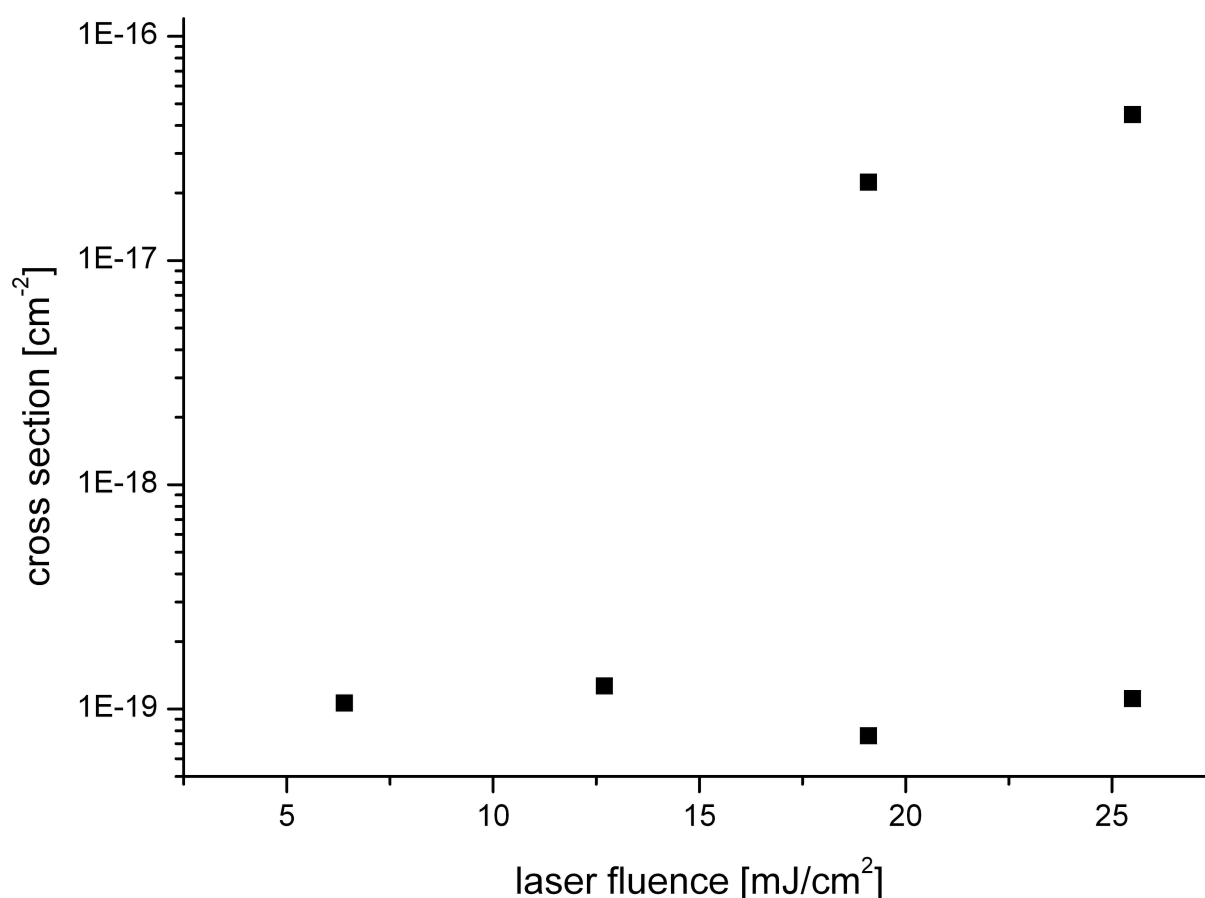


Figure 6.9: Desorption cross sections for CO as a function of laser fluence obtained from Figure 6.8

### 6.3 Adsorbate-induced roughening of Platinum nanoparticles after laser irradiation

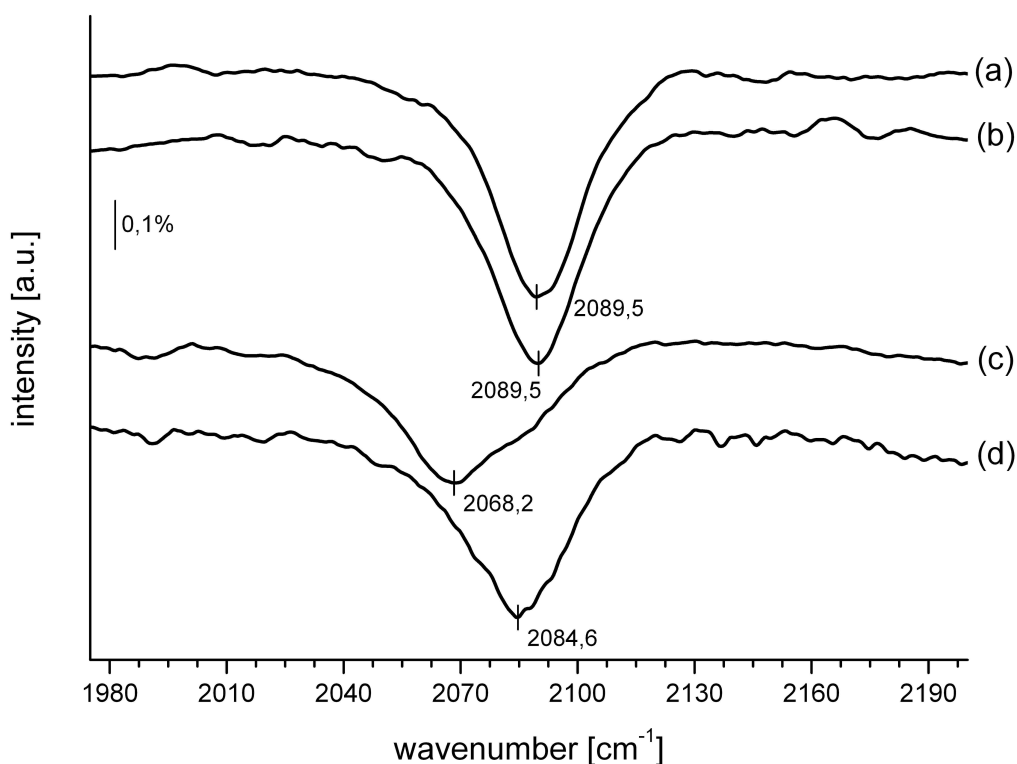


Figure 6.10: Nanosecond laser pulses were used to desorb CO adsorbed at 90K on 1Å Pt deposited at 300K on Al<sub>2</sub>O<sub>3</sub> at 355 nm, 19.1mJ cm<sup>-2</sup>. (a) 30L, (b) 2.6\*10<sup>16</sup> photons then 30L, (c) 30L, 2.6\*10<sup>16</sup> photons, (d) 30L, 2.6\*10<sup>16</sup> photons, 30L

There is a question about the source of the shift in the CO vibrational peak. Is it because of the laser induced CO desorption or might it be due to another reason like some platinum particles evaporate or diffuse during the laser irradiation. Such a process may reduce the amount of the CO molecules adsorbed on the particles which might lead to the CO vibrational peak shift. An experiment was implemented by irradiating the sample with the Nd:YAG, 19.1 mJ/cm<sup>2</sup> at 355nm laser first and then 30 L CO were re-adsorbed. The experiments in this section were done for samples of 1Å Platinum deposited at 300K onto alumina. Figure 6.10(a) shows a CO saturation coverage at 30L at 90K.

Figure 6.10(b) shows the FTIR spectrum of the adsorbed CO after the uncovered Pt nanoparticles has been exposed to laser radiation before dosing. It was interesting to note that the frequency of the CO vibrational peak has the same frequency of the CO vibrational peak that was directly adsorbed without laser irradiation. That means the laser doesn't modify the platinum nanoparticles without CO adsorbates present. As described in chapter 5, there are differences in the CO vibrational frequencies as a function of the deposited platinum thickness. So if some particles have been evaporated from the surface or particles have been destroyed otherwise, then some changes in the frequency of the CO vibrational peak should be noticeable.

Figure 6.10(c) shows the FTIR spectrum of the CO adsorption on 1 ÅPt deposited at 300K after irradiation with laser pulses of 19.1 mJ/cm<sup>2</sup> at 355nm with a total amount of  $2.6 \times 10^{16}$  photons. The frequency shift is clearly a result of the laser induced processes with CO present. After this experiment 30L CO were dosed again to the sample. FTIR measurement shown in Figure 6.10(d) exhibit that the frequency of the CO vibrational peak has been shifted compared to Figure 6.10(a). It is not the same as the frequency of the CO vibrational peak of CO dosed without laser irradiation. It may be speculated that a roughening occurs induced by CO adsorbed on the platinum nanoparticles with irradiation with the laser. Wille *et al.* (2004) has recognized the adsorbate induced roughening of nanosized palladium particles after coherent excitation. It was assumed that a multiple excitation of vibrational adsorbate modes followed by a channeling along chains of adsorbate solitons via dipole-dipole coupling and a subsequent trapping at certain aggregate sites are responsible. An efficient coupling to aggregate phonons then creates local hot spots sufficient to induce palladium-atom migration. A similar process apparently occurs for higher laser intensities in the present nanosecond laser experiments at Pt particles.

## 6.4 Laser induced CO desorption from different Pt thickness deposited at 300K

In chapter 4 the relation between the particle sizes to the amount of the platinum deposited was discussed. Figure 6.4 shows the laser induced CO desorption from 1 Å platinum for different laser fluences at  $\lambda = 355$  nm. By using the smallest intensity it was decided to check whether we can increase the laser induced laser desorption efficiency by decreasing or increasing the platinum particle size.

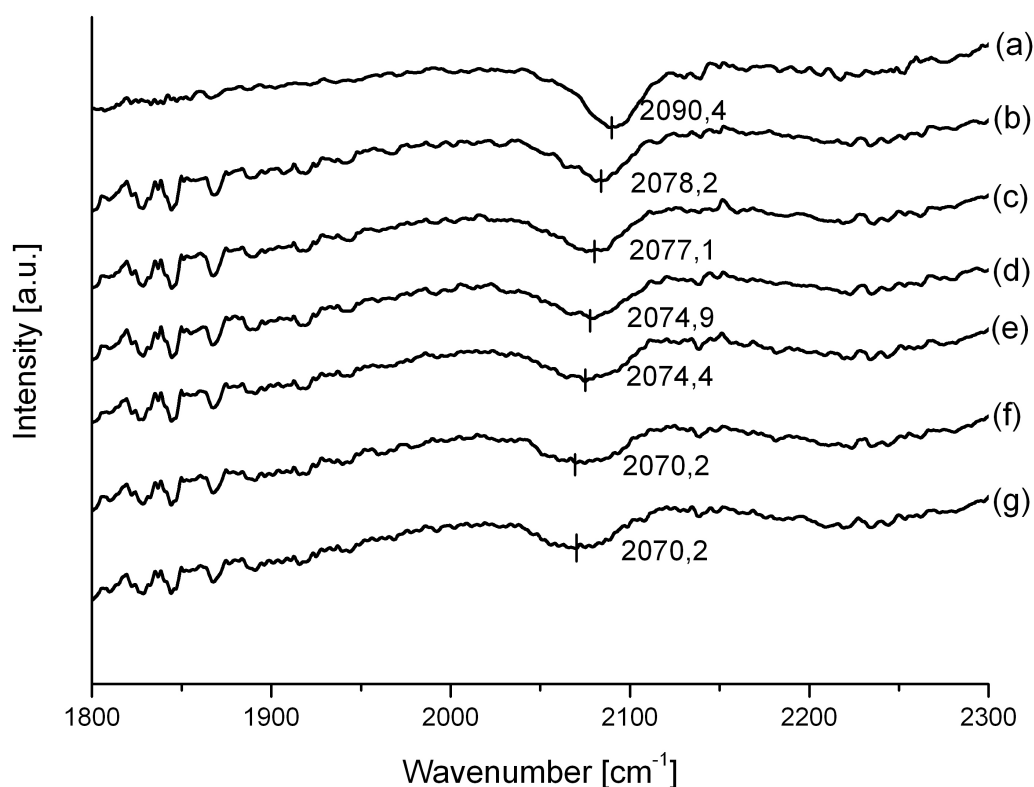


Figure 6.11: FTIR spectra of CO adsorbed at  $T=90$ K on  $0.5 \text{ \AA}$  Platinum deposited at 300K on alumina after laser irradiation with  $6.4 \text{ mJ/cm}^2$  (a)33L, (b) $8.92 \cdot 10^{18}$  Photons, (c) $1.78 \cdot 10^{19}$  Photons, (d) $2.67 \cdot 10^{19}$  Photons, (e) $3.57 \cdot 10^{19}$  Photons (f) $4.46 \cdot 10^{19}$  Photons (g) $7.14 \cdot 10^{19}$  Photons

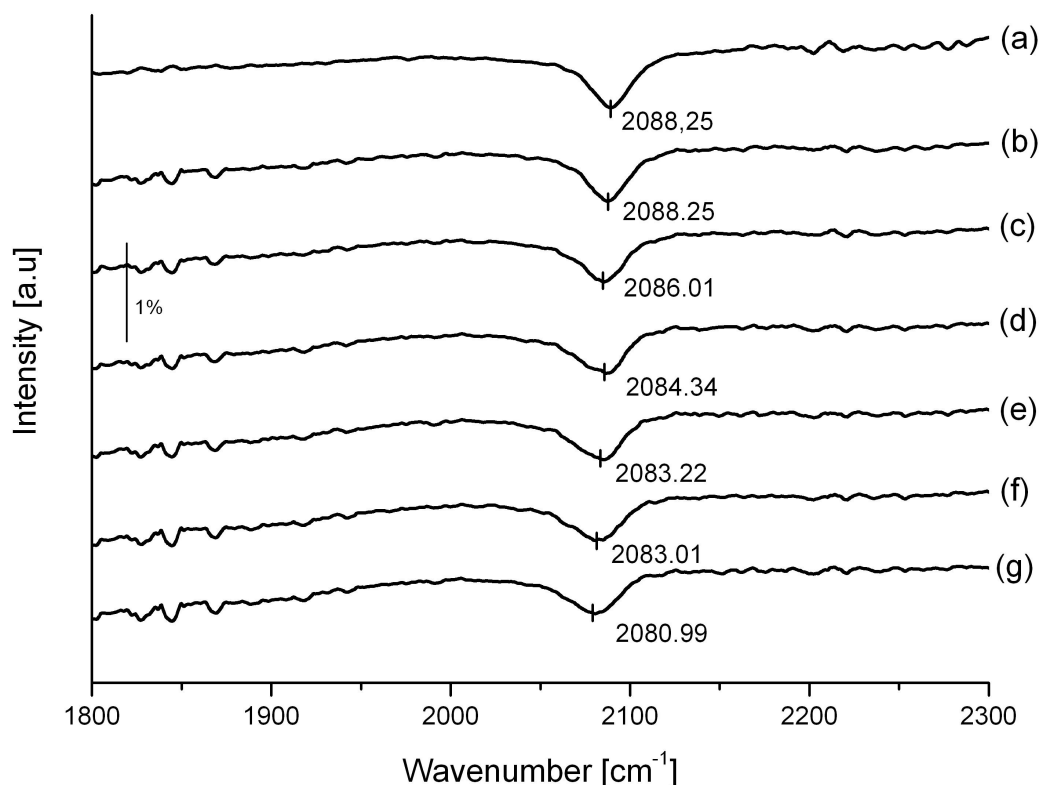


Figure 6.12: FTIR spectra of CO adsorbed at  $T=90\text{K}$  on  $1\text{\AA}$  Platinum deposited at  $300\text{K}$  on alumina after laser irradiation with  $6.4\text{ mJ/cm}^2$  (a)  $33\text{L}$ , (b)  $8.92 \cdot 10^{17}$  Photons, (c)  $8.92 \cdot 10^{18}$  Photons, (d)  $1.78 \cdot 10^{19}$  Photons, (e)  $2.67 \cdot 10^{19}$  Photons (f)  $4.46 \cdot 10^{19}$  Photons (g)  $7.14 \cdot 10^{19}$  Photons

So a series of experiments were done using  $6.4\text{ mJ/cm}^2$  at  $355\text{ nm}$  to study laser induced CO desorption from different Platinum thicknesses. A saturation coverage of  $33\text{L}$  CO was adsorbed. Then the sample was irradiated with laser light as described above. Figure 6.11, Figure 6.12, Figure 6.13, Figure 6.14 show FTIR spectra of CO adsorption coverage on  $0.5\text{\AA}$ ,  $1\text{\AA}$ ,  $2\text{\AA}$  and  $3\text{\AA}$  respectively Platinum deposited at  $300\text{K}$  on alumina after laser irradiation as a function of photons impinged.

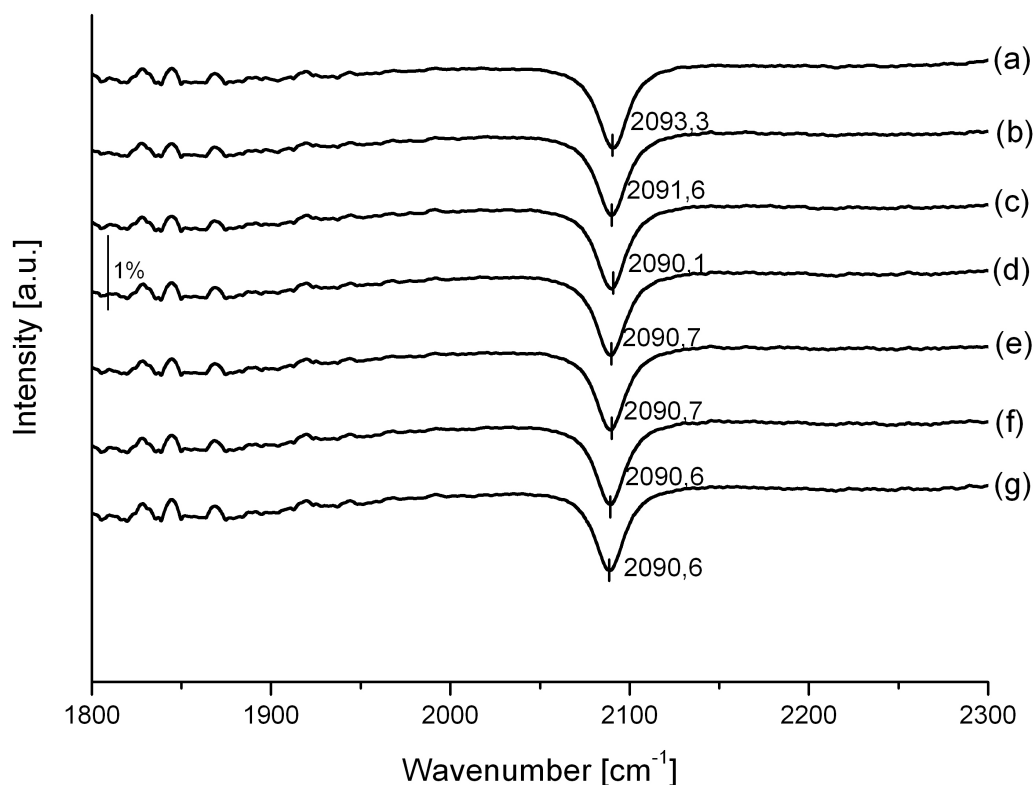


Figure 6.13: FTIR spectra of CO adsorbed at  $T=90\text{K}$  on  $2\text{\AA}$  Platinum deposited at  $300\text{K}$  on alumina after laser irradiation with  $6.4\text{ mJ/cm}^2$  (a)33L, (b) $8.92 \cdot 10^{18}$  Photon, (c) $1.78 \cdot 10^{19}$  Photons, (d) $2.67 \cdot 10^{19}$  Photons, (e) $3.57 \cdot 10^{19}$  Photons (f) $4.46 \cdot 10^{19}$  Photons (g) $7.14 \cdot 10^{19}$  Photons

Figure 6.11 shows a large shift in the CO frequency after laser irradiation. An experiment was done at  $0.27\text{ \AA}$  Pt which is far from the microbalance resolution. It was very noisy but it gave nearly the same results as  $0.5\text{ \AA}$  Pt. Figure 6.12 shows the decreasing frequency shift for  $1\text{ \AA}$  Pt with increasing laser exposure. The comparable frequency shift is very small for  $2\text{ \AA}$  and  $3\text{ \AA}$  Pt in Figure 6.13 and Figure 6.14. So Figure 6.15 shows the frequency shift for all Pt depositions as a function of photons impinged which makes the comparison between different thicknesses visible.



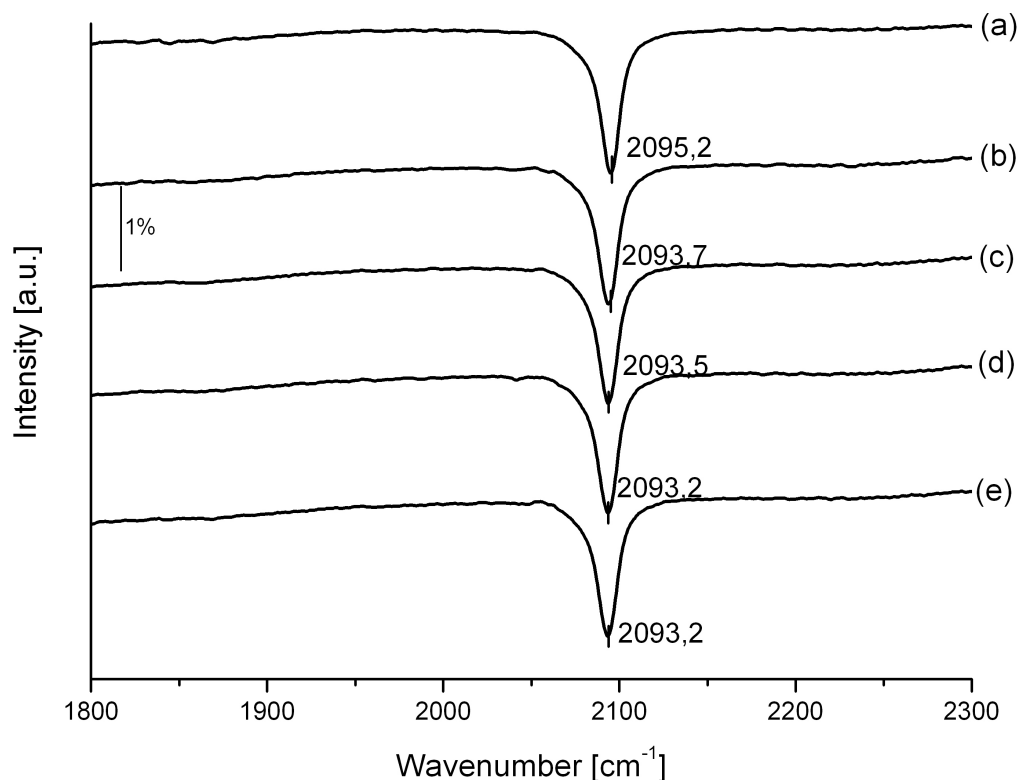


Figure 6.14: FTIR spectra of CO adsorbed at  $T=90\text{K}$  on  $3\text{\AA}$  Platinum deposited at  $300\text{K}$  on alumina after laser irradiation with  $6.4\text{ mJ/cm}^2$  (a)  $33\text{L}$ , (b)  $1.78 \cdot 10^{19}$  Photons, (c)  $2.67 \cdot 10^{19}$  Photons, (d)  $4.46 \cdot 10^{19}$  Photons (e)  $7.14 \cdot 10^{19}$  Photons

CO tempering experiment in Figure 5.33 and Figure 5.34 shows that the CO vibrational peak shift to  $2082.7\text{ cm}^{-1}$  when the sample is tempered to  $300\text{K}$ . While results of laser desorption experiment in Figure 6.13 shows that the CO vibrational peak shift to  $2090.6\text{ cm}^{-1}$ . This explains that there is no preferential desorption of low temperature adsorption species which mean that CO shuffles around quite a lot otherwise the peak should shift to  $2082.7\text{ cm}^{-1}$  with an increase in intensity.

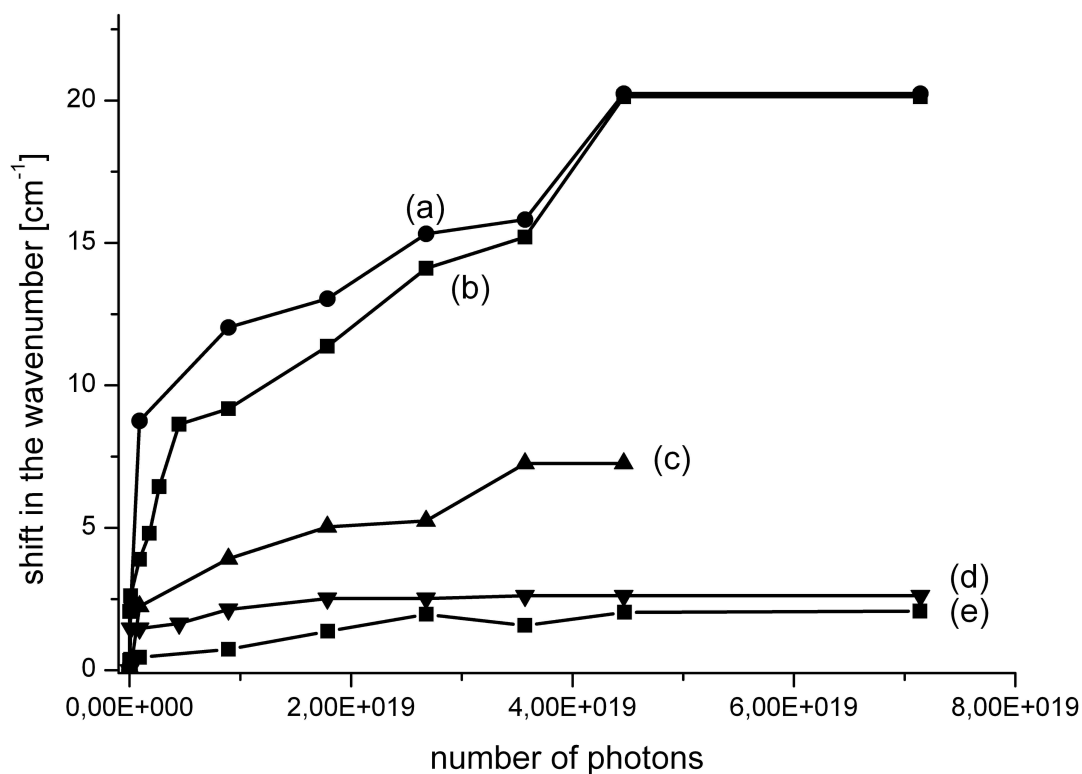


Figure 6.15: Nanosecond laser pulses at  $\lambda = 355 \text{ nm}$ ,  $6.4 \text{ mJ/cm}^2$ . CO adsorbed at  $T = 90 \text{ K}$  on Platinum deposited at  $300 \text{ K}$  on alumina. Frequency shifts of the CO stretching vibration as a function of number of photons impinged for (a)  $0.27 \text{ \AA}$ , (b)  $0.5 \text{ \AA}$ , (c)  $1 \text{ \AA}$ , (d)  $2 \text{ \AA}$ , (e)  $3 \text{ \AA}$  (overall amount of Pt deposited according to microbalance reading)

Figure 6.15 shows that at  $3 \text{ \AA}$  platinum thickness the frequency shift is at its minimum. The shift grows with decreasing thickness. At Pt coverages of  $0.5 \text{ \AA}$  and  $0.27 \text{ \AA}$  the frequency shifts are large and alike but the rise curve is higher for  $0.27 \text{ \AA}$ . The same procedure to calculate the desorption cross section as a function of laser fluence was used here to calculate the desorption cross section as a function of the thickness of the Platinum deposited on the alumina.

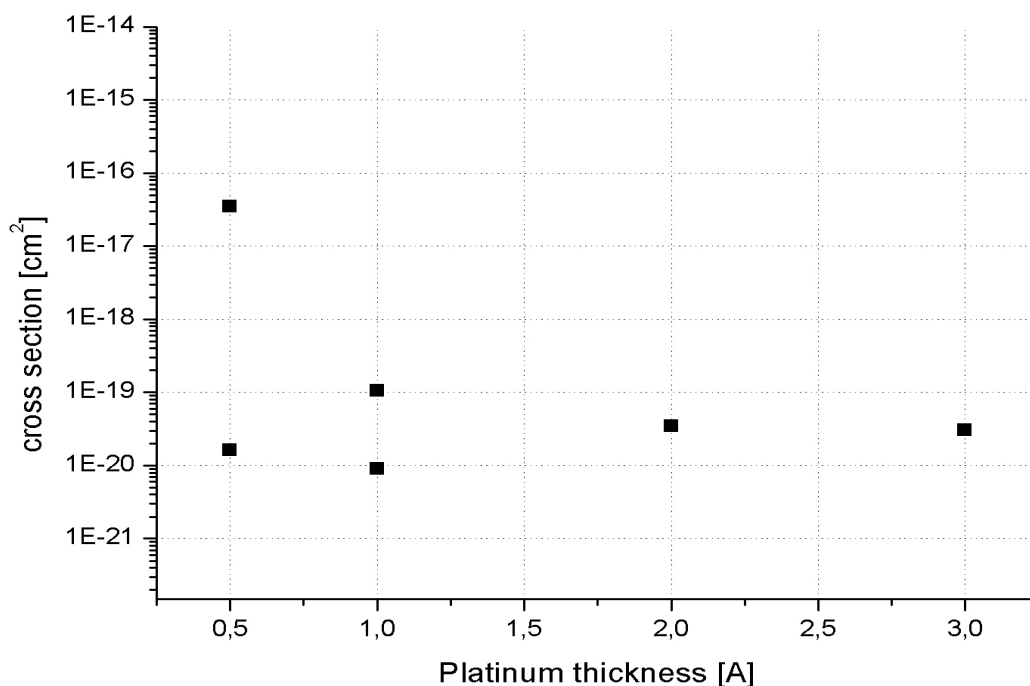


Figure 6.16: Desorption cross sections for CO as a function of Pt coverage/alumina (according to the reading of the quartz microbalance) for a laser fluence of  $6.4 \text{ mJ/cm}^2$  ( $\lambda=355 \text{ nm}$ ) as extracted from CO-stretching vibration data

The results of calculated cross sections are shown in Figure 6.16. At  $0.5 \text{ \AA}$  and  $1 \text{ \AA}$  their decay curves were fitted with a biexponential. For the first laser pulses the desorption cross section was  $3.48 \times 10^{-17} \text{ cm}^2$  while for later laser pulses a cross section of  $1.62 \times 10^{-20} \text{ cm}^2$  was found. For  $1 \text{ \AA}$   $\sigma$  was  $1.06 \times 10^{-19} \text{ cm}^2$  and later  $9.01 \times 10^{-21}$ , for  $2 \text{ \AA}$   $\sigma = 3.47 \times 10^{-20} \text{ cm}^2$  and for  $3 \text{ \AA}$   $\sigma = 3.07 \times 10^{-20} \text{ cm}^2$ . The cross section of  $0.27 \text{ \AA}$  was not calculated because of high signal to noise ratio of the FT-IR spectra. It is clear that at  $0.5 \text{ \AA}$  two different processes happened as the desorption cross section for the first pulses is several orders larger than for further pulses with  $\sigma$  being in the range of  $10^{-20} \text{ cm}^2$ . At  $1 \text{ \AA}$  the difference between the two values of the cross section is less than for  $0.5 \text{ \AA}$ . The desorption cross section decreases continuously with decreasing platinum thickness. For  $3 \text{ \AA}$  there are problems with the calibration curves for CO dosing explaining deviations from this trend as will be discussed further below.

## 6.5 Calculation of the error propagation in the desorption cross section

It was described how to calculate the desorption cross sections by relating the frequency of the CO stretching vibration to the CO adsorption coverage to estimate the amount of the CO which is still adsorbed on the Platinum nanoparticles. In order to better compare the laser induced CO desorption for different Pt particles, the same preparation was repeated several times. One of the error sources that might be presented is the quality of the alumina. Every time the alumina prepared was checked by LEED. Even good LEED patterns may differ in quality with respect to defect densities. Another error factor is the time of the platinum deposition for a specific amount and also the flux of the platinum evaporation. This factor is normally influenced by the changing of the head of the platinum rod on the evaporator which will induce changes in the distance between the platinum rod and the filament. This change will change the potential difference of the accelerated electrons from the filament to hit the rod to induce the evaporation. These factors could make slight changes in the Platinum nanoparticles on the alumina. The last error factor is the dosing of the CO. The adsorption coverage is done manually and because of the CO adsorption on the Platinum has a high nonlinearity, any small human error to open and to close the gas valve can accumulate errors in adsorption coverage and then this error will propagate to the calculation of the desorption cross section. Specially it was noted that the  $2\text{\AA}$  cross section is less than  $3\text{\AA}$  cross section. For larger particles the frequency shifts with CO coverage change are less pronounced so that the error is particularly large here. All these factors effect the desorption cross section. An example of the CO adsorption on  $1\text{\AA}$  Pt is shown in Figure 6.17. To calculate the error propagation numerically first derivations of the desorption cross section should be done as:

$$\ln(\theta) = \sigma n_{ph} \rightarrow \frac{\nabla \theta}{\theta} n_{ph} = \nabla \sigma$$

Two frequencies were chosen such that both graphs have the maximum error in the adsorption coverage. The frequencies are  $2088\text{ cm}^{-1}$  and  $2076\text{ cm}^{-1}$ , the error and the average was calculated as shown in the table below.

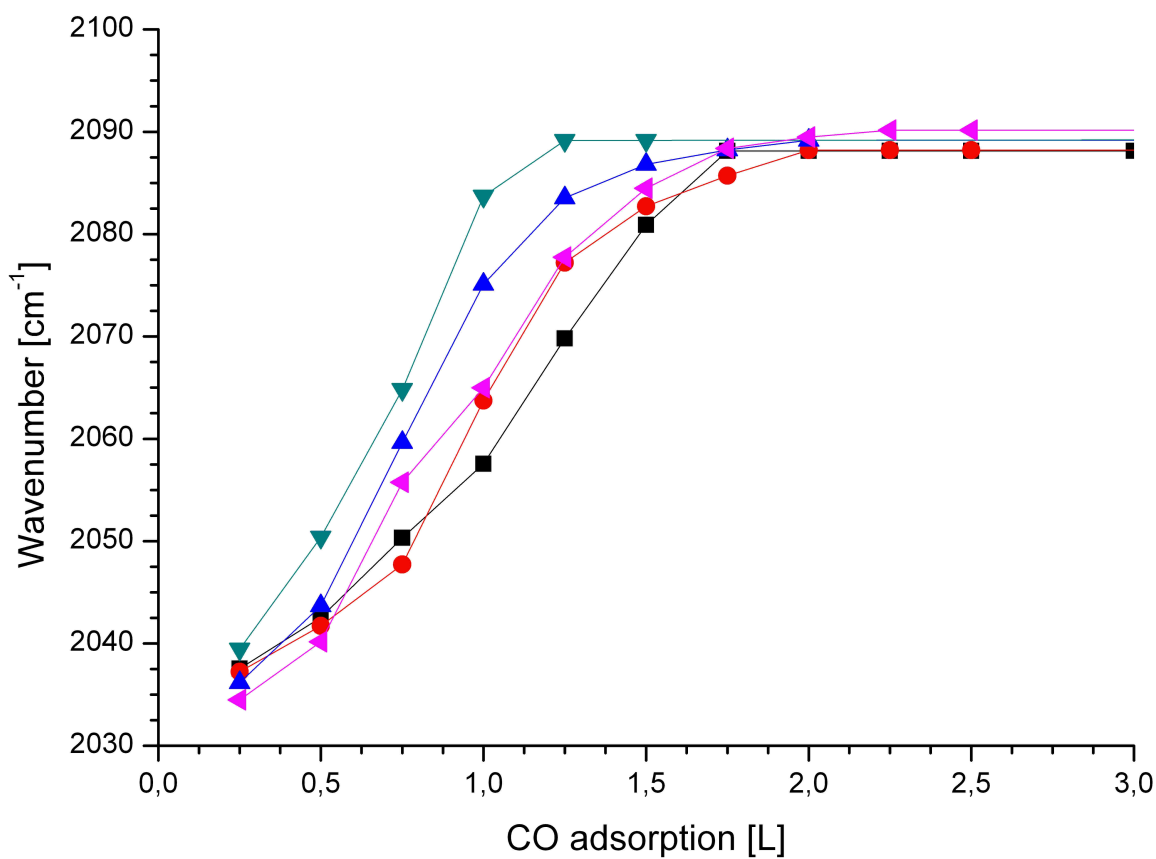


Figure 6.17: CO adsorption coverage on 1 Å Pt for different preparations

Frequency (cm <sup>-1</sup> )	CO coverage	Frequency (cm <sup>-1</sup> )	CO coverage
2075,0	1	2088,1	2
2075,0	1,368	2088,1	1,747
2075,0	1,1908	2088,1	1,747
2075,0	1,2081	2088,1	1,747
		2088,1	1,1939
Standard deviation	0,1506	Standard deviation	0,2966
average	1,191725	average	1,68698
Cross section error	12,64%	Cross section error	17,52%

The error propagation of the cross section is less than 20%. All the error sources that were discussed in this section are acceptable comparable to the few order increase of the cross section.

## 6.6 Discussion

The third harmonics at 355 nm of the Nd:YAG laser was used with different laser fluences 6.4 mJ cm<sup>-2</sup>, 12.7 mJ cm<sup>-2</sup>, 19.1 mJ cm<sup>-2</sup> and 25.5 mJ cm<sup>-2</sup> per pulse. In contrast to Pt(111), laser induced desorption of CO from a saturation coverage on platinum nanoparticles deposited on alumina was observed. The laser induced CO desorption depends on the CO coverage of the Platinum. It was recognized that no desorption occurs below a critical CO coverage. Depending on the laser fluence different critical CO coverages were observed. The critical CO coverage decreases as the laser fluence increases.

For elevated laser fluences (> 12.7 mJ cm<sup>-2</sup>) a sharp increase of the desorption efficiency by more than one order of magnitude was observed which could indicate multi photon processes. However, the large cross sections in our experiments are reminiscent to cross sections observed for laser induced desorption from oxide surfaces (Zimmermann and Ho 1995). Thus it may not fully be ruled out that spill over from CO molecules adsorbed at the platinum nanoparticles to the alumina support may occur followed by desorption.

Laser induced CO desorption experiments as a function of platinum thickness were done. The results show that the smaller the particles are the more efficient the CO desorption is at certain laser fluences to occur. It was observed that the cross sections decrease as the platinum thickness increases. At 0.5 Å platinum exhibits sharp changes in the cross sections. In TPD spectra loosely bound species are observed which may be responsible for an efficient desorption.

Adsorbate induced roughening experiments to observe particle destruction for dense adsorbate coverage was observed similar to the coherent experiments of Wille *et al.* (2004) on CO at palladium on alumina. One possible interpretation is that this is caused by energy pooling via dipole-dipole coupling in excited molecules at hot particle spots particularly at edges and kinks. The excited CO molecules gained their energy through short electronic excitation. This fact was supported by the finding that the laser desorption is only efficient at certain adsorbate coverages which depends on the laser fluence. The same idea was discussed in the quantum state resolved mapping of the energy partitioning in desorbing NO molecules from palladium particles reported by Kampling *et al.* (2002) pointing towards a mechanism which is governed by local effects such as would be found for lower coordinated metal particle sites at edges and kinks.

## References

Al-Shamery, K.; Beauport, I.; Freund, H. J. & Zacharias, H. (1994), 'UV laser-induced desorption of CO from Cr<sub>2</sub>O<sub>3</sub>(111). A fully quantum state resolved mapping of the desorbing species', *Chemical Physics Letters* **222**(1-2), 107 - 112.

Alvey, M. D.; Dresser, M. J. & Yates, J. T. (1986), 'Metastable angular distributions from electron-stimulated desorption', *Phys. Rev. Lett.* **56**(4), 367.

Antoniewicz, P. R. (1980), 'Model for electron- and photon-stimulated desorption', *Phys. Rev. B* **21**(9), 3811.

Asscher, M.; Zimmermann, F. M.; Springsteen, L. L.; Houston, P. L. & Ho, W. (1992), 'Translational and internal energy distributions of CO photochemically desorbed from oxidized Ni(111)', *The Journal of Chemical Physics* **96**(6), 4808-4811.

Auer, S.; Feulner, P. & Menzel, D. (1987), 'Comparison of neutral to ionic photodesorption in the valence region: CO/Ru(001)', *Phys. Rev. B* **35**(14), 7752.

Avery, N. R. (1981), 'Electron energy loss spectroscopic study of CO on Pt(111)', *The Journal of Chemical Physics* **74**(7), 4202-4203.

Avouris, P. & Walkup, R. E. (1989), 'Fundamental Mechanisms of Desorption and Fragmentation Induced by Electronic Transitions at Surfaces', *Annual Review of Physical Chemistry* **40**(1), 173-206.

Baro, A. M. & Ibach, H. (1979), 'New study of CO adsorption at low temperature (90 K) on Pt (111) by EELS', *The Journal of Chemical Physics* **71**(12), 4812-4816.

- Bertrams, T.; Winkelmann, F.; Uttich, T.; Freund, H. J. & Neddermeyer, H. (1995), 'Structural characterization of a model catalyst: Pt/Al<sub>2</sub>O<sub>3</sub>/NiAl(110)', *Surface Science* **331-333**(Part 2), 1515-1519.
- Bradshaw, A. & Hoffmann, F. (1976), "*J. Catalysis* **44**, 328.
- Burns, A. (1993), 'Quantum-resolved angular distributions of neutral products in electron-stimulated processes: desorption of CO\* from Pt(111)', *Surface Science* **280**(3), 349 - 358.
- Burns, A. R.; Stechel, E. B. & Jennison, D. R. (1987), 'Desorption by electronically stimulated adsorbate rotation', *Phys. Rev. Lett.* **58**(3), 250.
- Bäumer, M.; Cappus, D.; Kühlenbeck, H.; Freund, H.-J.; Wilhelmi, G.; Brodde, A. & Neddermeyer, H. (1991), 'The structure of thin NiO(100) films grown on Ni(100) as determined by low-energy-electron diffraction and scanning tunneling microscopy', *Surface Science* **253**(1-3), 116-128.
- Campbell, C. T. (1997), 'Ultrathin metal films and particles on oxide surfaces: structural, electronic and chemisorptive properties', *Surface Science Reports* **27**(1-3), 1-111.
- Campbell, C. T. & Ludviksson, A. (1994), 'Model for the growth and reactivity of metal films on oxide surfaces: Cu on ZnO(0001-bar)--O', *J. Vac. Sci. Technol. A*, AVS, Orlando, Florida (USA), pp. 1825-1831.
- Cappus, D.; Xu, C.; Ehrlich, D.; Dillmann, B.; Ventrice, C. A.; Al Shamery, K.; Kühlenbeck, H. & Freund, H. J. (1993), 'Hydroxyl groups on oxide surfaces: NiO(100), NiO(111) and Cr<sub>2</sub>O<sub>3</sub>(111)', *Chemical Physics* **177**(2), 533-546.
- Cassuto, A. & King, D. A. (1981), 'Rate expressions for adsorption and desorption kinetics with precursor states and lateral interactions', *Surface Science* **102**(2-3), 388 - 404.
- Cavanagh, R. R.; King, D. S.; Stephenson, J. C. & Heinz, T. F. (1993), 'Dynamics of nonthermal reactions: femtosecond surface chemistry', *The Journal of Physical Chemistry* **97**(4), 786-798.



Chatain, D.; Coudurier, L. & Eustathopoulos, N. (1988), 'Wetting and interfacial bonding in ionocovalent oxide-liquid metal systems', *Rev. Phys. Appl. (Paris)* **23**(6), 1055-1064.

Chen, J.; Crowell, J.; Yates, J. & Jr. (1987), 'Ni cluster chemistry on Al<sub>2</sub>O<sub>3</sub>-A vibrational eels study using chemisorbed CO on a model catalyst: Ni/Al<sub>2</sub>O<sub>3</sub>/Al(111)', *Surface Science* **187**(2-3), 243 - 264.

Chen, J. G.; Crowell, J. E. & Yates, J. T. (1987), 'Differentiation of single versus multiple vibrational excitation processes on surfaces: An electron-energy-loss spectroscopy investigation of the Al<sub>2</sub>O<sub>3</sub> vibrational modes', *Phys. Rev. B* **35**(10), 5299.

ChenHEN, P.; Colaianni, M. & Yates, J. (1990), 'Effect of complete oxidation on the vibrational properties of aluminium-oxide thin-films an electron energy loss spectroscopy study', *Physical Review* **41**(12), 8025-8032.

Chen, P. & Goodman, D. (1994), 'Epitaxial-growth of ultrathin Al<sub>2</sub>O<sub>3</sub> films on TA(110)', *Surface Science* **312**(3), L767-L773.

Chiang, T. C. (2000), 'Photoemission studies of quantum well states in thin films', *Surface Science Reports* **39**(7-8), 181 - 235.

Chuang, T. (1986), 'Laser-induced molecular processes on surfaces', *Surface Science* **178**(1-3), 763 - 786.

Collins, D. & Spicer, W. (1977), 'The adsorption of CO, O<sub>2</sub>, and H<sub>2</sub> on Pt: I. Thermal desorption spectroscopy studies', *Surface Science* **69**(1), 85 - 113.

Crossley, A. & King, D. A. (1977), 'Infrared spectra for co isotopes chemisorbed on Pt (111): Evidence for strong adsorbate coupling interactions', *Surface Science* **68**, 528 - 538.

- Crowell, J.; Chen, J. & Jr., J. Y. (1986), 'Surface sensitive spectroscopic study of the interaction of oxygen with Al(111) - low temperature chemisorption and oxidation', *Surface Science* **165**(1), 37 - 64.
- Davisson, C. & Germer, L. H. (1927), 'Diffraction of Electrons by a Crystal of Nickel', *Phys. Rev.* **30**(6), 705.
- Diebold, U.; Pan, J.-M. & Madey, T. E. (1995), 'Ultrathin metal film growth on TiO<sub>2</sub>(110): an overview', *Surface Science* **331-333**(Part 2), 845-854.
- Doychak, J.; Smialek, J. & Mitchell, T. (1989), 'Transient oxidation of Single-Crystal  $\hat{I}^2$ -NiAl', *Metallurgical and Materials Transactions A* **20**(3), 499-518.
- Ernst, K. H.; Ludviksson, A.; Zhang, R.; Yoshihara, J. & Campbell, C. T. (1993), 'Growth model for metal films on oxide surfaces: Cu on ZnO(0001)-O', *Phys. Rev. B* **47**(20), 13782.
- Erskine, J. L. & Strong, R. L. (1982), 'High-resolution electron-energy-loss-spectroscopy study of the oxidation of Al(111)', *Phys. Rev. B* **25**(8), 5547.
- Ertl, G.; Neumann, M. & Streit, K. M. (1977), 'Chemisorption of CO on the Pt(111) surface', *Surface Science* **64**(2), 393 - 410.
- Fair, J. & Madix, R. J. (1980), 'Low and high coverage determinations of the rate of carbon monoxide adsorption and desorption from Pt(110)', *The Journal of Chemical Physics* **73**(7), 3480-3485.
- Falconer, J. L. & Schwarz, J. A. (1983), 'Temperature-Programmed Desorption and Reaction: Applications to Supported Catalysts', *Catalysis Reviews: Science and Engineering* **25**(2), 141-227.
- Froitzheim, H.; Hopster, H.; Ibach, H. & Lehwald, S. (1977), 'Adsorption sites of CO on Pt (111)', *Applied Physics A: Materials Science & Processing* **13**(2), 147-151.

- Fukutani, K.; Song, M. & Murata, Y. (1993), 'Ultraviolet-laser-induced desorption of CO and NO from Pt surfaces', *Faraday Discussions* **96**, 105-116.
- Fukutani, K.; Song, M.-B. & Murata, Y. (1995), 'Photodesorption of CO and CO<sup>+</sup> from Pt(111): Mechanism and site specificity', *The Journal of Chemical Physics* **103**(6), 2221-2228.
- Giorgio, S.; Graoui, H.; Chapon, C. & Henry, C. (1997), 'Pd particles supported on ZnO (001) epitaxial thin films, evolution during HRTEM observations', *Materials Science and Engineering A-Structural Materials Properties Microstructure and Processing* **229**(1-2), 169-173.
- Guillamet, R.; Lenglet, M. & Adam, F. (1992), 'Reflectance Spectroscopy of Oxides Films Alpha-CR<sub>2</sub>O<sub>3</sub> and Alpha Fe<sub>2</sub>O<sub>3</sub> on Iron', *Solid State Communications* **81**(8), 633-637.
- Guo, X.; Yoshinobu, J. & John T. Yates, J. (1990), 'Photon-induced desorption of CO chemisorbed on the oxidized Ni(111) surface', *The Journal of Chemical Physics* **92**(7), 4320-4326.
- Hasselbrink, E. (1991), 'Photostimulated chemistry at the metal-adsorbate interface', *Applied Physics A: Materials Science & Processing* **53**(5), 403-409.
- Hayden, B.; Kretschmar, K. & Bradshaw, A. (1983), 'A TPD and IR study of co-adsorption of NO and oxygen on Ru(001)', *Surface Science* **125**(2), 366 - 376.
- Hayden, B.; Kretschmar, K.; Bradshaw, A. & Greenler, R. (1985), 'An infrared study of the adsorption of CO on a stepped platinum surface', *Surface Science* **149**(2-3), 394 - 406.
- Helmut Günzler, H.-U. G. (2002), *IR spectroscopy: an introduction*, Wiley-VCH, 2002.
- Henderson, M. A.; Szabo, A. & J. T. Yates, J. (1989), 'The structure of CO on the Pt(112) stepped surface---a sensitive view of bonding configurations using electron stimulated desorption', *The Journal of Chemical Physics* **91**(11), 7245-7254.

- Henderson, M. A.; Szabó, A. & Yates, J. T. (1990), 'Direct observation of adsorbate-adsorbate repulsions along a one-dimensional array: CO on the steps of Pt(112)', *Chemical Physics Letters* **168**(1), 51 - 55.
- Henry, C. R. (1998), 'Surface studies of supported model catalysts', *Surface Science Reports* **31**(7-8), 231-325.
- Heyden, B. & Bradshaw, A. (1983), 'The adsorption of CO on Pt(111) studied by infrared reflection--Absorption spectroscopy', *Surface Science* **125**(3), 787 - 802.
- Heyden, B. & Bradshaw, A. (1983), 'The adsorption of CO on Pt(111) studied by infrared reflection--Absorption spectroscopy', *Surface Science* **125**(3), 787-802.
- Ho, W. (1988), 'Mechanisms for Photodissociation and Photodesorption of Molecules Adsorbed on Solid Surfaces', *Comments on Cond. Matter Phys.* **13**, 293-327.
- Hoffmann, F. M. (1983), 'Infrared reflection-absorption spectroscopy of adsorbed molecules', *Surface Science Reports* **3**(2-3), 107 - 107.
- Hopster, H. & Ibach, H. (1978), 'Adsorption of CO on Pt(111) and Pt 6(111) × (111) studied by high resolution electron energy loss spectroscopy and thermal desorption spectroscopy', *Surface Science* **77**(1), 109 - 117.
- Isern, H. & Castro, G. (1989), 'The initial interaction of oxygen with a NiAl(110) single crystal: A LEED and AES study', *Surface Science* **211-212**, 865-871.
- Iwasawa, Y.; Mason, R.; Textor, M. & Somorjai, G. A. (1976), 'The reactions of carbon monoxide at coordinatively unsaturated sites on a platinum surface', *Chemical Physics Letters* **44**(3), 468 - 470.

Jacobs, J.-P.; Reijne, S.; Elfrink, R. J. M.; Mikhailov, S. N.; Brongersma, H. H. & Wuttig, M. (1994), 'Quantification of the composition of alloy and oxide surfaces using low-energy ion scattering', *The 40th National Symposium of the American Vacuum Society* **12**(4), AVS, 2308-2313.

Jaeger, R.; Kuhlenbeck, H.; Freund, H.-J.; Wuttig, M.; Hoffmann, W.; Franchy, R. & Ibach, H. (1991), 'Formation of a well-ordered aluminium oxide overlayer by oxidation of NiAl(110)', *Surface Science* **259**(3), 235-252.

Jaeger, R. M.; Libuda, J.; Bäumer, M.; Homann, K.; Kuhlenbeck, H. & Freund, H. J. (1993), 'Vibrational structure of excited states of molecules on oxide surfaces', *Journal of Electron Spectroscopy and Related Phenomena* **64-65**, 217-225.

Kamat, P. V. (2007), 'Meeting the Clean Energy Demand: Nanostructure Architectures for Solar Energy Conversion', *The Journal of Physical Chemistry C* **111**(7), 2834-2860.

Kamplung, M.; Al-Shamery, K.; Freund, H.-J.; Wilde, M.; Fukutani, K. & Murata, Y. (2002), 'Surface photochemistry on confined systems: UV-laser-induced photodesorption of NO from Pd-nanostructures on Al<sub>2</sub>O<sub>3</sub>', *Physical Chemistry Chemical Physics* **4**, 2629-2637.

King, D. A. (1975), 'Thermal desorption from metal surfaces: A review', *Surface Science* **47**(1), 384 - 402.

Kiskinova, M.; Szab, A. & Jr., J. Y. (1988), 'Compressed CO overlayers on Pt(111) -- Evidence for tilted CO species at high coverages by digital ESDIAD', *Surface Science* **205**(1-2), 215 - 229.

Klimenkov, M.; Kuhlenbeck, H. & Nepijko, S. (2003), 'Growth mode of Pt clusters deposited on [gamma]-Al<sub>2</sub>O<sub>3</sub>(1 1 1)/NiAl(1 1 0): a TEM study', *Surface Science* **539**(1-3), 31-36.

Klimenkov, M.; Nepijko, S.; Kuhlenbeck, H. & Freund, H. J. (1997), 'Transmission electron microscopic investigation of an ordered Al<sub>2</sub>O<sub>3</sub> film on NiAl(110)', *Surface Science* **385**(1), 66-76.

Krebs, H. J. & Lüth, H. (1977), 'Evidence for two different adsorption sites of CO on Pt(111) from infrared reflection spectroscopy', *Applied Physics A: Materials Science & Processing* **14**, 337-342.

Kronauer, P. & Menzel, D. (1972), 'Adsorption-Desorption Phenomena', *Academic, New York*, 313.

Libuda, J.; Baumer, M. & Freund, H.-J. (1994), 'Structural characterization of platinum deposits supported on ordered alumina films', *The 40th National Symposium of the American Vacuum Society* **12**(4), AVS, 2259-2264.

Libuda, J.; Winkelmann, F.; Bäumer, M.; Freund, H.-J.; Bertrams, T.; Neddermeyer, H. & Müller, K. (1994), 'Structure and defects of an ordered alumina film on NiAl(110)', *Surface Science* **318**(1-2), 61-73.

Luo, J.; Tobin, R.; Lambert, D. K.; Fisher, G. B. & DiMaggio, C. L. (1992), 'CO adsorption site occupation on Pt(335): a quantitative investigation using TPD and EELS', *Surface Science* **274**(1), 53 - 62.

M. Bäumer, J. Libuda, H.-J. F. Lambert, R. & Pacchioni, G., ed. (1997), *Metal Deposits on Thin Well Ordered Oxide Films: Morphology, Adsorption and Reactivity*, Nato-Advanced Study Institute, NATO ASI Ser. Vol. E, Kluwer Acad. Publ, 61 - 104.

Magkoev, T.; Song, M.; Fukutani, K. & Murata, Y. (1995), 'Rais Observation of Photoinduced Dissociation of NO on Ni(111)', *Surface Science* **330**(2), L669-L672.

McCabe, R. & Schmidt, L. (1977), 'Binding states of CO on single crystal planes of Pt', *Surface Science* **66**(1), 101 - 124.

McClellan, M. R.; Gland, J. L. & McFeeley, F. (1981), 'Carbon monoxide adsorption on the kinked Pt(321) surface', *Surface Science* **112**(1-2), 63 - 77.

Menzel, D. & Gomer, R. (1964), 'Desorption from Metal Surfaces by Low-Energy Electrons', *The Journal of Chemical Physics* **41**(11), 3311-3328.

Niemantsverdriet, D. J. W. Dyllick-Brenzinger, D. C. & Sora, K., ed. (1993), *Spectroscopy in Catalysis: an introduction*, VCH Verlagsgesellschaft, Weinheim (Federal Republic of Germany) VCH Publishers, New York, NY (USA).

Norton, P.; Goodale, J. & Selkirk, E. (1979), 'Adsorption of CO on Pt(111) studied by photoemission, thermal desorption spectroscopy and high resolution dynamic measurements of work function', *Surface Science* **83**(1), 189 - 227.

Okoroanyanwu, U.; Kunze, P.; Al-Shamery, K. H.; Romero, J. & Bernard, J. (2002), Impact of photo-induced species in O<sub>2</sub> containing gases on lithographic patterning at 193-nm wavelength, in 'Proc. SPIE', SPIE, Santa Clara, CA, USA, pp. 746-764.

Overbury, S. H.; Bertrand, P. A. & Somorjai, G. A. (1975), 'Surface composition of binary systems. Prediction of surface phase diagrams of solid solutions', *Chemical Reviews* **75**(5), 547-560.

Pan, F.; Zhang, J.; Zhang, W.; Wang, T. & Cai, C. (2007), 'Enhanced photocatalytic activity of Ag microgrid connected TiO<sub>2</sub> nanocrystalline films', *Appl. Phys. Lett.* **90**(12), 122114-3.

Peden, C. H. F.; Kidd, K. B. & Shinn, N. D. (1991), 'Metal/metal-oxide interfaces: A surface science approach to the study of adhesion', *J. Vac. Sci. Technol. A* **9**(3), 1518-1524.

Peremans, A.; Fukutani, K.; Mase, K. & Murata, Y. (1993), 'CO and CO<sup>+</sup> photodesorption from Pt(001) at 193 nm', *Phys. Rev. B* **47**(7), 4135.

- Peremans, A.; Fukutani, K.; Mase, K. & Murata, Y. (1993), 'UV photodesorption of CO from Pt(001) at 193 nm investigated by state-selective detection', *Surface Science* **283**(1-3), 189 - 194.
- Peremans, A.; Fukutani, K.; Mase, K. & Murata, Y. (1993), 'UV photodesorption of CO from Pt(001) at 193 nm investigated by state-selective detection', *Surface Science* **283**(1-3), 189-194.
- Persaud, R. & Madey, T. E. (1997), Chapter 11 Growth, structure and reactivity of ultrathin metal films on TiO<sub>2</sub> surfaces, *in* Ph.D. (Rand) Sc.D. (East Anglia) F.R.S. D.A. King, B.Sc. & Ph.D. D.Sc. (Warwick) D.P. Woodruff, B.Sc. (Bristol), ed., 'Growth and Properties of Ultrathin Epitaxial Layers', Elsevier, , pp. 407-447.
- Prybyla, J. A.; Tom, H. W. K. & Aumiller, G. D. (1992), 'Femtosecond time-resolved surface reaction: Desorption of Co from Cu(111) in <math>\approx 325\text{ fsec}</math>', *Phys. Rev. Lett.* **68**(4), 503.
- Redhead, P. (1964), 'Interaction of Slow Electron of Slow Electrons with Chemisorbed Oxygen', *Can. J. Phys./Rev. can. Phys.* **42**(5), 886-905.
- Redhead, P. (1964), 'Interaction of slow electrons with chemisorbed Oxygen', *Can. J. Phys./Rev. can. phys.* **42**(5), 886-905.
- Rubahn, H.-G. (1999), *Laser Applications in Surface Science and Technology*, Wiley-Blackwell.
- Shigeishi, R. A. & King, D. A. (1976), 'Chemisorption of carbon monoxide on platinum 111: Reflection-absorption infrared spectroscopy', *Surface Science* **58**(2), 379 - 396.
- Smith, D. L. (1995), *Thin-Film Deposition: Principles and Practice*, McGraw-Hill Companies.
- Steininger, H.; Lehwald, S. & Ibach, H. (1982), 'On the adsorption of CO on Pt(111)', *Surface Science* **123**(2-3), 264 - 282.
- Strong, R. L.; Firey, B.; de Wette, F. W. & Erskine, J. L. (1982), 'Surface-site determination using electron-energy-loss spectroscopy and lattice-dynamical models', *Phys. Rev. B* **26**(6), 3483--.



Tüshaus, M.; Schweizer, E.; Hollins, P. & Bradshaw, A. M. (1987), 'Yet another vibrational study of the adsorption system Pt(111)-CO', *Journal of Electron Spectroscopy and Related Phenomena* **44**(1), 305 - 316.

Venables, J. A.; Spiller, G. D. T. & Hanbucken, M. (1984), 'Nucleation and growth of thin films', *Reports on Progress in Physics* **47**(4), 399-459.

Watanabe, K.; Matsumoto, Y.; Kampling, M.; Al-Shamery, K. & Freund, H.-J. (1999), 'Photochemistry of Methane on Pd/Al<sub>2</sub>O<sub>3</sub> Model Catalysts: Control of Photochemistry on Transition Metal Surfaces', *Angewandte Chemie International Edition* **38**(15), 2192-2194.

Wille, A.; Buchwald, R. & Al-Shamery, K. (2004), 'Adsorbate-induced roughening of nanosized palladium particles after coherent laser excitation', *Applied Physics A-Materials Science & Processing* **78**(2), 205-211.

Wille, A.; Buchwald, R. & Al-Shamery, K. (2004), 'Adsorbate-induced roughening of nanosized palladium particles after coherent laser excitation', *Applied Physics A: Materials Science & Processing* **78**(2), 205-211.

Wille, A.; Haubitz, S. & Al-Shamery, K. (2003), 'Laser induced adsorption site changes of CO adsorbed at nanoparticulate palladium aggregates on an alumina support driven by local adsorbate density fluctuations', *Chemical Physics Letters* **367**(5-6), 609-616.

Winkelmann, F.; Wohlrab, S.; Libuda, J.; Bäumer, M.; Cappus, D.; Menges, M.; Al-Shamery, K.; Kühlenbeck, H. & Freund, H.-J. (1994), 'Adsorption on oxide surfaces: structure and dynamics', *Surface Science* **307-309**(Part 2), 1148-1160.

Xu, J.; Henriksen, P. N. & Yates, J. T. (1994), 'Reflection Infrared Study of the Xe-CO Interaction on Pt(335): A New Method for Site Assignment of Chemisorbed Species', *Langmuir* **10**(10), 3663-3667.

Xu, J. & Yates, J. T. (1995), 'Terrace width effect on adsorbate vibrations: a comparison of Pt(335) and Pt(112) for chemisorption of CO', *Surface Science* **327**(3), 193 - 201.

Xu, X. & Goodman, D. W. (1992), 'Metal deposition onto oxides: An unusual low initial sticking probability for copper on SiO<sub>2</sub>', *Applied Physics Letters* **61**(15), 1799-1801.

Yoshinobu, J.; Ballinger, T.; Xu, Z.; Jansch, H.; Zaki, M.; Xu, J. & Jr., J. Y. (1991), 'Ultraviolet photodesorption of CO from NiO as measured by infrared spectroscopy', *Surface Science* **255**(3), 295 - 302.

Zhou, J.; Lu, H.; Gustafsson, T. & Garfunkel, E. (1993), 'Anomalously weak adsorption of Cu on SiO<sub>2</sub> and MgO surfaces', *Surface Science* **293**(3), L887-L892.

Zhou, X. L.; Zhu, X. Y. & White, J. M. (1991), 'Photochemistry at adsorbate/metal interfaces', *Surface Science Reports* **13**(3-6), 73 - 220.

Zimmermann, F. M. & Ho, W. (1995), 'State resolved studies of photochemical dynamics at surfaces', *Surface Science Reports* **22**(4-6), 127 - 247.

Zinke-Allmang, M.; Feldman, L. C. & Grabow, M. H. (1992), 'Clustering on surfaces', *Surface Science Reports* **16**(8), 377-463.

Dai, H.-L., H. W., ed. (1995), *Laser Spectroscopy and Photochemistry on Metal Surfaces*, World Scientific Publishing Co. Pte. Ltd.

## List of figures

Figure 2.1	Schematic drawing of the MGR model.....	6
Figure 2.2	Schematic drawing of the Antoniewicz model.....	7
Figure 2.3	Schematic drawing for TPD experimental setup.....	8
Figure 2.4	Diffraction from a one-dimensional lattice.....	11
Figure 2.5	Schematic drawing of the LEED.....	13
Figure 2.6	Schematic diagram of fourier transform spectrometer.....	17
Figure 2.7	Spectra (on the left) with corresponding double-sided interferograms.....	18
Figure 3.1	The UHV chamber.....	21
Figure 3.2	Schematic diagram of the sample holder.....	23
Figure 3.3	FTIR spectrometer under the chamber.....	25
Figure 4.1:	LEED pattern of Al <sub>2</sub> O <sub>3</sub> /NiAl(110).....	31
Figure 4.2:	Dimension of the Al <sub>2</sub> O <sub>3</sub> /NiAl(110) unit mesh.....	31
Figure 4.3:	He <sup>+</sup> ion scattering spectra of the clean and oxidised NiAl(110) surface.....	32
Figure 4.4:	Thermal desorption spectra of the system CO/Al <sub>2</sub> O <sub>3</sub> /NiAl(110).....	33
Figure 4.5:	Schematic representation of the Wulff-Kaichew construction.....	36
Figure 4.6:	Surface potential experienced by a diffusing adatom.....	36
Figure 4.7:	Comparison of (00) spot profiles after deposition of various amounts of Pt.....	37
Figure 4.8:	STM image of the alumina film covered with 0.25Å Pt.....	38
Figure 4.9:	Size distributions of Pt particles for effective platinum coverages.....	39
Figure 4.10:	Clusters density & mean cluster size as a function of platinum coverage. ....	40
Figure 4.11:	Mean cluster height as a function of the mean cluster size.....	41
Figure 4.12:	Top view of 2ÅPt deposited at 300K/Al <sub>2</sub> O <sub>3</sub> /NiAl(110) AFM image.....	42
Figure 4.13:	3 dimensional view of 2ÅPt deposited at 300K/Al <sub>2</sub> O <sub>3</sub> /NiAl(110) AFM image.....	43
Figure 4.14:	Top view of 1ÅPt deposited at 300K/Al <sub>2</sub> O <sub>3</sub> /NiAl(110) AFM image.....	43
Figure 4.15:	3 dimensional view of 1ÅPt deposited at 300K/Al <sub>2</sub> O <sub>3</sub> /NiAl(110) AFM image.....	44
Figure 4.16:	Top view of 2ÅPt deposited at 100K/Al <sub>2</sub> O <sub>3</sub> /NiAl(110) AFM image.....	45
Figure 4.17:	3 dimensional view 2ÅPt deposited at 100K/Al <sub>2</sub> O <sub>3</sub> /NiAl(110) AFM image.....	45
Figure 4.18:	Top view of 1ÅPt deposited at 100K/Al <sub>2</sub> O <sub>3</sub> /NiAl(110) AFM image.....	46
Figure 4.19:	3 dimensional view of 1ÅPt deposited at 100K/Al <sub>2</sub> O <sub>3</sub> /NiAl(110) AFM image.....	47
Figure 4.20:	Top view of STM scan of 1ÅPt deposited at 300K/Al <sub>2</sub> O <sub>3</sub> /NiAl(110).....	48

Figure 4.21: Three dimensional view of STM scan of 1ÅPt deposited at 300K/Al <sub>2</sub> O <sub>3</sub> /NiAl(110)...	49
Figure 5.1: LEED pattern of Al <sub>2</sub> O <sub>3</sub> /NiAl(110).....	52
Figure 5.2: Dimension of the Al <sub>2</sub> O <sub>3</sub> /NiAl(110) unit mesh .....	53
Figure 5.3: He <sup>+</sup> ion scattering spectra of the clean and oxidised NiAl(110) surface.(Jacobs 1994).	54
Figure 5.4: Thermal desorption spectra of the system CO/Al <sub>2</sub> O <sub>3</sub> /NiAl(110) .....	55
Figure 5.5: Schematic representation of the Wulff-Kaichew construction.....	55
Figure 5.6: Surface potential experienced by a diffusing adatom. ....	56
Figure 5.7: Pt/Al <sub>2</sub> O <sub>3</sub> /NiAl(110) comparison of spot profiles of various amounts of Pt.....	57
Figure 5.8: STM image of the alumina film covered with 0.25Å Pt .....	58
Figure 5.9: Size distributions of Pt particles for different Pt coverages.....	59
Figure 5.10: Clusters density and mean cluster size as a function of Pt coverage.....	60
Figure 5.11: Mean cluster height as a function of the mean cluster size.....	61
Figure 5.12: Top view of 2ÅPt deposited at 300K/Al <sub>2</sub> O <sub>3</sub> /NiAl(110), .....	62
Figure 5.13: 3 dimensional view of 2ÅPt deposited at 300K/Al <sub>2</sub> O <sub>3</sub> /NiAl(110).....	63
Figure 5.14: Top view of 1ÅPt deposited at 300K/Al <sub>2</sub> O <sub>3</sub> /NiAl(110).....	64
Figure 5.15: 3 dimensional view of 1ÅPt deposited at 300K/Al <sub>2</sub> O <sub>3</sub> /NiAl(110),.....	65
Figure 5.16: Top view of 2ÅPt deposited at 100K/Al <sub>2</sub> O <sub>3</sub> /NiAl(110).....	66
Figure 5.17: 3 dimensional view 2ÅPt deposited at 100K/Al <sub>2</sub> O <sub>3</sub> /NiAl(110),.....	67
Figure 5.18: Top view of 1ÅPt deposited at 100K/Al <sub>2</sub> O <sub>3</sub> /NiAl(110).....	69
Figure 5.19: 3 dimensional view of 1ÅPt deposited at 100K/Al <sub>2</sub> O <sub>3</sub> /NiAl(110),.....	70
Figure 5.20: Top view of STM scan of 1ÅPt deposited at 300K/Al <sub>2</sub> O <sub>3</sub> /NiAl(110).....	71
Figure 5.21: Three dimensional view of STM scan of 1ÅPt deposited at 300K/Al <sub>2</sub> O <sub>3</sub> /NiAl(110)....	72
Figure 5.22 The frequency of CO vibrational coverage as a function of Pt thickness.....	73
Figure 5.23 FT-IRRAS spectra of CO adsorption coverage on 1ÅPt/Al <sub>2</sub> O <sub>3</sub> /NiAl(110).....	74
Figure 5.24 FT-IRRAS spectra of CO adsorption coverage on 0.5 ÅPt/Al <sub>2</sub> O <sub>3</sub> /NiAl(110).....	75
Figure 5.25 FT-IRRAS spectra of CO adsorption coverage on 2 ÅPt/Al <sub>2</sub> O <sub>3</sub> /NiAl(110).....	76
Figure 5.26 FT-IRRAS spectra of CO adsorption coverage on 3 ÅPt/Al <sub>2</sub> O <sub>3</sub> /NiAl(110).....	77
Figure 5.27 Diagram of the IR intensity peaks of the CO adsorbed on different Pt nanoparticles. .	78
Figure 5.28 Frequency shifts for different Pt thickness as a function of CO adsorption coverage. .	79
Figure 5.29 TPD experiments of CO saturation coverage adsorbed on Pt nanoparticles.....	81
Figure 5.30 TPD of CO from Pt/Al <sub>2</sub> O <sub>3</sub> /NiAl(110) Winkelmann <i>et al.</i> (1994).....	82
Figure 5.31 TPD spectra of CO adsorbed on 2Å Pt/Al <sub>2</sub> O <sub>3</sub> /NiAl(110).....	83
Figure 5.32 TPD spectra of CO adsorbed on 2Å Pt/Al <sub>2</sub> O <sub>3</sub> /NiAl(110) as function of CO coverage	84

Figure 5.33 FT-IRRA spectra of CO adsorbed on 2Å Pt/Al <sub>2</sub> O <sub>3</sub> /NiAl(110) with tempering.....	85
Figure 5.34 TPD of CO adsorbed on 2Å Pt deposited at different temperatures on Al <sub>2</sub> O <sub>3</sub> /NiAl(110) .....	86
Figure 6.1 FT-IR spectra of CO adsorbed on Pt(111) crystal before and after Laser irradiation....	89
Figure 6.2 FTIR spectra for <sup>13</sup> CO on Pt(111).....	91
Figure 6.3 FTIR spectra for CO on Pt(111) irradiated by 193 nm laser.....	92
Figure 6.4 FTIR spectra of CO adsorbed 1Å Pt/Al <sub>2</sub> O <sub>3</sub> /NiAl(110) irradiated by different laser fluences.....	93
Figure 6.5 Frequency shift of CO after Laser irradiation as a function of laser fluence.....	94
Figure 6.6 FTIR spectra of CO adsorption coverage on 1Å Pt and after laser irradiation.....	96
Figure 6.7 Relative change of FT-IR intensity of CO as a function of laser fluence.....	98
Figure 6.8 Plot of the coverage of CO as a function of photons impinged onto the surface.....	99
Figure 6.9 Desorption cross sections for CO as a function of laser fluence.....	100
Figure 6.10 Adsorbate induced roughening.....	101
Figure 6.11 FTIR spectra of CO adsorbed on 0.5Å Pt/Al <sub>2</sub> O <sub>3</sub> /NiAl(110) after laser irradiation with 6.4 mJ/cm <sup>2</sup> .....	103
Figure 6.12 FTIR spectra of CO adsorbed at T=90K on 1Å Pt/Al <sub>2</sub> O <sub>3</sub> /NiAl(110) after laser irradiation with 6.4 mJ/cm <sup>2</sup> .....	104
Figure 6.13 FTIR spectra of CO adsorbed at T=90K on 2Å Pt/Al <sub>2</sub> O <sub>3</sub> /NiAl(110) after laser irradiation with 6.4 mJ/cm <sup>2</sup> .....	105
Figure 6.14 FTIR spectra of CO adsorbed at T=90K on 3Å Pt/Al <sub>2</sub> O <sub>3</sub> /NiAl(110) after laser irradiation with 6.4 mJ/cm <sup>2</sup> .....	106
Figure 6.15 Frequency shift of the CO stretching vibration as a function of number of photos impinged with different Pt thicknesses.....	107
Figure 6.16 Desorption cross sections for CO as a function of Pt coverage for a laser fluence of 6.4 mJ/cm <sup>2</sup> .....	108
Figure 6.17 CO adsorption coverage on 1Å Pt for different preparations.....	110

## **Curriculum Vitae**

Name	Alaa Al-Shemmary
Date of Birth	31.10.1980
Place of Birth	Najaf- Iraq

### **Educational Background**

Since 10/2009	Research fellow in Deutsches Elektronen-Synchrotron DESY
Since 10/2005	Ph.D Student in Physical Chemistry, Oldenburg University, Ph.D work on "Real Time Control of Photochemical Surface Reactions"
09/2001 – 09/2004	M.Sc. Laser Engineering, College of Engineering, Al-Nahrain University "Design and Analysis of Laser Guidance System using Detector Array" Baghdad-Iraq
09/1998 –09/2001	B.Sc. Laser Engineering, College of Engineering, Al-Nahrain University "Design and Implementation of Nd:YAG Flashlamp Power Supply", Baghdad-Iraq
09/1995-09/1998	Secondary School Baccalaureate, Najaf-Iraq
09/1992-09/1995	Intermediate School, Najaf-Iraq
09/1986-09/1992	Primary School, Bucharest-Romania

### **Scientific publications and posters**

Al-Shemmary, A.; Buchwald,R. and Al-Shamery, K. (2010), 'Surface photochemistry of CO adsorbed at alumina supported nanoparticulate platinum', J. Phys.: Condens. Matter **22**, 084011

Al-Shamery, K.; Al-Shemmary, A.; Buchwald,R.; Hoogestraat, D.; Kampling, M.; Nickut, P. and Wille, A. (2010), 'Elementary processes at nanoparticulate photocatalysts', Eur. Phys. J. B **75**, 107–114.

Redlin, H.; Al-Shemmary, A.; Azima, A., Stojanovic, N.; Tavella, F.; Willd,I. and Düsterer, S. (accepted), 'The FLASH pump-probe laser system: setup, characterization and optical beamlines', Nuclear Instruments and Methods in Physics Research Section A.

Al-Shemmary, A.; Buchwald, R.; Hoogestraat, D. and Al-Shamery, K. 'Photochemistry of adsorbates at nanoparticulate systems' Bunsentagung 2008, Saarbrücken 1-3 May

Buchwald, R.; Wille, A.,; Al-Shemmary, A.; Hoogestraat, D. and Al-Shamery, K. ' Photochemistry of adsorbates at nanoparticulate systems' DIET XI-International Workshop 2007, Berlin 11-15 March.

## **Declaration**

Hereby I declare that I wrote the thesis by myself and listed all used sources. I agree with making the thesis publicly available.

Alaa Al-Shemmary

Hamburg 29.9.2010